UNIVERSITY OF CALIFORNIA
RIVERSIDE

Computational Studies of Structure-Property Relations in Wide Bandgap Semiconductors

A Dissertation submitted in partial satisfaction
of the requirements for the degree of

Doctor of Philosophy

in

Materials Science and Engineering

by

Pegah S. Mirabedini

December 2021

Dissertation Committee:
Dr. P. Alex Greaney, Chairperson
Dr. Masaru Rao
Dr. Mahesh Neupane

The Dissertation of Pegah S. Mirabedini is approved:

_____

_____

_____

Committee Chairperson

University of California, Riverside

Acknowledgements

First and foremost, I would like to express my heartfelt gratitude to my wonderful advisor, Dr. Alex Greaney, for his training, support, and inspiring me to grow as a scientist and person.

In accomplishing this thesis, I also had great pleasure of working with researchers, Dr. Structural and electronic properties of 2DMahesh Neupane, Dr. Masaru Rao, Dr. Alfredo Martinez-Morales, Dr. Duncan Ashby, Dr. Taehoon Lim, Harsha Antony, and Agnieszka Truszkowska.

I would like to acknowledge previously published data: Chapter 3 has been partially reproduced from our previous paper published at the *Applied Surface Science Journal* [1]. Part of chapter 4 has been Reproduced from Ref. [2], with the permission of *AIP Publishing*. Chapter 7 has been reproduced from our previous paper [3] with permission from the *Journal of MRS Advances*.

I am deeply grateful to my parents for their unconditional love and support, and for giving me the opportunities and experiences that have made me who I am.

To my Parents.

ABSTRACT OF THE DISSERTATION

Computational Studies of Structure-Property Relations in Semiconductors

by

Pegah S. Mirabedini

Doctor of Philosophy, Graduate Program in Materials Science and Engineering
University of California, Riverside, December 2021
Dr. P. Alex Greaney, Chairperson

This thesis reports on incorporating various computational methods and tools, including first-principles calculations, mesoscale modeling, stochastic modeling, and Artificial intelligence to study structure-property relations in wide bandgap semiconductors.

In the first project, we present first-principles calculations that elucidate the growth mechanism of ZnO photocatalytic materials for water-splitting applications used in sustainable energy storage. Polar surfaces of ZnO are known to have higher photoelectrochemical activity increasing water splitting efficiency. However, they are known to be unstable and less probable to form under normal conditions. In this project, we demonstrate these high-energy surfaces could be stabilized under certain growth conditions. This approach suggests a general solution for controlling the growth morphology, and it can be applied to other compounds to tailor their structure and obtain materials that are not normally stable.

Further, we present a comprehensive study of diamond-based systems for application in high-power and high-frequency electronic devices. This includes two major projects to find solutions for SD of diamond. the first project studies the possibility of using hexagonal

Boron Nitride (hBN) and graphene 2D materials as acceptor or interface layer in diamond-based heterostructures. The second project reports modeling and analysis of amorphous vanadium pentoxide slabs as candidates for SD of diamond.

Chapter six of this thesis introduces a novel AI-based approach to accelerate computational studies of molecule-surface (and molecule-molecule) interactions. To this end, we present an interactive method that couples Gaussian Processes, Bayesian Inference, and molecular dynamics simulations to accelerate the search for the minimum energy structure in molecule-surface interactions. This method addresses the problem of dealing with multiple configurations with similar energies. It enables making accurate predictions from relatively small datasets and quantifying the uncertainty associated with each prediction.

The last chapter of this thesis introduces a Monte Carlo-based raytracing model, named LightCapture, that simulates light absorption in a microfluidic water-treatment reactor. The LightCapture model was developed to predict geometry - light interaction correlations in reactors consisting of micropillars. This is a critical step in determining the reactor's overall photocatalytic efficiency. To evaluate the performance, the model was applied to determine light capture efficiency in microreactors that use an array of TiO_2 photocatalytic micropillars, which are being developed for treating recycled water on spacecraft during deep space missions, and the results were in great agreement with experimental tests.

This thesis provides guiding principles for accelerated discovery of wide bandgap semiconductors. Many of the presented methods and tools have been successfully utilized to provide guiding principles for experimental fabrication.

Table of Contents

List of Figures

List of Tables

1. Introduction and overview

As the name suggests, wide bandgap semiconductors (WBGs) are materials with a larger bandgap, typically above 2 eV, compared to conventional semiconductors. Examples of WBG semiconductors include silicon carbide (SiC), titanium dioxide (TiO_2), zinc oxide (ZnO), and diamond (also known as ultra WBG). The large bandgap of WBGs unlocks many interesting properties in these semiconductors, which makes them attractive for a variety of technological applications. For instance, WBG based devices can work at much higher temperature, voltage, and frequencies compared to other semiconducting systems such as silicon (Si) and gallium arsenide (GaAs). This has brought scientists' attention to design new WBGs to advance electronics technology.

In this thesis, we present a set of methods and tools developed and/or implemented to accelerate the discovery of wide bandgap semiconductors. In the first three projects, we present computational modeling and analysis of various systems including surfaces and interfaces, crystalline and amorphous oxides, and complex heterostructures. In the second two projects, we report development of an artificial intelligence-based method and a stochastic model to accelerate structure optimization at atomic to microscale levels. The presented studies and approaches in this thesis will provide new paths for design of functional semiconductors that find many applications, including sustainable energy, high-power electronics, and water recycling. Furthermore, the presented methods and techniques can be generalized to study other materials systems beyond wide bandgap semiconductors.

Engineering new nanostructures can lead to discovery of materials with superior functionality. Designing tailored structures requires deep understanding of the growth mechanism

and its correlation with the final morphology. A challenge in structure design is that often the desired structure is away-from-equilibrium. Therefore, the first project on this thesis reports on elucidating the growth mechanism of nanopyramidal zinc oxide (ZnO) structures as promising photocatalysts for water-splitting to generate hydrogen.

Recent reports by the U.S. environmental protection agency (EPA) show that Burning of fossil fuels – the major energy source in current transportation systems – is the principal cause of nitrogen oxide (NO_2) and carbon dioxide (CO_2) emission, which leads to the earth's overheating and formation of acidic rains[4]. These problems have drawn scientists' attention to substituting clean energy resources for carbon compounds. Over the past few decades, companies have attempted to generate electric and hydrogen powered vehicles as more planet-friendly means of travelling. The process of generating and burning hydrogen can be both done without forming CO_2 byproducts. Recent advancements report generation of hydrogen using off-peak power generated by wind turbines as a CO_2 free method to produce hydrogens [5]. Therefore, hydrogen-powered transportation removes the generation of particulate pollution from urban settings (i.e., vehicle exhaust). A cost-efficient method to generate hydrogen is through water splitting — that is, breaking water into its components to generate H2 and O2 through hydrogen and oxygen evolution reactions (HER) and (OER), respectively. A photocatalyst can utilize light to accelerate HER through water splitting. Figure 1.1 depicts a schematic of the water splitting reactions at the surface of photocatalysts followed by using the generated H2 in zero-emission transportation such as OCTA.

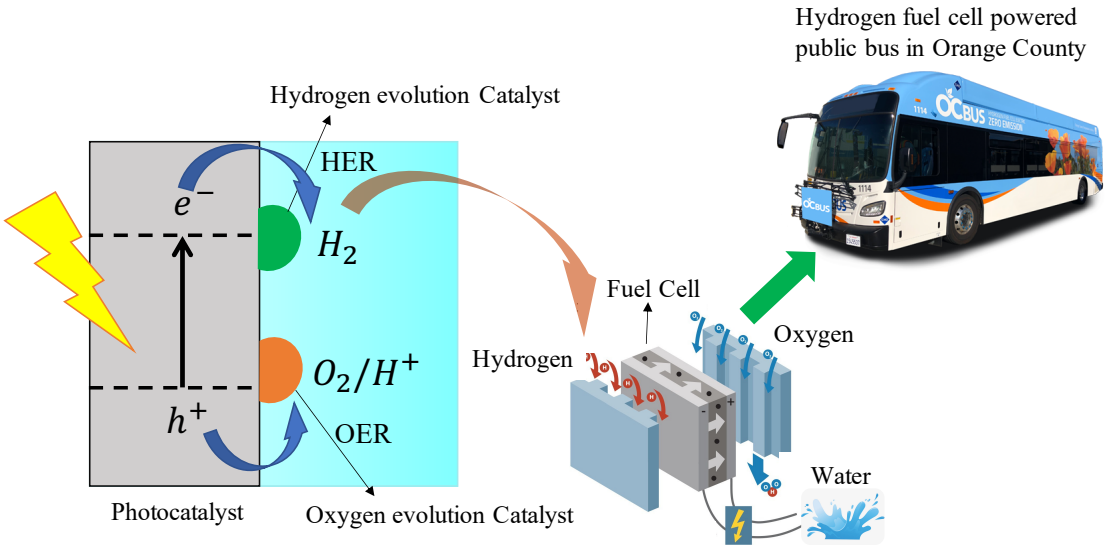

Figure 1.1, Schematic illustration of the water splitting process and the resulting hydrogen evolution reaction (HER) and oxygen evolution reaction (OER).

The ZnO nanopyramidal structures – consisting of semi-polar facets – are generally known to have higher photocatalytic activity, potentially enhancing water splitting performance. However, these morphologies are usually associated with higher energy and hence are less probable to form under normal conditions. The challenge, therefore, lies in stabilizing - lowering the energy of - higher energy shapes to enhance the efficiency of these nano-materials. In this work, we perform a comprehensive set of density functional theory calculations to elucidate the growth mechanism of ZnO nanostructures at different stages of growth in a chemical vapor deposition (CVD) chamber. Our results show a clear correlation between the growth condition and morphology. The predictions show that by controlling the growth condition, we can stabilize high-energy structures of ZnO (and by extension other material systems) to engineer new systems with tailored properties and superior performance.

Diamond is an ultra-wide bandgap (UWBG) semiconductor with the highest breakdown field and carrier mobility, making it an attractive material of choice for next-generation high-speed and high-power electronic and RF device applications [6], [7]. However, unlike other WBGs, diamond cannot be doped with shallow dopants because of the high dopant activation energies [7], [8]. An advanced doping technique that has been developed to mitigate this limitation is Surface Doping (SD) [9], [10]. In this technique, a thin film of acceptor layer with a high electron affinity (EA) is interfaced with a hydrogenated diamond (H-diamond) surface where the C-H dipoles induce a negative electron affinity (NEA). The latter leads to an upward band bending that creates a hole accumulation region at the diamond surface [11]. This accumulated charge forms a high-mobility two-dimensional hole gas (2DHG) channel resulting in *p*-type doping of the diamond surface [12], [13]. The performance of SD-based devices is based on the 2DHG channel and relies on the hydrogen and acceptor layer quality [13]. Initial SD-based diamond devices used atmospheric adsorbates as acceptor layers [9], [14]. However, recent studies have demonstrated improved device performance utilizing relatively controllable amorphous oxide-based acceptor layers, such as Al_2O_3 [15], MoO_3 [16], and V_2O_5 [17], [18]. Although amorphous oxide layers provide favorable band alignment for charge transfer, they suffer from low 2DHG carrier mobilities in diamond due to interface and Coulomb scattering originated from the fixed and trapped charges at the oxide/H-diamond interface [19], [20]. Furthermore, high gate leakage current caused by trap-assisted tunneling [21], [22]. limits H-diamond devices' applicability in high-field, high-power operations.

To facilitate SD in diamond, here we present two major projects: In the first project, we demonstrate that a sheet of hBN or graphene interfaced with the H-diamond (100) surface—the technologically relevant surface for diamond-based electronic devices—could act as a protective layer that preserves the p-type bulk-like conductivity in the H-diamond (100) surface. In the second project, we model and analyze state-of-art amorphous vanadium pentoxide (V_2O_5) slabs as acceptor for SD of diamond. Recent reports show improvements in SD of H-diamond when using high-work function Oxides, such as V_2O_5. In addition, amorphous V_2O_5 contains defects which can provide electron traps for doping diamond. Despite all desirable properties of amorphous V_2O_5 slabs, a thorough computational analysis that elucidates the structural and electronic properties of this system is still lacking. Lack of long-range order in amorphous materials and restricted geometry of make modeling amorphous slabs a hard problem. To address this problem, we propose and deploy a novel melt-quench molecular dynamics simulation approach to generate a wide array of possible amorphous structures. Further, to evaluate the performance of the simulated slabs for surface doping of diamond, we present our density functional theory studies of amorphous V_2O_5/H-diamond (100) vdW and V_2O_5/hBN/H-diamond (100) heterostructures. The presented methods and models in these two chapters will provide guidance for the fabrication of novel high-frequency and high-power electronic devices.

A perennial challenge in computational chemistry is the process of finding the minimum energy configuration of weakly interacting molecules, or molecules interacting with a surface. Predicting the minimum energy structure is vital for modeling a number of chemical applications, including catalysis, design of targeted dugs, and self-assembling surface

coatings. In these problems, we often deal with numerous choices for selecting the initial molecule configuration, and this is particularly challenging if the molecule is flexible. The traditional method of finding the lowest energy structure is to perform calculations starting from many different initial configurations. To be sure of finding the global minimum, a very large number of calculations can be needed, but many of these converge at the same result, which is a waste of computational effort. Here, we present a novel AI-based approach to accelerate computational studies of molecule-surface interactions. Our method is based on an active-learning framework that interactively couples Gaussian Process (GPs) regression, Bayesian inference, and molecular dynamics simulations to accelerate the search for the minimum energy structure. Through utilizing the forces dataset – generated at no additional cost during simulation – we were able to improve the robustness and accuracy of the predictions. To demonstrate application of the proposed method and verify its' accuracy, we used the approach to study water molecules on the zinc oxide semi-polar surface. The presented approach offers a general solution to study molecule surface interactions in other material systems. Therefore, it addresses a long-standing challenge in computational chemistry and any other problem in which we deal with a large dataset and overlap of the targets.

Despite all the advances in technology, still many people do not have access to clean water around the World. TiO2 is a wide-bandgap semiconductor vastly used as a photocatalyst to remove contaminants from water under illumination. Microfluidic reactors that use arrays of TiO2 micropillars offer many advantages such as short diffusion length thanks to their high surface-to-volume ratio [23]. However, scaling down the reactor size comes with

problems such as reducing the free space for light travel and water flow. Optimizing reactor's design is important as it results in reducing the amount of material needed to optimize water treatment reactions, resulting in lower environmental burden and higher inherent safety [23]. Moreover, in many applications, such as long-duration space missions, we face additional design limitations (e.g., low-power, lightweight, and low-volume power matrix). In these cases, it is imperative to achieve high efficiency without a need to scale up the reactor. In the last chapter of this thesis, we present a Monte Carlo based ray tracing model (written in Python) that simulates light absorption in wastewater recycling reactors composing an array of TiO_2 micropillars. The model is further couples with a with a Lattice Boltzmann model [24] to simulate water flow around the pillars. Finally, the finite element method was used to model waste mass transfer as a way to evaluate the overall efficiency of the reactors. This study provides guiding principles for optimizing reactor design to enhance performance. The presented tool was applied to provide insights for the design of microfluidic reactors being developed by our experimental collaborators, Dr. Rao and his team at the Biomedical Microdevices Laboratory at UC Riverside. The theoretical predictions were found to be in great agreement with the experimental test results for the reactor. This thesis provides efficient computational methods, tools, and insights for designing novel wide bandgap semiconductors which will benefit many technological applications including sustainable energy, next-generation electronics, wastewater recycling, etc. Even more importantly, the presented methods and tools can be readily generalized to design other materials systems.

2. Methods

Discovering novel materials with tailored properties is an exciting yet challenging process. Experimental trials and tests can be used to design and analyze new materials, but they are costly and time consuming, especially when dealing with a large search space. Over the past few decades, computational modeling and simulations have been utilized to accelerate materials discovery [25]. Computational analysis can provide extremely helpful tools for experimentalists through predicting new materials systems or by elucidating previous experimental designs and mechanisms, enabling design of new materials by more than ten times faster compared with experimental trials and tests.

In this chapter, we provide an overview of the computational methods used in this thesis. In the first three projects – presented in chapters 3 to 5 – we report on quantum and classical simulations of wide bandgap semiconductors using density functional theory calculations and molecular dynamics simulations, two common methods used to design and study materials computationally. In the last two chapters, we present novel methods and models based on Gaussian Processes, Bayesian inference, Monte Carlo simulations, and ray tracing.

2.1 Density Functional Theory

Density functional theory (DFT) is a method to study the ground-state energy and electronic structure of many-body electrons systems through solving as a set of n one-electron Schrödinger-like equations, also known as the Kohn-Shan equations [26], [27].

$$\left[-\frac{1}{2}\Delta^2 + V_n(r) + V_H(r) + V_{xc}(r)\right]\phi_i(r) = \epsilon_i\phi_i(r) \quad (2.1)$$

The terms on left hand side of this equation are kinetic energy, external potential, Hartree potential, and exchange correlation potentials, respectively. The exact functionals for exchange-correlation potentials (which include many particle interactions) are usually unknown, and therefore, various approximations are used to describe them. The Jacob's ladder, illustrated in Figure 2.1, provides a helpful tool for describing the accuracy and simplicity of various density functional approximations for the exchange-correlation energy [28]. DFT is one of the widely known methods in computational chemistry and solid-state physics. DFT can provide an accurate estimation of materials properties when their atomic or molecular structure is known [27]. However, its time complexity is $O(N^{3-4})$, where N is the density of electrons. This makes DFT very slow and computationally impractical for studying large unit cells.

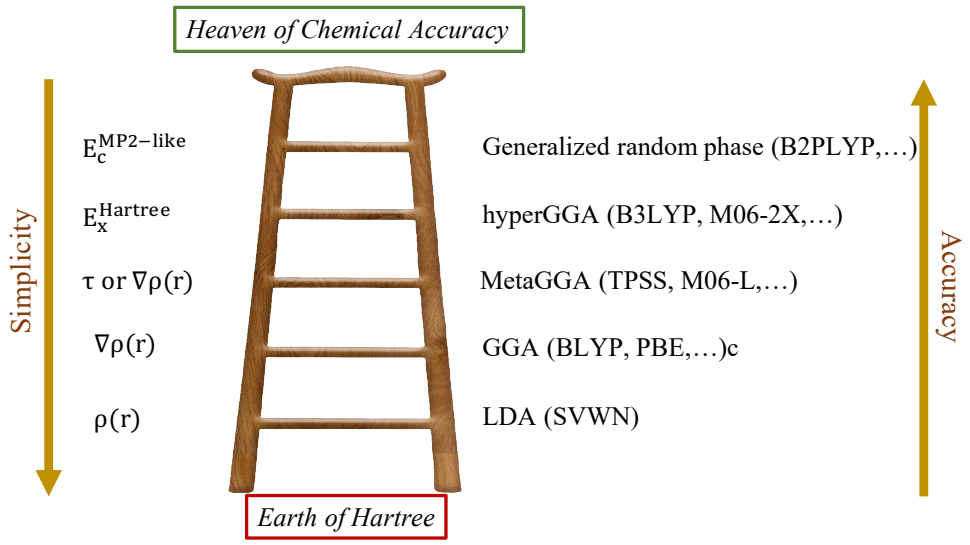

Figure 2.1, Jacob's ladder for exchange-correlation approximations in DFT based on the metaphor of Perdew and Schmidt.[28]

2.2 Molecular Dynamics

Molecular dynamics (MD) simulations study motion and the interactions between atoms and molecules through solving the Newton's equation of motion [29]. Therefore, they are vastly used to study the equilibrium and dynamic properties of relatively larger materials systems and quick optimizations. MD simulations are used in chapters 5 and 6 to model amorphous oxides and generate large structure-energy datasets for AI aided studies of molecule surface interactions.

2.3 Ray Tracing

The concept of Ray Tracing was first introduced by Albrecht Dürer [30]. In computer science and graphics, a ray tracing model is a model that follows the path of light and can ultimately be used to render images with high resolution. In such model, the ray is defined using the origin of ray and the direction it is traveling in. This simplified view, ignores the wave-particle duality of the phonons, yet it is capable of generating high-quality images.

Mathematical relations are then established to find the intersection of the rays with objects having different shapes. This helps us mathematically compute all types of interactions between a ray and a surface. For instance, we can determine whether light is transmitted or reflected back. We can also find the type of reflection, which can be used to determine the color of an object or the ray's next path. After reflection, the light might hit another object on its way. To analyze what happens to light after reflection, we need to consider the trajectory of light as it bounces off in between surfaces [31]. The LightCapture model uses a similar technique to trace phonon paths and find out where the rays hit the pillars.

2.4 Monte Carlo Methods

Monte Carlo (MC) Methods (i.e., Monte Carlo Simulations) (Binder, 1987) are statistical methods that use a set of random samples to approximate the solution of integration and optimization problems [32]. MC methods approximate a function of probability distributions using a set of randomly simulated values [33]. That is, instead of predicting fixed values, MC models generate a set of possible results by means of a probability distribution, such as gaussian distribution. Monte Carlo-based models are widely used in finance, artificial intelligence, and other scientific or non-scientific simulations. The name, Monte Carlo, is originated from a famous casino town, named "Monaco", as like a gambling game like roulette, chance plays an important role in MC simulations [34].

2.5 Gaussian Distribution

The Gaussian (Normal) distribution is widely used in probability theory to represent unbiased uncertainties and residual errors in modeling multiple processes with additive characteristics and symmetric distribution. According to the central limit theorem, the distribution

of the sum of a set of real-valued random variables, which are independently and identically distributed, converges to a normal distribution. The resulting normal distribution forms a so-called "bell curved" shape [35], [36]. Most natural phenomena can be approximated by the normal distribution, and hence, Gaussian distribution is the most popular probability distribution in statistics and machine learning [37].

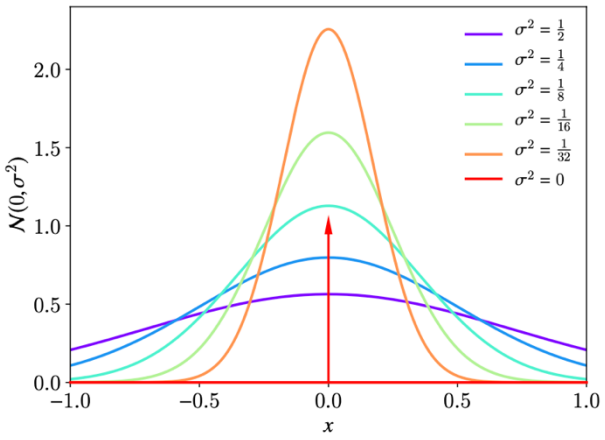

Figure 2.2, Sample plots of gaussian distribution showing the Gaussian bell curve shape with μ=0 and different values of variance [121].

The cumulative distribution function (cdf) of a continuous random variable X is defined as [37],

$$P(x) \triangleq Pr\,(X \leq x) \tag{2.2}$$

Where, capital P letter represents cdf, and Pr is probability. The cdf of the Gaussian is,

$$\Phi(x; \mu, \sigma^2) \triangleq \int_{-\infty}^{y} \mathcal{N}(z|\mu, \sigma^2)dz = \frac{1}{2}[1 + \text{erf}\,(z/\sqrt{2})] \tag{2.3}$$

With $z = (x - \mu)/\sigma$, and $erf(u)$, error function defined as,

$$\text{erf}(u) \triangleq \frac{2}{\sqrt{\pi}} \int_0^u e^{-t^2} dt \tag{2.4}$$

where μ, σ, and σ^2 represent the mean, standard deviation, and the variance of the distribution, respectively.

The probability density function (pdf) of a Normal distribution is found by taking the derivative of cdf [35],

$$\mathcal{N}(x|\mu, \sigma^2) = \frac{1}{\sqrt{2\pi\sigma^2}} e^{-\frac{(x-\mu)^2}{2\sigma^2}} \tag{2.5}$$

A significant property of normal distribution is that it has the maximum entropy among all possible probability distributions over the reals with a mean μ and variance σ^2. The general form of entropy for a continuous random variable (X) with a probability density $f(x)$ is,

$$H(X) = -\int_{-\infty}^{\infty} f(x) log f(x) dx \tag{2.6}$$

Solving this for a normal distribution, yields the entropy function as,

$$H(X) = \frac{1}{2}(1 + \log(2\sigma^2\pi)) \tag{2.7}$$

Gaussian distributions are discussed in more details in chapter 2.

3. Engineering functional morphology in ZnO

3.1 Overview

Zinc oxide (ZnO) is an interesting photocatalyst material for water splitting due to its unique electronic properties, low-cost, high sensitivity to light, and nontoxic nature [38], [39]. A variety of morphologies containing polar and non-polar surfaces can be achieved by controlling the growth condition. Previous studies have reported synthesis of ZnO nanostructures, including nanoparticles [40], nanorods [41], tetrapods [42], [43], and even nanoflowers[44], [45] (Figure 3.1). Stability and efficiency are two important factors in determining the feasibility of a photocatalyst for oxygen evolution reactions in water splitting applications [46]. While many experimental and theoretical works have studied the nanorod geometries of ZnO formed by $\{10\bar{1}0\}$ and $\{0001\}$ crystal planes [47], little is known about the high-index facets such as $\{11\bar{2}2\}$ which form a nanopyramidal structure. The $\{11\bar{2}2\}$ semi-polar facets of ZnO are known to have high electrochemical activity and better reversibility of the adsorption-desorption process, which can potentially result in superior water splitting performance process [48], [49]. On the other hand, the semi-polar facets are also known to be associated with higher energy, which makes them thermodynamically less stable, and hence, less probable to form under normal growth conditions as compared to the low-index planes of Wurtzite ZnO, such as $\{10\bar{1}0\}$ and $\{0001\}$.

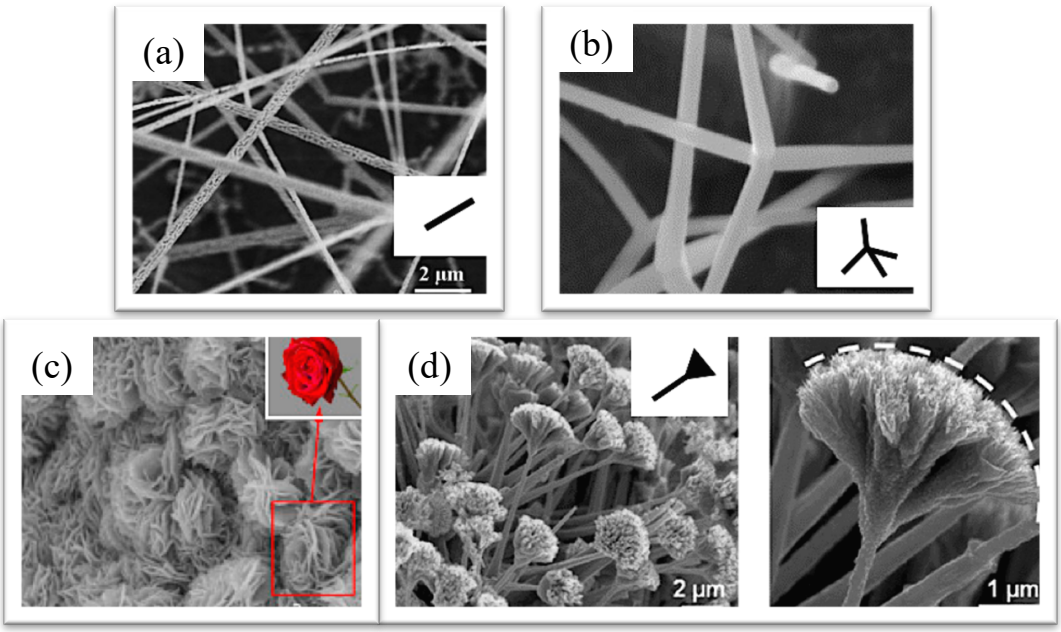

Figure 3.1, Scanning electron microscope (SEM) and transmission electron microscope (TEM) images of example nanostructures and their simplified models: (a) High-porosity ZnO nanowires grown on an Sn-coated Si substrate,[50] (b) FE-SEM images of tetrapod-like ZnO nanorods,[42] (c) ZnO rose-like nanoflowers [27], (d) SEM images of ZnO nanoflowers.[43]

The motivation of this research arises from an interesting observation by our experimental collaborators, Dr. Martinez-Morales and his team at the UC Riverside Center for Environmental Research & Technology (CE-CERT), who observed an unexpected growth of $\{11\bar{2}2\}$ nanopyramidal surfaces during chemical vapor deposition of ZnO (Figure 3.2). Interestingly, the J-V characteristics and electro-chemical impedance spectroscopy (EIS) under illuminated condition results show higher photocatalytic activity for the nanopyramidal structures containing $\{11\bar{2}2\}$ planes compared to the nanorod structures formed by the $\{10\bar{1}0\}$ facets (Figure 3.3). These exciting observations intrigued us to seek the answer to two important questions: I) What condition results in the growth of ZnO nanopyramidal structures? and II) Do the nanopyramidal structures show higher activity?

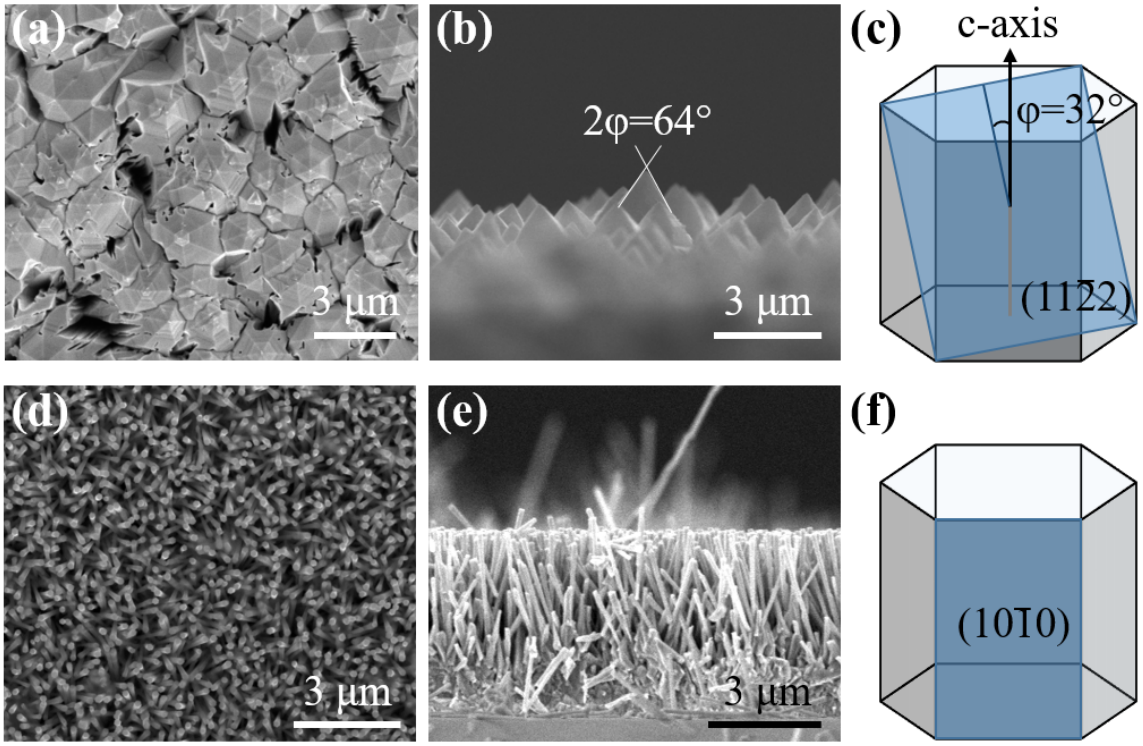

Figure 3.2, (a) Top-view and (b) cross-sectional SEM images of synthesized pyramidal ZnO, (c) schematic drawing of (11$\bar{2}$2) plane for geometric analysis. (d) Top-view and (e) cross-sectional SEM images of synthesized nanorod ZnO, (f) schematic drawing of (10$\bar{1}$0)

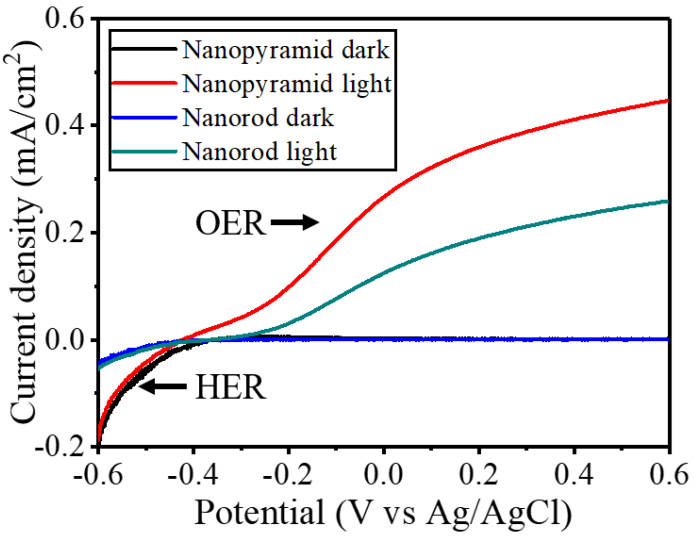

Figure 3.3, J-V characterization under dark and illumination

The equilibrium shape of a material is controlled by the thermodynamic stability of the whole structure and Kinetic of growth; that is the rate at which the crystal facets grow [21 prop]. Understanding which of the above two factors dominates is of great importance in determining the growth mechanism and structure. Here, we were able to elucidate the growth mechanism of ZnO nanostructures through analysis of thermodynamic stability. However, further analysis of growth kinetics is suggested for morphologies which cannot be explained through thermodynamics rules. The Wulff construction is vastly used to determine the equilibrium shape of a crystal structure. The Wulff construction is found through minimizing the surface Gibbs free energy defined as,

$$\Delta G_i = \sum_j \gamma_j O_j \tag{3.1}$$

where γ_j and O_j represent the surface energy and area of a crystal facet. Figure 3.4 illustrates a schematic of Wulff construction. Increasing the ratio of a desired crystal surface

can be achieved through reducing its surface energy or increasing the surface energy of other facets. Therefore, surface energy plays an important role in determining the Wulff construction representing thermodynamic stability and crystal epitaxial growth, and hence is critical to synthesis of novel materials. Since experimental measurements of surface energy is difficult, first-principles methods are used to evaluate this quantity [51]. Herein, we perform a set of Density Functional Theory calculations to study and compare the stability and photocatalytic efficiency of the surfaces formed during different stages of the growth process of ZnO. Our study suggests a general approach for understanding and controlling growth condition to engineer novel nanostructures with desired properties.

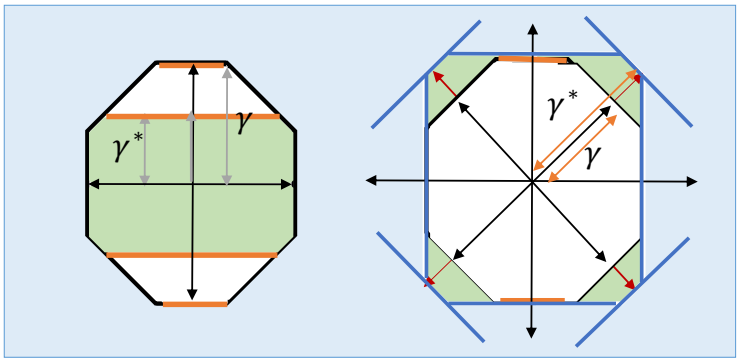

Figure 3.4, Simplified illustration of schematic Wulff construction

3.2 Surface Energy Calculations

Electronic structure calculations were performed to compute the surface energy of the non-polar $(10\bar{1}0)$ and semi-polar $(11\bar{2}2)$ facets of ZnO and to determine how the electronic structure of these surfaces affects the crystal growth process and photocatalytic activity. DFT was used to compute the total energy of infinite slabs of ZnO with exposed parallel $(10\bar{1}0)$ or $(11\bar{2}2)$ facets, as shown in Figure 3.5. The slabs for DFT calculations were cut from bulk ZnO crystal and relaxed. Depending on where the cut-plane intersects the unit

cell, several surface structures are possible, enabling the formation of stoichiometric surfaces and surfaces that are O-rich or Zn-rich. In the $[10\bar{1}0]$ direction, the packing of atomic planes follows an AaBbAa sequence. The $(10\bar{1}0)$ facet can be cut between the narrowly spaced Aa planes or the wider aB planes. The energy of surfaces created as a result of both possible cuts was computed, and the surfaces cut between the wider aB planes were found to be significantly lower in energy as they are more compact. As a result, these lower energy surfaces are the structures that are reported on in this work.

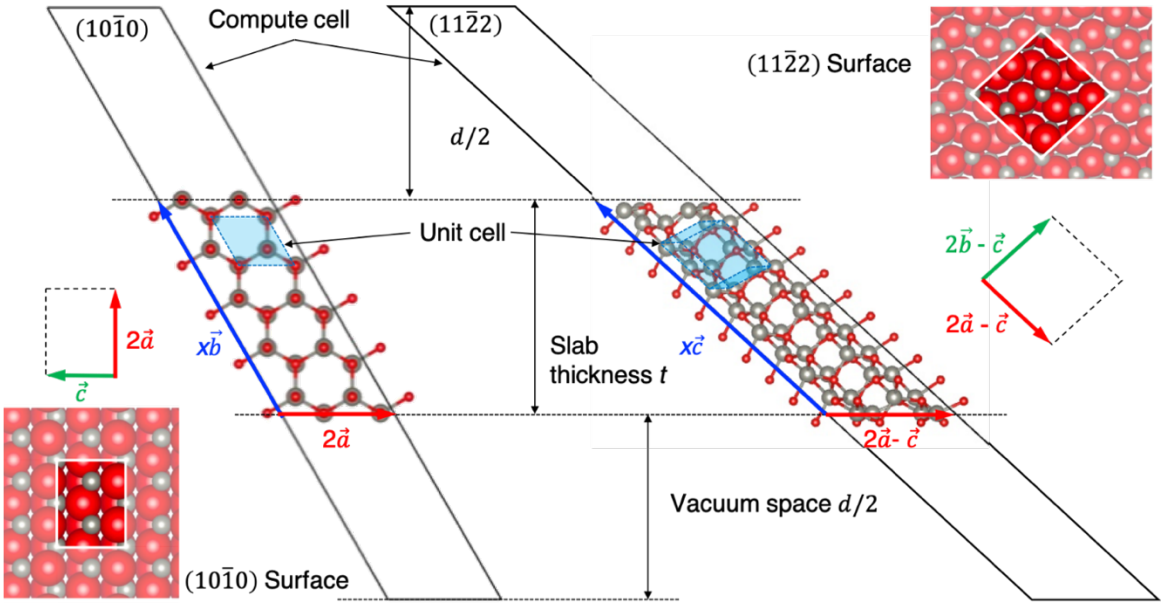

Figure 3.5, Computational cells geometries of the generated $\{10\bar{1}0\}$ and $\{11\bar{2}2\}$ slabs, demonstrating surface areas, slabs thickness (t), vacuum space (d), and the cell vectors in terms of unit cell lattice parameters a, b, and c (where x is an integer number in range 5-11 for the $\{10\bar{1}0\}$ surface and 5-8 for the $\{11\bar{2}2\}$ slabs).

The $\{10\bar{1}0\}$ surfaces lie parallel to the polar c-axis of the crystal. Each layer of atoms in the AaBb packing sequence is stochiometric, making the facets nominally non-polar. However, under relaxation, the stoichiometric $(10\bar{1}0)$ surface undergoes a small buckling distortion, generating a small polarization perpendicular to the surface. Non-stochiometric

$\{10\bar{1}0\}$ surfaces that are deficient in either Zn or O can also be generated by removal of the Zn or O atoms from the surface layer. The $(10\bar{1}0)$ facet, therefore, has three distinct surface energies, $\gamma_{(10\bar{1}0)-S}$, $\gamma_{(10\bar{1}0)-Zn}$, and $\gamma_{(10\bar{1}0)-O}$ for the stoichiometric, Zn-, and O-rich structures, respectively.

The surface energies of stoichiometric surfaces, $\gamma_{(hkwl)-S}$, were calculated by computing the facet energy of relaxed slabs, each containing a single pair of parallel stoichiometric facets, using the following equation [52],

$$\gamma_{(hkwl)-S} = \frac{E_{slab} - N_O E_{bulk}}{2A} \tag{3.2}$$

where E_{slab} is the total energy of the slab, N_O is the number of oxygen atoms in the slab, E_{bulk} is the energy of one formula unit of bulk ZnO, and A is the area of the surface. The factor of 2 in the denominator indicates the presence of a top and bottom surface in the slab model.

The surface energy of the non-stoichiometric facets depends on the chemical potential of the reservoir from which the excess surface species is drawn. The energies of these surfaces were obtained from calculations of slabs with one stoichiometric surface and a non-stoichiometric opposing surface. The surface energy of the non-stoichiometric facet is given by,

$$\gamma_{(hkwl)-X} = \frac{1}{A}\left[E_{slab} - E_{ref}(N_O, N_{Zn}, \Delta\mu_O)\right] - \gamma_{(hkwl)-S}, \tag{3.3}$$

with the reference energy defined as,

$$E_{ref}(N_O, N_{Zn}, \Delta\mu_O) = N_{Zn}\left(E_{bulk} - \Delta\mu_O - E_{O_2}\right) + N_O\left(\Delta\mu_O - E_{O_2}\right) \quad (3.4)$$

where N_O and N_{Zn} are the number of O and Zn atoms in the system, respectively. $E_{O_2}$is the cohesive energy per atom of oxygen in the O_2 dimer. The oxygen chemical potential, $\Delta\mu_O$, is defined as the difference between chemical potential of oxygen in the reactor and half of cohesive energy of a single oxygen dimer in isolation, and it is plotted over the range for which ZnO is stable [53]. This gives the low $\Delta\mu_O$ limit as the chemical potential at which ZnO is reduced to Zn metal and O_2 gas,

$$(E_{bulk} - E_{Zn-HCP} - E_{O_2}) \leq \Delta\mu_O \leq 0 \quad (3.5)$$

where E_{Zn-HCP} is the cohesive energy per atom of HCP Zn metal. The relaxed low energy geometries of the stochiometric, Zn-rich, and O-rich $(10\bar{1}0)$ facets are shown in Fig. 3.6, (a)–(c), respectively.

The geometric permutations of the semi-polar $\{11\bar{2}2\}$ surfaces are more complex with four distinct surface terminations: O- and Zn-terminated stoichiometric surfaces (opposite faces of a stoichiometric slab) and O- and Zn-rich non-stoichiometric surfaces. Although four different permutations of the top and bottom surface structures can be created, from the ZnO crystal structure, it is only possible to determine three independent surface energy metrics. While the distinct surface energies for the $(10\bar{1}0)$ facets can be determined, for the $(11\bar{2}2)$ surface, the energy of the stoichiometric surface, $\gamma_{(11\bar{2}2)-S}$, is taken as half of the cleavage energy, $\gamma_{(11\bar{2}2)-S} = \frac{1}{2}\left(\gamma_{(11\bar{2}2)-S-Zn} + \gamma_{(11\bar{2}2)-S-O}\right)$. This is used as the reference surface in Eq. 2 to define the energies of the Zn- and O-rich surfaces, $(11\bar{2}2)$-Zn

and $(11\bar{2}2)$-O. These relaxed structures of the $(11\bar{2}2)$ facets are shown in Figure 3.6, (d)-(f).

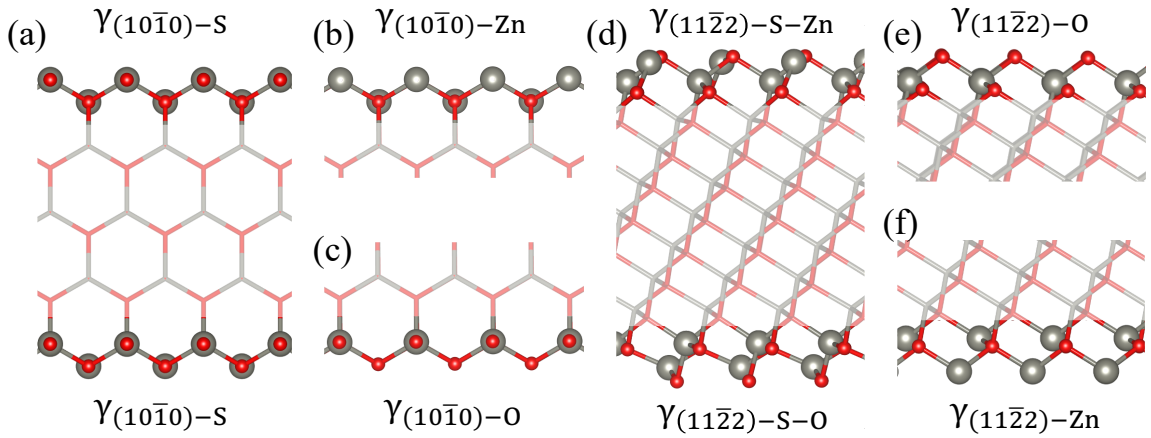

Figure 3.6, Profile view of ZnO surface facets after relaxation. (a-c) Slabs of the $(10\bar{1}0)$ surfaces viewed along the c-axis, and (d-f) slabs of the $(11\bar{2}2)$ surfaces viewed from a direction perpendicular to the c-axis. (a) Shows the low energy stoichiometric surfaces, (b) and (c) show the same surface depleted of O and Zn, to generate the Zn and O rich surfaces, respectively. (d) Shows the Zn and O terminated stoichiometric planes, with (e) showing the O-rich surface, and (f) the Zn-rich surface.

The energy calculations were performed using supercells with (2×1) and (2×2) periodicity in the plane of the slab for $\{10\bar{1}0\}$ and $\{11\bar{2}2\}$ structures to allow the system freedom to undergo surface reconstructions that break the crystal symmetry. To obtain a consistent set of fully converged surface energies, calculations were performed for a series of slabs by systematically varying the slab thickness and vacuum separation. In order to obtain a consistent set of fully converged surface energies, we performed a series of energy calculations for slabs systematically varying the slab thickness and vacuum separation. To converge the surface energy of the $(10\bar{1}0)$ facet with respect to slab thickness, *t*, slabs with 5 to 16 atomic layers — thickness of 14 to 45 Å — were generated and fully relaxed following the computational method discussed earlier in this chapter. For the $(11\bar{2}2)$ surface energy, slabs were generated with 5 to 10 double layers — thickness of 15 to 30 Å. In addition, in

order to find the optimum vacuum distance to avoid interaction between layers, slabs with a vacuum space (d) of 15 to 35 Å were tested. All atoms were allowed to fully relax in the *x*- *y*- and *z*- directions. The surface energy of the $(10\bar{1}0)$ facets was computed to an accuracy of 0.01 J/m^2. Convergence was achieved with slabs having a thickness of 11 or more atomic layers (≥ 31 Å) and a vacuum space of 20 Å. In contrast, the convergence of the semi-polar $(11\bar{2}2)$ surface was harder to achieve due to the existence of an internal field formed in the polar slabs. In this case, surface energies were computed following the convergence method by Meyer *et al.* [53], where the energies of slabs with a series of different thicknesses, *t*, were computed and then the $1/t$ dependence of the slab energy was extrapolated to remove the effect of the internal field. This method resulted in the surface energy of the $(11\bar{2}2)$ facets computed to an accuracy of only 0.1 J/m^2.

All DFT calculations were performed using the Vienna ab-initio Simulation Package (VASP) [54]–[57] within the Perdew-Berke-Ernzerhof (PBE) general gradient approximation (GGA) exchange-correlation functional [58], [59]. The calculations were spin-polarized with a plane wave cutoff energy of 400 eV. Core electrons were modeled implicitly using the projector-augmented wave method (PAW) pseudopotentials [60], [61]. Structures were relaxed using the conjugate gradient algorithm [62] to minimize the forces for ionic relaxation to lower than 1×10^{-3} eV/Å. A great deal of care was taken to obtain a fully converged and relaxed bulk ZnO reference structure, as errors in the energy prediction of this reference state are the largest source of uncertainty in the surface energy predictions. The cohesive energy of the bulk crystal structure was found to be well converged using a 5×5×5 Monkhorst-Pack grid of k-points for the Brillouin zone integration. Using this

approach, the modeled bulk ZnO had equilibrium lattice parameters of a = 3.19 Å and c = 5.30 Å. For the slab calculation, a 5×5×1 Γ-centered k-point mesh was used for Brillouin zone sampling with one k-point along the nonperiodic direction perpendicular to the slab.

The surface energies computed using the described procedure above were used in the Wulff construction to predict the equilibrium morphology of ZnO crystallite growing on a substrate with its *c*-axis perpendicular to the substrate. The energy of the ZnO/substrate interface is assumed to be zero. The equilibrium morphologies were used for the theoretical predictions of the height to width ratio and the $\{11\bar{2}2\}$ to $\{10\bar{1}0\}$ surface area ratio of ZnO pyramidal nanocrystals grown under different oxygen chemical potential conditions. For growth on most substrates, it is likely that the effective surface energy of the ZnO/substrate is negative due to the reduction in energy from covering the exposed substrate and ZnO-(0001) surfaces by bringing ZnO into contact with the substrate. If the effective ZnO-(0001)/substrate interface energy is negative, then the width-to-height ratio and $\{11\bar{2}2\}$ to $\{10\bar{1}0\}$ surface area ratio of ZnO pyramidal nanocrystals will be underestimated.

3.3 Prediction of Crystal Growth Morphology

A growing crystal arrives at its final morphology either as the result of anisotropic attachment kinetics producing a shape that becomes kinetically frozen in place, or as a result of the growing crystal relaxing towards its thermodynamically preferred shape. The latter is the shape that minimizes the total surface energy structure and is described by the Wulff construction. Here we consider only the thermodynamically preferred shape and further restrict consideration to the Wulff construction of the crystal containing only $\{10\bar{1}0\}$ and

$\{11\bar{2}2\}$ facets to identify conditions under which pyramidal crystals will be thermodynamically preferred over nanorods.

The energy of the different variants of the $\{10\bar{1}0\}$ and $\{11\bar{2}2\}$ facets are plotted as a function of oxygen chemical potential in Fig. 3.7. For the stoichiometric surfaces, the $(10\bar{1}0)$ facet is more compact and has a lower surface energy of 0.9 J/m^2, while the surface energy of stoichiometric $(11\bar{2}2)$ is 1.8 J/m^2. However, for the non-stoichiometric surfaces, both the O-rich and Zn-rich $(11\bar{2}2)$ facets have lower surface energy than their corresponding $(10\bar{1}0)$ facet. The surface energy versus the chemical potential of oxygen plot in the system (Fig. 3.7 (a)) shows that there is a small range of O-starved growth conditions under which the Zn-rich $\{11\bar{2}2\}$ facets become lower in energy than even the stoichiometric $\{10\bar{1}0\}$ surface. However for the $\{11\bar{2}2\}$ pyramidal facets, to completely geometrically exclude the $\{10\bar{1}0\}$ facets from the Wulff construction, $\gamma_{(11\bar{2}2)}$ must be considerably lower than $\gamma_{(10\bar{1}0)}$, satisfying the inequality, $\frac{\gamma_{(10\bar{1}0)}}{\gamma_{(11\bar{2}2)}} \geq \frac{2}{\sqrt{3}}\sqrt{1+\left(\frac{a}{c}\right)^2}$ (≈1.36 for ZnO). This condition is not met in the plot in Fig. 3.7, but it is not necessary for the $\{10\bar{1}0\}$ facets to be completely excluded for the crystals to grow in a pyramidal morphology. Figure 3.7 (b) shows the height/width and the $\{11\bar{2}2\}$/$\{10\bar{1}0\}$ area ratio of the Wulff construction (Figure 3.7 (c)) plotted on the same x-axis. Under the oxygen-starved growth conditions, the equilibrium morphology of ZnO crystals transitions from rod-like to compact pyramidal structures marked by the drastic increase in the fraction of semi-polar $\{11\bar{2}2\}$ surfaces.

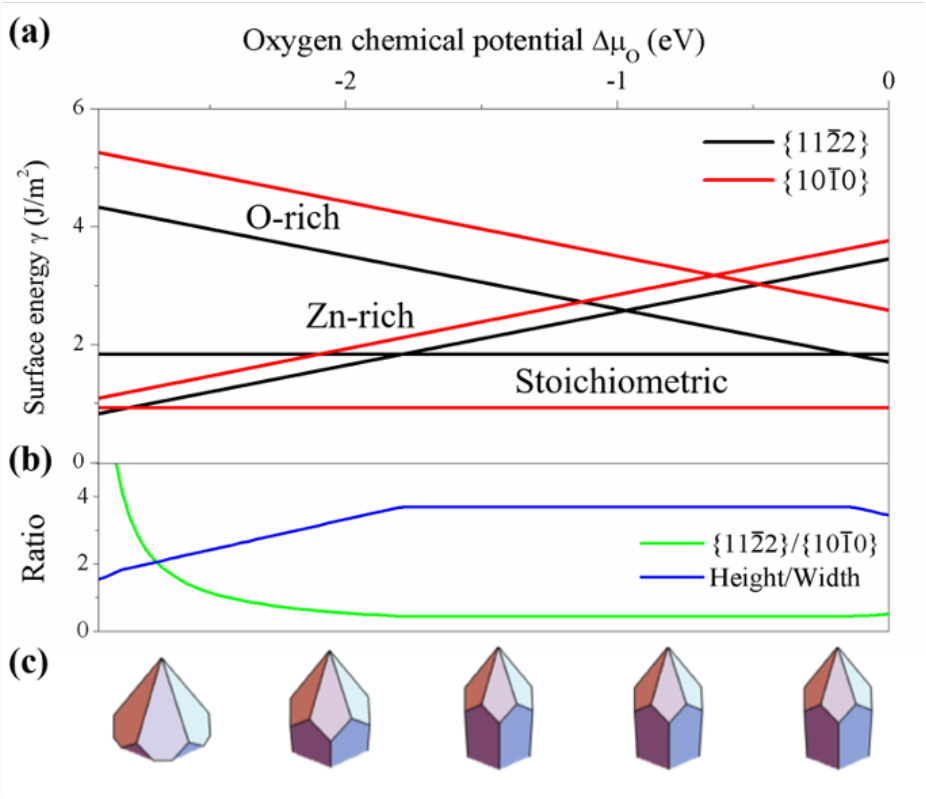

Figure 3.7, (a) Plot of the surface energy of the $\{11\bar{2}2\}$ (black) and $\{10\bar{1}0\}$ (red) facets as a function of oxygen chemical potential, (b) corresponding surface area (green) and aspect ratio (blue), and (c) corresponding Wulff construction.

The DFT calculations anticipate that ZnO with high-index $\{11\bar{2}2\}$ surface planes can be synthesized when the chemical potential of oxygen is low. This prediction is consistent with the experimental results. ZnO pyramidal structures are successfully synthesized when the Zn vapor partial pressure is significantly higher than that of oxygen near the substrate. This extremely biased precursor ratio environment is achieved by modifying the design of the CVD reactor. The prevention of the premature oxidation of Zn precursor plays an important role in growing the ZnO crystal with $\{11\bar{2}2\}$ surfaces by creating an environment with highly concentrated Zn vapor. When the crystals are removed from the reactor and

exposed to air, the surfaces quickly oxidize and become stoichiometric, but the crystal morphology remains in the pyramidal shape.

3.4 Prediction of Photoelectrochemical Activity

The electrostatic potential of the DFT computed stoichiometric $(10\bar{1}0)$ and $(11\bar{2}2)$ surfaces was analyzed to determine which structure has the highest polarity and greater photoelectrochemical activity. Only stoichiometric planes are considered because although we predict that the pyramidal morphology is stabilized during growth in oxygen-deficient conditions, these surfaces will quickly become stoichiometric under ambient conditions. Fig. 7 shows the atomic structure of each surface with the left-hand side of each plot showing the surfaces' local electrostatic potentials plotted on the surface of constant charge density. The charge density contour value is the same for all plots. The color scale indicating the local voltage is the same for all surfaces. It is observed that the two $(11\bar{2}2)$ surfaces present a wider variation in the local electrostatic potential than the $(10\bar{1}0)$ surface. The compactly co- ordinated and charge-balanced structure of the $(10\bar{1}0)$ surface offers smaller variation in the surface potential presented to water molecules than both the Zn and O terminated stoichiometric $(11\bar{2}2)$facets which are polarized. The results are supportive of the observations that both Zn- and O-terminated $(11\bar{2}2)$ surfaces are more reactive than the $(10\bar{1}0)$ non-polar facet. Therefore, the $(11\bar{2}2)$ facets are more likely to react with water molecules and are more suitable for water splitting applications.

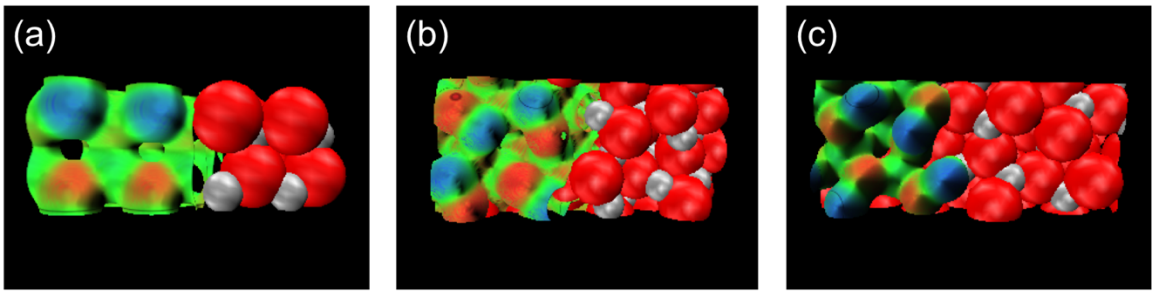

Figure 3.8, Electrostatic potential on the stoichiometric ZnO facets (left side of the surface) and atomic locations with red atoms indicating O and silver for Zn (right side) on the surface of (a) $(10\bar{1}0)$, (b) Zn-terminated $(11\bar{2}2)$, and (c) O-terminated $(11\bar{2}2)$.

3.5 Conclusions

Although the pyramidal structures with $\{11\bar{2}2\}$ facets are generally not stable due to their relatively high surface energy, our DFT calculations show that these morphologies are stabilized under a Zn-rich growth condition. The Wulff crystal structures show a transition to eliminate $\{10\bar{1}0\}$ nonpolar facets and form pure pyramidal structures with $\{11\bar{2}2\}$ semi-polar surfaces as the environment becomes oxygen-deficient. Our results suggest a correlation between the growth condition and the final morphology of materials. Using this correlation, we tailored the structure to obtain materials that are normally unstable and difficult to grow. The larger variations observed in the electrostatic potentials at the surface of $\{11\bar{2}2\}$ semi-polar surfaces indicate their higher reactivity compared with the $\{10\bar{1}0\}$ non-polar surfaces. The nanopyramidal ZnO with semi-polar $\{11\bar{2}2\}$ facets were experimentally synthesized by our collaborators through creating an oxygen-deficient environment for improved photocatalytic performance, which validates our predictions.

4. Surface Structure and Electrical Transport Property Relationships in Diamond-based Heterostructures

4.1 Overview

Surface Transfer Doping (SD) and delta doping are critical methods used for doping diamond for transistor applications. The SD technique, a thin film of acceptor layer is interfaced with the hydrogenated diamond surface which creates a high-mobility two-dimensional hole gas (2DHG) channel at the interface. H-diamond has been extensively studied for fabrication of high-power and high-frequency field effect transistors (FETs). The C-H dipoles at the surface of H-diamond reduces the electron affinity in the surface layer inducing p-type doping in this region and facilitates SD. Recent studies are targeted towards improving the stability and conductivity of the 2DHG channel as important factors in designing diamond-based electronic devices. A 2D surface used in combination with H-diamond can act as either an acceptor layer to enable SD or as a cap layer to prohibit atomic interactions between the acceptor layer and the H-diamond surface. The choice of the 2D layer material and surface crystal orientation are important in determining its functionality. A recent experimental study reported an improvement in the homogeneity and carrier mobility of the 2DHG channel at the diamond surface when using an hBN layer as a gate dielectric in diamond FETs. Their results show that even at low temperatures, the channel remains conductive over the period of time [19], [63]. In addition, studies show a thin layer of h-BN, when interfaced with H-diamond, offers an improvement in device parameters

through enhancement of charge concentration and mobility, and reduction of surface scattering [64].

Despite these experimentally demonstrated improvements on the overall performance of the diamond devices, a theoretical effort dedicated to the study of structural and electronic properties of 2D/H-diamond heterostructures with an atomistic resolution, particularly with h-BN as the 2D layer, is still lacking. In this chapter, we investigate the possibility of using hexagonal Boron Nitride as a cap layer to preserve the 2DHG channel at the surface of H-diamond (100) surface. Here, we present three papers. In the first manuscript, we investigate the structural and electronic properties of an hBN (graphene) layer interfaced with H-diamond (100) surface. Particularly, we demonstrate that both hBN and graphene can be used as interfacial (cap) layers to maintain the 2DHG channel across the interface. We also observe a corrugation (rippling) in the 2D layer to mitigate the unavoidable applied strain during modeling. In the second paper, we examined the effects of the 2D layers' rippling on the electronic structure of the isolated 2D layers and 2D/H-diamond (100) heterostructure. Finally, in the third paper, we analyze the effect of surface termination on structural and electronic properties of diamond (100) and hBN/diamond (100) systems.

4.2 Structural Modeling and Computational Details

To identify the optimal strain-compensated h-BN (graphene)/H-diamond (100) heterostructures, we performed a full analysis of the structural alignments of the 2D layers on the H-diamond (100) surface. Prior to the formation of the heterostructures, we generated the reconstructed 2×1 H-diamond (100) system with in-plane lattice constants of a = 5.04 Å and b = 2.52 Å and a thickness of ~10 Å (10 carbon layers) which exhibits the desired bulk-

like electronic properties and is consistent with the earlier publications.[65] Following that, we constructed a supercell of 5×1 2D layers on $2\sqrt{2} \times 1/\sqrt{2}$ unit cells of 2×1 reconstructed H-diamond (100) surface with edges along the $[011]$ and $[0\bar{1}1]$ directions. The selected structures are the ones that balance system size and computational expense with minimization of lattice mismatch while accommodating the 2×1 reconstruction of (100) diamond. Starting with the h-BN $[2\bar{1}\bar{1}0]$ along the diamond $[011]$ direction (which we take as the *x*-direction) the h-BN sheet is rotated anticlockwise by 26.6°, and then the rotated sheet is strained in compression by 10.2% along the *x*-axis and stretched by 3.7% along the *y-axis*. Due to the similarity between the B–N and C–C bond lengths in h-BN and graphene (1.45 and 1.42 Å, respectively), the same alignment was chosen for the graphene layer which was achieved with a compression of 8.3% along *x* and a stretch of 5.9% along *y* after rotation. The stages for bringing the hBN layer into registry with the H-diamond (100) surface are illustrated in Figure 4.1(a-c).

The final step in constructing the strain-compensated heterostructures was to find the lowest energy alignment of the 2D layer on the H-diamond (100) surface. To achieve this goal efficiently, we performed a coarse sampling of the potential energy landscape by rastering the position of the 2D layer over the diamond substrate to generate 38 different starting structures. For each resulting structure, the initial 30 steps of structural relaxation were performed, after which the energies were mapped and compared (Figure 4.1 (d)). The aim of this was not to find the minimum energy position, but rather to find the watersheds between different potential energy wells. To gain a better understanding of the structure-energy distribution, we performed the *k*-means clustering method [66], a commonly used

algorithm for cluster analysis that groups similar items into k clusters. The k-means clustering error converged with $k = 4$, i.e., four clusters yield the most accurate partition of the structures, shown in Fig. 4.1 (e). The group of initial structures with the lowest final energies, denoted by "The low energy group", are located on the y = 0.33 line. In other words, we arrive at the lowest energy structures starting from structure for any x shift in the 2D sheet providing the y shift is 0.33 of the box width. This implies that there is little to prevent the sheet from sliding in the x direction during minimization. However, in the 2D/H-diamond (100) heterostructures, the hydrogens are positioned on the outer edges of the H-diamond (100) surface, which is expected to inhibit the atoms in the layer from shifting in y direction during the structure relaxation. Based on this, we selected the structure from this group with the lowest energy and continued its structural relaxation to minimize its energy. As the next step, we found the optimal vdW spacing between the constituent layer and the H-diamond surface. Structures with a vdW spacing of 3.0 Å were found to yield convergence. The H-diamond (100) surfaces were separated by a vacuum spacing of 20 Å to avoid interactions between the adjacent blocks. In all structure relaxation calculations, the surface hydrogens and the first four carbon layers of the H-diamond (100) surface were allowed to relax while the remaining layers of diamond were fixed.

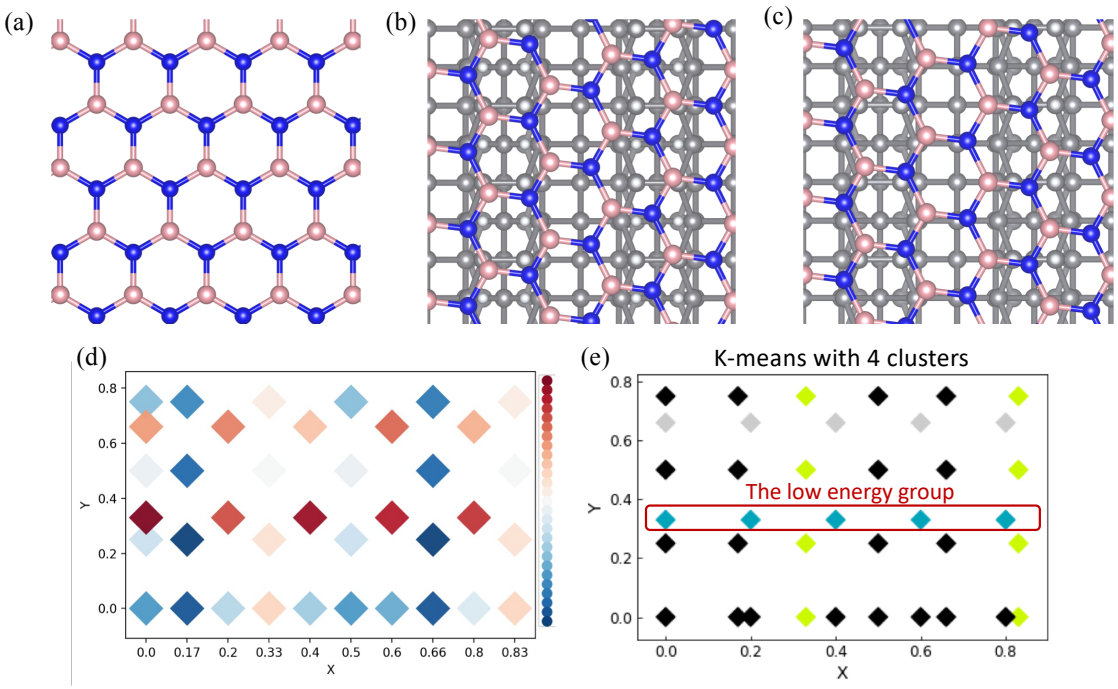

Figure 4.1, Structural alignment analysis of hBN/H-diamond heterostructure. (a) The original planar hBN layer, (b) the strained and rotated hBN layer positioned on top of the H-diamond surface, and (c) the same heterostructure with the layer shifted in y-axis by one-third of the b lattice vector. (d) shows the final energy of structures after 30 steps with different initial positions for the hBN layer relative to substrate. The x and y axes show the initial shift of the 2D layer as fractions of supercell lattice vectors. (e) The k-means clustering (with k=4) for the energies after 30 relaxations steps for the tested structures, showing that the structures shifted in the y axis, disregarding of their alignment along the x-axis, poses the lowest energies.

All the calculations in this paper were performed using the Vienna ab-initio Simulation Package (VASP) implementing the Perdew-Berke-Ernzerhof (PBE) general gradient approximation (GGA) exchange correlation functional [54]–[56], [58], [67]. A plane wave cutoff energy of 520 eV was used. For the individual constituent system (unitcell of h-BN or graphene), a 12×12×1 Gamma-centered mesh of k-points was found to yield a well-converged structure with an accuracy of 10^{-4} eV. Accordingly, for the heterostructure, a 4×12×1 grid of k-points is expected to provide sufficient accuracy and was used to sample the Brillouin zone (BZ). In order to include the van-der-Waals (vdW) forces during structural and electronic properties calculations, we have adapted the Grimme's D2

approximation [68]. All the structures were optimized using the conjugate gradient algorithm [62] to minimize the forces for ionic relaxation to better than 1×10^{-5} eV/Å. The electronic properties such as band structure, projected density of states (PDOS), and the charge (potential) profile normal to the 2D/H-diamond (100) interface, were calculated using a denser K-point mesh to increase the accuracy. To correct the band gap underestimation by the PBE functional, we used the HSE06 hybrid functional to compute the electronic properties after ionic relaxation.[69] We used the Grimme's D2 approximation [68], zero damping DFT-D3 [70], and DFT-D3 with the Becke-Jonson (BJ) damping [71] in order to include the effect of van der Waals interactions between the layer and the H-diamond surface. To include SOC in band structure calculations of graphene, we used the SOC implementation in VASP [72]. The charge transfer between the H-diamond (100) surface and the 2D layer was quantified using the Bader charge analysis [73].

4.3 Structural and electronic properties of 2D/H-diamond heterostructures

Recent studies suggest using a thin layer of 2D materials as the gate dielectric layer to mitigate the limitations of oxide-based acceptor layers [19], [63]. These studies report improvements in device parameters such as 2DHG channel carrier densities and mobilities. Motivated by these experiments, recent theoretical modeling based on effective mass approach predicted that a thin layer of 2D layer as an interfacial capping layer can minimize the impact of interface roughness, or even facilitate the charge transfer across the H-diamond/acceptor layer interface and improve the sheet hole concentration [64], [74]. Despite proofs of improved device performance, a theoretical effort to study the structural and electronic properties of 2D/H-diamond heterostructures with an atomistic resolution,

particularly with hBN as the 2D layer, is still lacking. Furthermore, a fundamental understanding of the structural alignment and charge transfer between the 2D layer and H-diamond is key to the successful integration of 2D layers in the next-generation scalable SD-based diamond devices.

The (111) and (100) facets are the most common diamond surfaces in the device community. Though the hexagonal 2D layers are crystallographically compatible with the (111) facet, complex surface reconstruction mechanism and surface structural properties make it less desirable for the device design. In addition, this surface also suffers from high structural defects and low structural stability [75]. On the other hand, the (100) facet is the dominant surface in the experimental growth of diamond films via chemical vapor deposition [76], [77] and exhibits smooth bulk-like to (2×1) reconstruction, resulting in carbon double bonds (C=C) at its surface [78]. Besides, the high stability of the 2×1 reconstruction of the (100) surface enables the growth of defect-free facets during fabrication [79] [80]. This surface undergoes a 2×1 surface reconstruction that affects the pattern of H termination. Despite these advantages, which makes (100) the most technologically important diamond surface, the lattice mismatch in the hexagonal 2D layer on the diamond complicates the computational studies. As a result, recent computational studies on 2D/diamond heterostructures have utilized the (111) diamond facet to mitigate the interfacial strain [42], [81], [82]. Motivated by this, we study the structural and electronic properties resulting from the integration of hBN and graphene on the H-diamond (100) surface using the first principles simulations.

4.3.1 Structural Properties of hBN(graphene)/H-diamond

Figure 4.2 depicts the relaxed structure of graphene/H-diamond (100) and hBN/H-diamond (100) heterostructures, respectively. After undergoing the transformation to bring the 2D layer into registry with the H-diamond (100) surface, the heterostructures, with an optimized vdW-gap (δ) of ~3 Å, were fully relaxed during which both the hBN and graphene sheets developed a corrugation perpendicular to the compressive axis. The corrugated (buckled) alignment observed here occurs to relax residual compressive strain imposed by the periodicity of the supercell. Similar substrate-induced corrugation or rippling of graphene layer was also observed in the epitaxial growth of graphene on Ge [83], and SiC substrate [84], and a DFT study of graphene on diamond (111) surface [85]. Though this atomic distortion results in the modification of the local potential within the layer, it does not have a noticeable effect on the electronic properties as discussed later in this chapter.

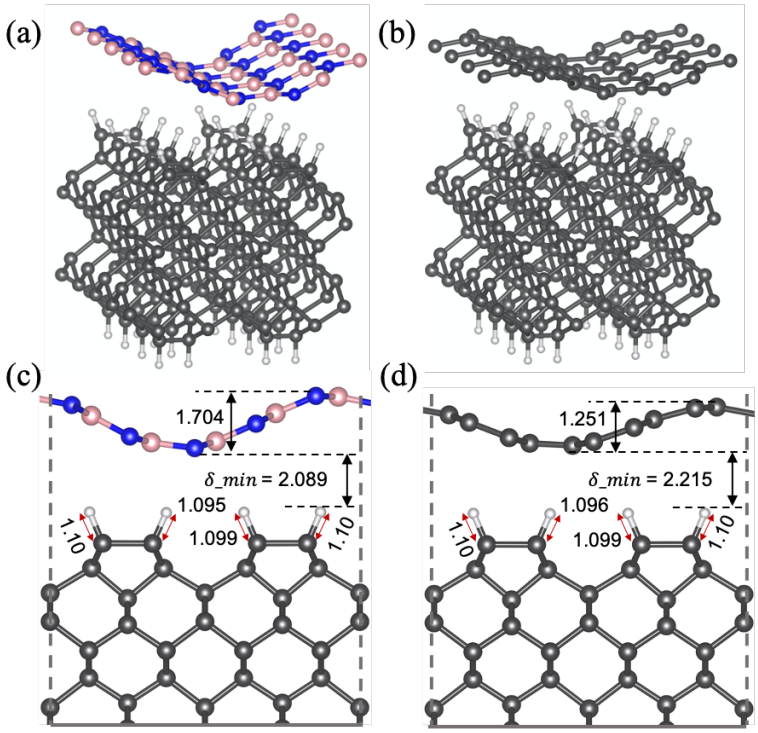

Figure 4.2, Atomistic structures of optimized 2D/H-diamond (100) Heterostructures. Three dimensional and side views of the optimized (a, c) graphene/H-diamond (100), and (b, d) hBN/H-diamond (100) heterostructures. The C-H bond lengths, peak to valley distance of the rippling curvature, and the minimum vdW spacing after rippling (δ_{min}) values are annotated on the figures. All distances are in Å. The hydrogen, carbon, boron, and nitrogen atoms are shown with white, gray, pink, and blue colors, respectively.

To correlate the magnitude of rippling of the 2D layers to the layer adhesion energy, the adhesion energy per-atom (E_{ad}) is evaluated using the equation [85],

$$E_{ad}(E_{vdW}, E_{binding}) = \frac{1}{n}(E_{S/D} - E_S - E_D) \tag{4.1}$$

where E_D, E_S, and $E_{S/D}$ are the total energy of the H-diamond (100), 2D layer, and the 2D/H-diamond (100) heterostructure, respectively. The term n is the number of atoms in the 2D layer. The per atom adhesion energy of graphene on the H-diamond (100) surface was found to be -0.0314 eV, which is comparable to the reported value (-0.05 eV) for the similar system [81]. The variation in the adsorption energy values comes from the

difference in the interfacial strain due to the unreconstructed and bulk-like used in Ref,[81] which is distinctly different from the experimentally observed, reconstructed (2x1) surface used in this study. For the hBN on H-diamond (100) system, the observed per atom adhesion energy was -0.0396 eV, indicating a slightly stronger interaction between the hBN layer and the H-diamond surface. In both cases, the trough of the ripple was aligned between the rows of reconstructed C–C bonds on the substrate. The minimum vdW-gap (δ_{min}) at the valley of the corrugation is 2.215 Å and 2.089 Å for graphene and hBN, respectively, as illustrated in Figs. 1 (c) and (d). The amplitude of the observed ripple in graphene is smaller than hBN due to the lower compressive strain imposed on the graphene layer required to make it commensurate with the diamond surface. The bending of the sp^2 bonds in the rippled sheets distorts the orbital hybridization of the atoms in the locations where the curvature is large, leaving orbitals free to participate in bonding with the substrate.

4.3.2 Electronic Transport Properties of hBN(graphene)/H-diamond

Using the optimized geometries and corresponding self-consistent charges, we calculated the band structures of 2D/H-diamond (100) heterostructures (Figure 4.3). The band structure of the pristine rippled graphene supercell is overlaid over that of the graphene/H-diamond (100) in order to analyze the effect of heterogeneity on the shape and slope of the Dirac cone at K', as illustrated in Fig. 4.3 (a). The overall characteristic of the single-layer graphene is preserved in the graphene/H-diamond (100), while the primary Dirac point is shifted below Fermi-level by 0.13 eV. This generates weak n-type doping of the graphene layer, indicating the effect of charge transfer across the vdW-interface (Figure 4.3 (a)

inset). The magnitude of graphene doping is consistent with the recent experimental report on graphene/H-terminated (111) system [86], [87]. This charge transfer induced doping of pristine graphene is consistent with earlier studies on graphene-based vdW heterostructures [88]–[92]. Even though an intrinsic, defect-free graphene layer is gapless, a small gap opening of 10 meV was observed around the Dirac cone for both the rippled graphene supercell and graphene/H-diamond (100). The small gap around the K' point, which is less than half of the room-temperature thermal energy, is consistent with other works where the induced gap is attributed to the hybridization of π and σ orbitals [81], [93], [94], and the spatially varying potentials [95], [96] introduced by strain and ripples. If the graphene layer is grown large enough or the substrate is designed to minimize the strain, this gap can be suppressed, and hence, the graphene/H-diamond (100) heterostructure can be deemed as a semi-metallic system. This observation is consistent with the previous studies on graphene-based heterostructures [81], [84], [97].

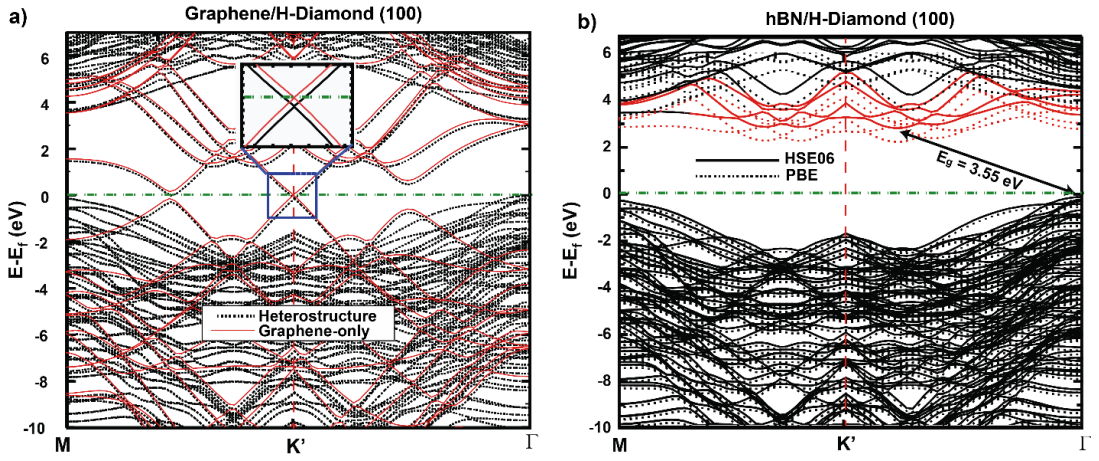

Figure 4.3, Band structures for (a) graphene/H-diamond (100) and (b) hBN/H-diamond (100) heterostructures. In (a), the red solid and black dotted lines represent the band structures for rippled graphene supercell and graphene/H-diamond (100) heterostructure, respectively. In (b), the solid and dotted lines represent the band structures for hBN/H-diamond (100) using HSE06 and PBE functionals. Contributions from the hBN layer to the CBE states are presented with the light (red) lines.

The band structure for the hBN/H-diamond (100) is illustrated in figure 4.3 (b). Here, to highlight the role of the exchange-correlation term on the band edges, we plotted the band structures calculated from both the local functional (PBE) and hybrid functional (HSE06). The HSE06 functional increases the fundamental energy gap (E_g) of the hBN/H-diamond (100) by ~30% to 3.5 eV compared to the PBE functional. The main contributions to the scaling originate from the CB states. Similar exchange-correlation related up-scaling of energy gaps was observed for the bulk diamond and H-diamond (100) systems. Quantitatively, the energy gaps increased from 4.2 and 2.6 eV (PBE) to 5.3 eV and 4.2 eV (HSE06) for bulk diamond and H-diamond (100), respectively. Other theoretical studies on wide bandgap semiconductors also reported similar degrees of scaling for the fundamental gaps.[98], [99] Though H-diamond (100) has a direct bandgap with CB minima (CBM) and VB maxima (VBM) located at the Γ-point, a direct-to-indirect energy gap transition

occurs in the hBN/H-diamond (100) system due to the heterogeneity so that the CBE is located between the K' and Γ-points, and the VBE is placed at the Γ -point of the BZ.

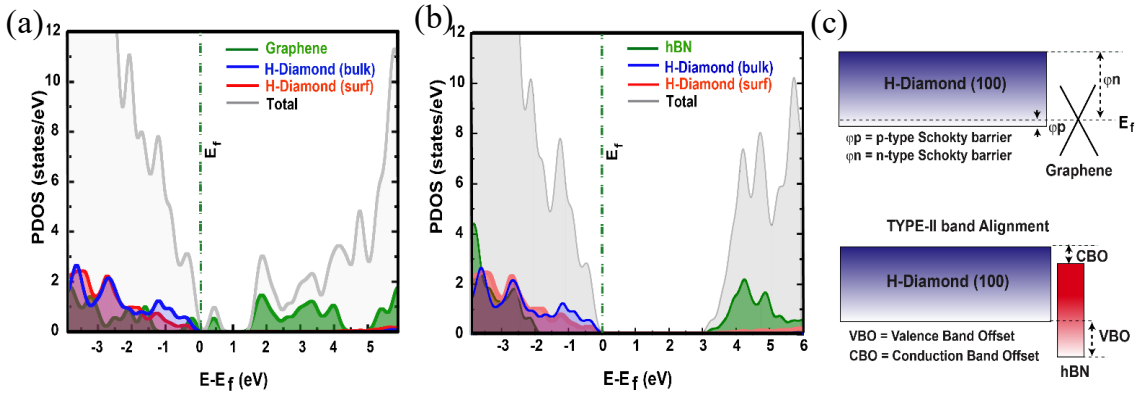

Figure 4.4, Partial density of states (PDOS) plots of surface and bulk atoms in the diamond (100) surface, and the constituent layer for (a) graphene/H-diamond (100) and (b) hBN/H-diamond (100) systems, and (c) band alignment schematics for both heterostructures.

One can gain further insight into the role of the proximal 2D layers in modifying device-related properties by analyzing the site projected partial density of states (PDOS) of the 2D/H-diamond (100) heterostructures. In graphene/H-diamond (100), Figure 4.4(a), most of the contributions to the two peaks around the Fermi-level are from the graphene layer, which is consistent with the observed Dirac cones around the Fermi-level seen in the band structure plot in Figure 4.3 (a). The VB states at the Γ-point of this system are co-located in the vicinity of the C-H bonds in the diamond surface and the graphene layer as illustrated in figure 4.5. These results suggest that graphene could be a very promising material as the metal electrode, and it can enhance the contact performance while maintaining the intrinsic electronic properties of interfaced diamond surface.

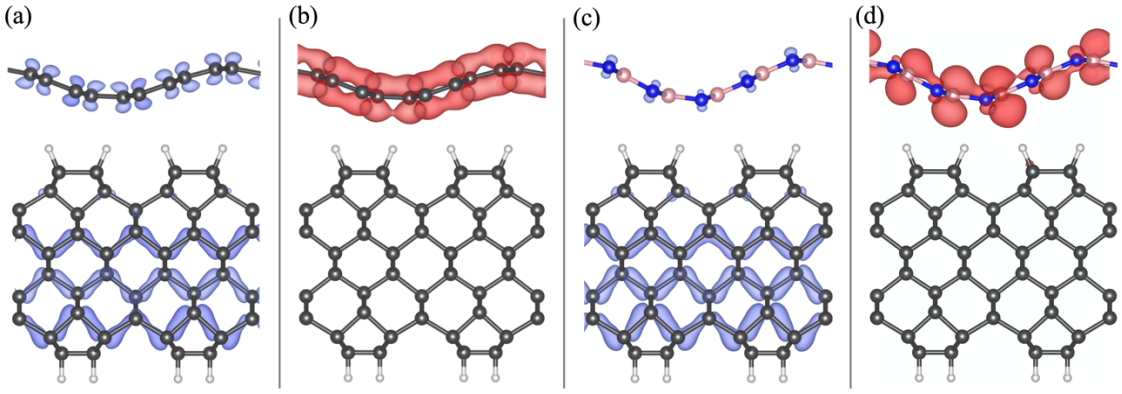

Figure 4.5, Band-decomposed partial charge density visualization, equivalent to the sum of absolute-squared values of wave functions ($|\psi|^2$) over the Brillouin zone, for the highest occupied, i.e. VB, electronic state (blue regions in (a) & (c)), and the lowest unoccupied, i.e. CB, electronic state (red surfaces in (b) & (d)) in the graphene/H-diamond (left-hand) and h-BN/H-diamond (right-hand) systems. Hydrogen, carbon, boron and nitrogen atoms are depicted as white, gray, pink, and blue spheres, respectively.

In contrast to the graphene/H-diamond (100) system, the hBN/H-diamond (100) system exhibits semiconducting properties with a significant energy gap of 3.55 eV, as shown in Fig. 4.3 (b). Although the energy gap is ~15% smaller than the gap of isolated H-diamond (100), it is comparable to other WBG semiconductors such as GaN (3.4 eV) and SiC (3.3 eV) [100]. Here, the hybridized states from the surface and bulk C atoms mainly contribute to the VBE states. On the other hand, the $\boldsymbol{p_z}$ orbitals from the B atoms in the hBN layer contribute to the CBE states and are consequently localized around B atoms in the hBN layer. This is further elucidated by the band decomposed charge densities around the band edges, illustrated in Figure 4.5 (c) and (d). This spatial separation of electrons and holes by more than 5Å in the hBN/H-diamond (100) is highly desirable for minimizing the Coulomb scattering in the channel of the SD-based diamond transistors [63].

In the semi-metallic nature of the graphene/H-diamond (100) system, there are no gap states originating from the graphene layer in the H-diamond (100) gap. As a result, the

Fermi level pinning is minimal, and the graphene layer is expected to act as a metal contact [101], [102]. Here, the n-type (p-type) Schottky barrier, [103], [104], Φ_n (Φ_p) is defined as the energy difference between the CBE (VBE) state of the H-diamond (100) and the Dirac point at the K'-point. The observed Φ_p and Φ_n are 13 meV and 1.73 eV, respectively. The relatively small Φ_p value indicates that the graphene layer in graphene/H-diamond (100) acts as a p-type Ohmic contact. Since the H-diamond (100) band edges are sensitive to the surface and termination types, the graphene/H-diamond (100) exhibits tunable Schottky and Ohmic contacts with promising device applications based on unique and complementary intrinsic properties of graphene and H-diamond (100).

In the hBN/H-diamond (100) system, the CBE and VBE energy levels are primarily composed of the states from the hBN and H-diamond (100) systems, respectively. Furthermore, their energy levels form a TYPE-II (staggered) band alignment, as illustrated in the bottom panel of Figure 4.4 (c). This type of band alignment allows the confinement of electrons and holes in different spatial locations of the heterojunction and is widely used in memory,[105] and unipolar electronic device, [106] applications. The observed CBO and VBO values are 0.1 eV and 1.38 eV, respectively. This indicates higher confinement for holes, (vis-à-vis electrons), in the hBN/H-diamond (100) system. Quantitatively, the observed VBO value is less than the reported value for the Al_2O_3/H-diamond (100) system obtained by analyzing the energy difference between the site-resolved core-level shifts in XPS measurements [15]. Despite this, an hBN layer interfaced with H-diamond offers the advantage of having a low number of charge impurities and dangling bonds. Besides, an hBN layer between the H-diamond and the acceptor layer may serve to protect the

hydrogenated diamond surface and thereby improves the stability of the hole channel preventing charge leakage during the device operation. The hBN/H-diamond (100) heterostructure is also an interesting system to realize interlayer indirect excitons because of the small screening effect and heavy carrier masses in the constituent hBN and H-diamond systems. Furthermore, because of the TYPE-II band alignment between the hBN and H-diamond (100) systems, the spatially separated electrons and holes, as illustrated in Figure 4.5 (c) and (d), form indirect excitons that are strongly bound and are long-lived, as compared to the excitons realized in the III-V and 2D heterostructures [107]–[109].

4.4 Effect of Rippling on Electronic Properties of 2D Layers and 2D/H-diamond Heterostructures

In the previous section, we reported that a sheet of hBN or graphene interfaced with the H-diamond (100) surface—the technologically relevant surface for diamond-based electronic devices—could act as a protective layer that preserves the p-type bulk-like conductivity in the H-diamond (100) surface. During the analysis of the structural alignment of the 2D layers on the H-diamond (100) surface, we also noticed a strain-mediated 2D layer corrugation or rippling. Here, we examine the effects of the 2D layers' rippling on the electronic structure of the isolated 2D layers and 2D/H-diamond (100) heterostructure.

The absence of dangling bonds at the surface of 2D materials enables the stacking and construction of various van der Waals (vdW) heterostructures, even in cases with substantial lattice mismatch [110]. This allows combining different 2D layers with each other or three-dimensional (3D) materials to mitigate limitations in engineering high-power electronic devices [111]. In many cases, such as the presented hBN(graphene)/H-diamond

(100) system, there is a lattice mismatch between the 2D layer and the 3D material [112], [113]. In these cases, even though the weak vdW interfacial bond means that the energy penalty for the mismatch is low, the intrinsically low bending stiffness of 2D materials means that the energy penalty can sometimes be further reduced by buckling the 2D layer to accommodate any compressive strain needed to bring the 2D layer and substrate into registry. Moreover, rippling is a common occurrence in computer simulations of 2D heterostructures as an artifact of the periodic boundary conditions and the need to enforce lattice matching in a computationally tractable system size. In either case, elucidating the effects of rippling on electronic structure is essential for understanding the resulting heterostructure's electrical transport properties. If the ripples are real, we need to understand them, and if rippling is an artifact of computation, we need to be able to discount the ripple's effect from any predictions made or inferences drawn.

In experiment, ripples are observed both in free-standing graphene due to instability of the 2D lattice [114] or lattice perturbation [96], and in 2D-based heterostructures, due to the interaction with the underlying substrate such as SiC (0001) [84], and Ge [83]. Rippling in graphene interfaced with Ge substrate was found to result in a slight n-doping of graphene in the rippled regions [83]. Since the ripples are developed in response to an external perturbation, they could potentially affect the electronic properties and subsequently the device performance. Controlling the degree of rippling in graphene is suggested as a way to engineer devices with tailored bandgaps and functionality. A previous study reported generating controlled ripples in suspended graphene through thermally applied strains [96].

In computation, the generation of large strains is an unavoidable part of modeling heterostructures with lattice mismatch. Understanding how ripples affect a system's properties helps drawing a better comparison between the computational predictions and real-world applications. Previous theoretical studies have focused on elucidating the thermodynamic and mechanical properties of rippled hBN [115], [116]. Others have studied graphene under an imposed modulated potential with a similar wavelength to the ripples in our work, finding that the imposed potential opens the Dirac cones at k-points that are not parallel to the wavevector of the modulation [95]. Going beyond these works, in this paper, in addition to studying the effect of the ripples on the 2D layer, we elucidate their impact on the computed interaction of the 2D layer with a substrate. One merit of this is to determine whether rippling works in favor of electronic devices. In this case, to obtain better charge transfer properties, we can experimentally devise device geometries with the layers forced to form ripples under some geometrically imposed strain.

To understand the effect of rippling on the heterostructures' structural and electronic properties, we provide a comparison against the generated models with a strained-planar hBN (graphene) layer. To obtain these, the structures were relaxed, with the atoms in the 2D layer permitted to move in plane but constrained from moving out of plane. To differentiate the former and latter heterostructures, hereon, we refer to them as wavy and planar hBN(graphene)/H-diamond (100), respectively. The results and discussions are presented in two sections, structural properties, and electronic structure of the isolated layers and the resulting heterostructures.

4.4.1 Effect of Rippling on Structural Properties

To understand the effect of the 2D layers' rippling on the heterostructures, we need to evaluate each contributing factor to the layers' transformation and the heterostructures' construction. Hence, we computed the energy at each step of the process for mating the 2D layer with the diamond substrate. Figure 4.6 shows the stages for transforming the hBN (graphene) layer and aligning the transformed layer on the H-diamond (100) surface. As illustrated, the contributing factors include imposing strain on the layer, full relaxation of the layer through which the layer develops a rippled structure, adhesion of the layer on the H-diamond surface, and the vdW interaction between the constituent layer and the substrate.

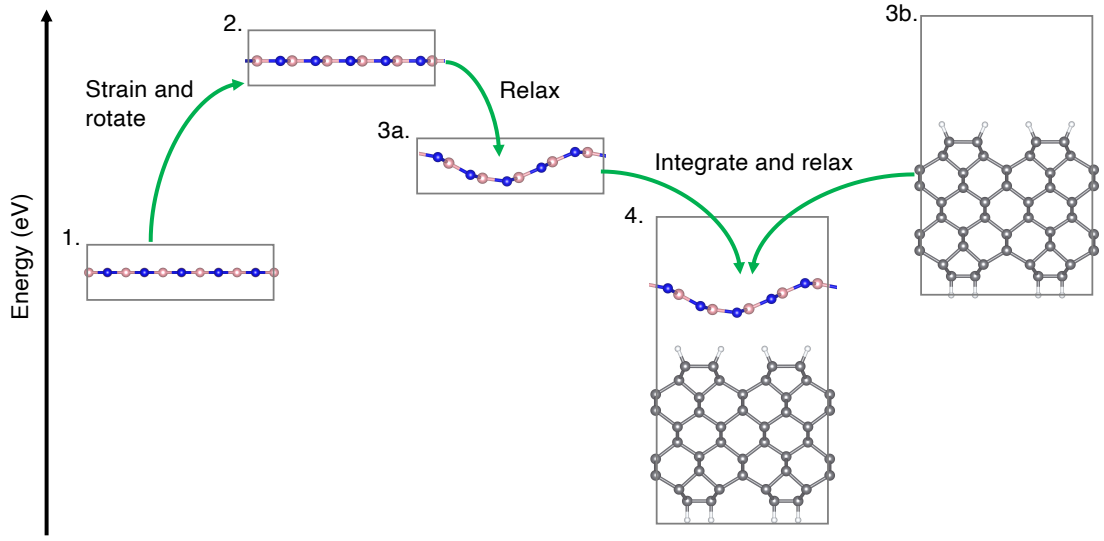

Figure 4.6, Hypothetical energy path for 2D layer (here hBN) and H-diamond (100) integration by straining a monolayer and integrating. it with H-diamond (100) surface to generate the hBN/H-diamond (100) model.

The strain energy is defined as the energy gained when the layer is strained (Figure 4.6, subsets 1 and 2). The energy released when the strained layer develops ripples is considered as the rippling energy, equivalent to the energy difference between stages 2 and 3b in

Figure 4.6. The adhesion energies (E_{ad}) and vdW energies (E_{vdW}) were computed using equation 4.1. To compute the adhesion energy values, the fully relaxed atomic structure for the layer and H-diamond (100) surface prior to integration, illustrated in Figure 4.6, 3a. and 3b., were used as E_S and E_D, respectively. Whereas, to evaluate the vdW interaction strength, we used the frozen atomic structure of the constituent layer and the substrate isolated from the fully relaxed 2D/H-diamond (100) heterostructures. For consistent evaluation, the energy values were normalized with respect to the number of atoms in the layer.

To understand the effect of the vdW correction scheme on the structural properties, we evaluated the adhesion energies of simulations with DFT-D2, zero damping DFT-D3, and DFT-D3 with the Becke-Jonson (BJ) damping (Table 4.1). The results indicate that the choice of vdW correction, at least within the tested approaches, does not significantly affect the adhesion energies. Quantitively, the change in adhesion energy was 0.008 eV. In addition, we did not observe a significant difference between the relaxed structures using different vdW corrections. Since all the correction schemes resulted in similar adhesion energy and vdW gap, we have selected the D2 correction scheme for our work.

Table 4.1, Adhesion energy (E_{ad}) of the studied hBN (graphene)/H-diamond (100) heterostructures computed using Grimme D2, Grimme D3 with zero damping, and Grimme D3 with the Becke-Jonson (BJ) damping vdW correction schemes.

System	$E_{ad}(D2)$ (eV)	$E_{ad}(D3)$ (eV)	$E_{ad}(D3-BJ)$ (eV)
Planar hBN/H-diamond (100)	-0.0411	-0.0394	-0.0369
Wavy hBN/H-diamond (100)	-0.0396	-0.0330	-0.0317
Planar Graphene/H-diamond (100)	-0.0372	-0.0380	-0.0360
Wavy Graphene/H-diamond (100)	-0.0314	-0.0351	-0.0340

The energy values for all contributing factors are presented Table 4.1. The results show a higher energy cost to enforce epitaxy on the hBN layer compared with graphene due to a larger imposed strain on the hBN layer. Rippling of the strained layers lowers the energy and makes the structure more stable. The process of rippling in the hBN and graphene releases 0.112 and 0.047 eV/atom of energy, respectively. The larger energy loss during rippling in hBN is caused by the higher applied strain during modeling. Although the energy gain through imposing strain on the layers is not fully compensated by the rippling, the negative values of adhesion energies indicate that the adhesion is exothermic and hence energetically favorable for all the studied heterostructures. Here, in addition to the adhesion energy, which incorporates all the contributing factors, including the lattice deformation (buckling) and the vdW interactions, we also computed the energies for the bare contribution of the vdW interactions. Although the adhesion energy values are slightly stronger for

the heterostructures constituting of planar layers due to strain and buckling effect, the average vdW interactions between the constituent layer and the H-diamond surface are stronger for the heterostructures composed of wavy layer. In addition, for both planar and wavy models, the adhesion and vdW interactions are stronger in the heterostructures composing of hBN as compared with the ones with a graphene layer. The higher interaction between hBN and H-diamond surface can be related to the higher degree of rippling, as well as the polar nature of hBN. These results are consistent with an earlier study which predicted enhancement of binding strength for adhesion of Hydrogen to rippled graphene compared with a planar layer [117]. The bending of the bonds at the crest and trough of each ripple causes sp^2 to sp^3 orbitals rehybridization, leaving available (free) orbitals to participate in bonding with the substrate. Such improvement in reactivity due to ripples in graphene has been found beneficial for the hydrogenation and dehydrogenation process [117]. A previous study reported a quantified correlation between the graphene rippling degree and hydrogen bonding energy [118].

Table 4.2, Structural analysis of planar and wavy hBN(graphene)/H-diamond (100) heterostructures. E_{ad}, E_{vdW}, E_{rip}, E_{strain} show the adhesion, van der Waals, rippling, and strain energies, respectively. The average value of C – H bond length at the interface of H-diamond is reported in each case.

System	E_{ad} (eV)	E_{vdW} (eV)	E_{rip} $(eV/atom)$	E_{strain} $(eV/atom)$	C – H bond length (Å)
Planar hBN/H-diamond (100)	-0.0411	-0.0323	NA	0.3186	1.1012
Wavy hBN/H-diamond (100)	-0.0396	-0.0378	-0.112	0.3186	1.0992
Planar Graphene/H-diamond (100)	-0.0372	-0.0306	NA	0.2918	1.1010
Wavy Graphene/H-diamond (100)	-0.0314	-0.0404	-0.047	0.2918	1.0999

In addition to evaluating the energy path, to compare the overall stability of the planar and wavy heterostructures, we evaluated their total energies. We also measured the average C-H bond lengths at the surface of H-diamond in the heterostructures, as illustrated in Figure 4.7, the results of which are tabulated in Table 4.2. These show that in the wavy layer/H-diamond heterostructures, the surface C-H bonds are slightly contracted, whereas these bonds in both planar layer/H-diamond systems are slightly stretched compared with the C-H bonds at the bare H-diamond (100) surface with a bond length of 1.10 Å.

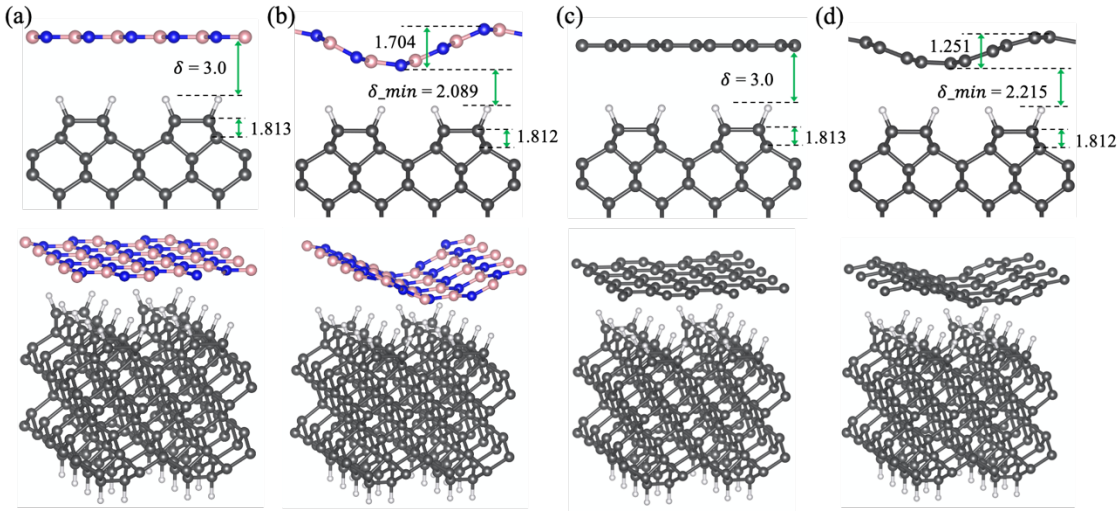

Figure 4.7, Relaxed atomic structures are illustrated. (a, b) Strained-planar and rippled hBN/H-diamond (100), and (c, d) Strained-planar and rippled graphene/H-diamond (100) heterostructures, respectively. Top and bottom panels illustrate side and three-dimensional views of the same structures, respectively.

4.4.2 Effect of Rippling on Electronic Structure

In the following two sections, we present our results on the effect of rippling on the electronic properties of: 1. 2D layers, and 2. 2D/H-diamond (100) heterostructures. We used PBE functional for computing the electronic properties. The PBE functional is well-known for underestimating the band gap. However, since our goal here is to draw a clear comparison rather than providing exact values, the PBE functional was found to provide sufficient accuracy while being computationally more affordable. To prove the validity of this claim, we compare the results computed using PBE [58], and HSE06 [69] functionals for the 2D layers, which require less computational resources as compared with the heterostructures.

To elucidate the effect of strain and rippling on the electronic properties of the 2D layers, we calculated and compared the electronic band structures for the planar and wavy hBN (graphene) layers. In pristine (planner) graphene, the Dirac cone is located at the high symmetry *K* point at the corner of the first Brillouin zone (BZ). However, straining the

graphene layer distorts the perfect honeycomb lattice and BZ of the planner graphene, shifting the K point to a new position, as shown in Figure 4.8 (a). On computing the band structure at this position in the BZ, one finds a small apparent band gap opening in both the planar and rippled graphene. Though this gives an impression of strain-induced band gap opening, this is mainly due to a subtle shift in the location of the Dirac cone to new locations that we call K_S in the strained planar unit cell and K_R in the 5x1 supercell of rippled graphene.

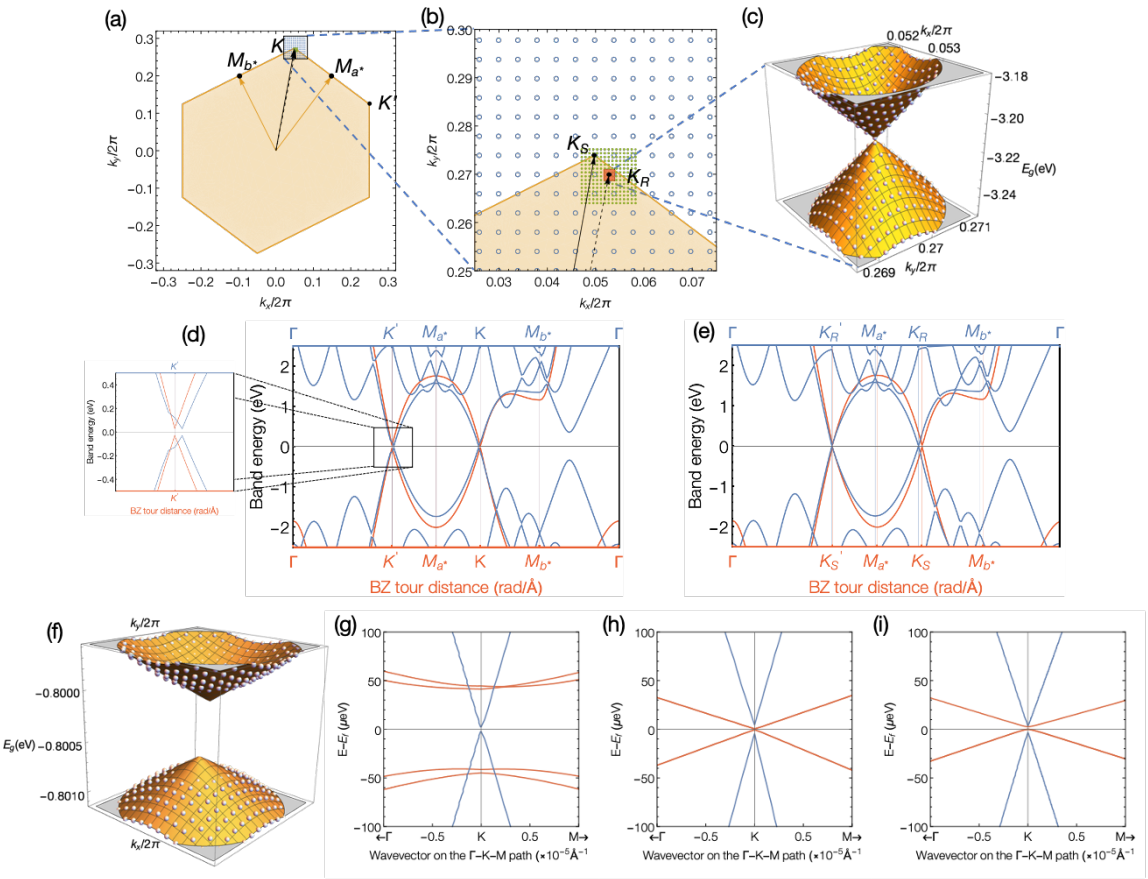

Figure 4.8, The band structure and Dirac cone of rippled and strained but planar graphene in isolation. Plot (a) shows the Brillouin zone (BZ) of the graphene unit cell rotated and distorted so that the 5x1 supercell of graphene is commensurate with the diamond substrate. Plot (b) shows a zoom in of the region around the K point that was covered by the first Dirac cone search mesh. The search points after the 1st and 2nd mesh refinement are plotted in green and red. Also shown at point K_R is the location of the Dirac cone in the rippled graphene. Plot (c) shows a 3D image of the valence and conduction bands in the most refined k-point mesh. The spheres show the DFT computed band energies, and the surface plot is the fit of the distorted cone (Eq. 1) to these points. Plot (d) show the band structure along a path to the BZ corners for the strained unit cell (orange) and the effective (unfolded) band structure for the 5x1 rippled graphene (blue) along the same k-path (for clarity, the band weights for unfolded case are not shown as they are in fig.5). Plot (e) shows the same data as in plot (d) except that the path runs to the locations of Dirac cone at K_S and K_R of each material rather than to the BZ corner. From these latter band tours, it becomes clear that there is no band gap. As the two paths in (d) are slightly different the It can be seen that the way points along the path length do not line up exactly. Plot (f) shows the 3D image of the valence and conduction bands with spin-orbit coupling. Plots (g-i) show the zoomed band structure in the vicinity of the Dirac point $K(K')$ for the unstained, strained-planar, and rippled graphene (unfolded), respectively. In plots (g-i), orange lines indicate calculations including spin-orbit coupling, whereas blue lines represent calculations without spin-orbit coupling.

To find the true location of the Dirac cone, we computed the band energies on a fine mesh of k-points surrounding the corner of the strained BZ, and then fit the equation of a strained and biased cone to the conduction and valence band energies at these *k*-points. The fitting function had the form:

$$E(k) = E_o + g\,|L \cdot (k - k_o)| + s \cdot (k - k_o), \tag{4.2}$$

where the vector s describes the bias or tilt to the cone, and matrix $L = \begin{bmatrix} \varepsilon_{11} & \varepsilon_{12} \\ \varepsilon_{12} & \varepsilon_{22} \end{bmatrix}$ describes the cone distortion. Terms k_o and E_o give the location and energy of the cone's apex. After fitting, the location of the cone center at k_o was taken as the center for generating a second refined *k*-point mesh and the process was repeated as shown in Figure 4.8. By the third mesh refinement, we identify a true gapless Dirac cone. Independent fits to the valence and conduction bands (Figure 4.8, (c)) produce cones with E_o and k_o that are identical for both the strained-planar structure (K_S) and the rippled supercell (K_R), that is, they align perfectly in $\boldsymbol{k}$ and their apices meet. The elliptical distortion of the Dirac cone can be seen clearly in Figure 4.8 (c). Although it is enough to see an *apparent* band gap opening, K_S is only minutely shifted from the BZ corner at *K*, and it is likely that this difference is due to rounding error in the specification of the lattice vectors. However, for the rippled 5x1 supercell of graphene the *K* point is folded into the interior of the supercell's BZ, and so is no longer anchored to a high symmetry point of the BZ. In this case the location of the Dirac cone is no longer constrained by symmetry, and we find that K_R is significantly displaced from the corner of the strained unit cell's BZ as can be seen in Figure 4.8 (b). Figure 4.8 (d) and (e) show the band structures of the strained and rippled

graphene in isolation. Figure 4.8 (d) shows a conventional tour through the high symmetry points in the strained BZ, while plot Figure **4.8** (e) shows the band tour that is directed through the true Dirac cones at K_S, K_S', K_R and K_R'. It can be seen how these shifts in the Dirac cone can mislead one to believe that a band gap has opened when in fact it has not. It highlights that, when computing the band structure of graphene in other situations, one must take care to search around the *K* point before one can confidently identify a true band gap opening. This process may have been overlooked in some earlier works, and may require re-evaluation [93], [119], [120]. It is also interesting here that, in contrast to the effect in a graphene superlattice formed with a modulated potential [95], the Dirac cones at all six of the high symmetry points in the BZ remain intact. The band structures in Figure 4.8 also show that strain causes a significant distortion in the band structure away from the Dirac cone, inducing a large difference in the size of the vertical gap at the M_{a^*} and M_{b^*} points. With these large changes brought about by strain, it is all more remarkable that the Dirac cone is robust to both straining and rippling.

We evaluated the effect of including spin-orbit coupling (SOC) in calculating graphene's band structure, as illustrated in Figure 4.8 (f – i). Inclusion of SOC might induce an additional gap opening at the Dirac cone and cause a band splitting [121]. Previous *ab initio* studies report an SOC induced gap in range of 25 to 50 μeV [122]. Including a magnetic field, addition of substrate, lattice distortion, and other changes that cause rehybridization of sp^3 orbitals affects the magnitude of SOC split [121], [122]. We found that including SOC induces a gap and splitting of bands in unstrained, strained-planar, and rippled graphene (Table 4.1). The magnitude of gap and splits depend on the choice of parameters in

DFT calculations. Though the reported values in this work are different from previous studies, we note that the evaluated gaps and splits were negligible or within the resolution of the numerical accuracy for all the cases.

Table 4.3, Spin-orbit induced split (E_{split}), and gap (E_{gap}) for unstrained, strained but planar, and rippled graphene.

System	$E_{split}(\mu eV)$	$E_{gap}(\mu eV)$
Graphene	30	800
Strained-planar graphene	1	8
Rippled graphene	3	25

The band structure of the strained-planar and wavy hBN layers are plotted in Figure 4.9 (b) and (c), respectively. In both cases, the plots were generated from calculations of a 5 × 1 hBN supercell and show the *effective* (unfolded) band structure along a tour of the 1st BZ of the strained unitcell through the points indicated in Figure 4.9 (a). The unfolded band structure of the strained-planer 5 × 1 supercell exactly matched that computed directly in a single strained unitcell. In contrast, the unfolded band structure of the wavy hBN, while containing the same features as the planar hBN, also contains several extra bands that arise from the rippling. The PBE (HSE) measured bandgap values for the unitcell of hBN was 4.66 (5.48) eV—comparable with the experimentally measured gap of 5.9 ~ 6 eV [123], [124]. The PBE measured bandgap of the strained-planar, and wavy hBN layer are 3.96 eV and 4.18 eV, respectively. Using the HSE functional, the energy gaps of the strained-planar and wavy layers increased to 5.34 eV and 5.52 eV, respectively. As compared to the PBE functional, the HSE calculations show a 20-35% increase in the magnitude of the gap,

which is consistent with our previous study [125] and Refs. [98], [99]. An increase in the bandgap value by 0.18 (0.22) eV, using PBE (HSE) functional, is also observed when the strained-planar layer is allowed to fully relax and develop ripples, indicating the negligible effect of the rippling on the magnitude of the gap. However, the strained-planar and rippled hBN layers both show indirect gaps. We also quantified the PBE computed direct gap at the Gamma point to be 4.37 eV and 5.3 eV for the strained-planar and wavy hBN layers, respectively. The direct gap increased by an order of magnitude as compared to the fundamental gap. As illustrated in Figure 4.9 (a), the conduction band minimum (CBM) shifts away from the fermi level by 0.16 (0.21) eV, measured using PBE (HSE) functionals, when the strained-planar layer is allowed to fully relax and develops ripples. The PBE (HSE) computed CBM values with respect to the fermi level are 4.741 (5.513) eV, 3.959 (5.053) eV, 4.179 (5.264) eV for the planar, strained-planar, and wavy hBN monolayer, respectively. Similarly, the valence band maximum (VBM) energy values, relative to their fermi levels, for the planar, strained-planar, and wavy hBN monolayers are -0.22 (-0.253) eV, -0.246 (-0.283) eV, -0.301 (-0.251) eV computed using PBE (HSE) functional. As compared to the CBM energy level, the VBM energy level of the hBN layer is insensitive to structural inhomogeneity such as strain and rippling. In addition, we evaluated the electron affinity (EA) of the hBN layers by computing the energy difference between the vacuum level (V_{Vac}) and the CB edge (E_{CBE}), i.e., $V_{Vac} - E_{CBE}$. The vacuum level is obtained by calculating the planar average of the electrostatic potential across the heterostructure and taking the vacuum potential, V_{vac}, sufficiently far from the surface along the surface normal direction. This concept will be discussed in more details in the following sections. The PBE

(HSE) calculated EA values are 1.104 (0.869) for the planar (EA_{plan}), 1.473 eV (0.953 eV) for the strained-planar ($EA_{str-plan}$), and 1.631 eV (1.079 eV) for the rippled (EA_{rip}) hBN layer. Though the magnitude of EA depends on the choice of functional, using both PBE and HSE functionals yield an increase of EA as the hBN layer is strained and rippled, that is $EA_{plan} < EA_{str-plan} < EA_{rip}$. One might argue that the observed decrease in EA is in contradiction with the increase of CBM energies when using HSE functionals. The non-monotonous decrements in the EA predicted by the HSE functional is a consequence of asymmetric scaling of the direct and indirect gaps due to the correction to the self-interaction error in PBE functional. Furthermore, the change in surface dipoles as a result of the applied strain and rippling, which could also alter the relative alignment of CBM band and vacuum level [126].

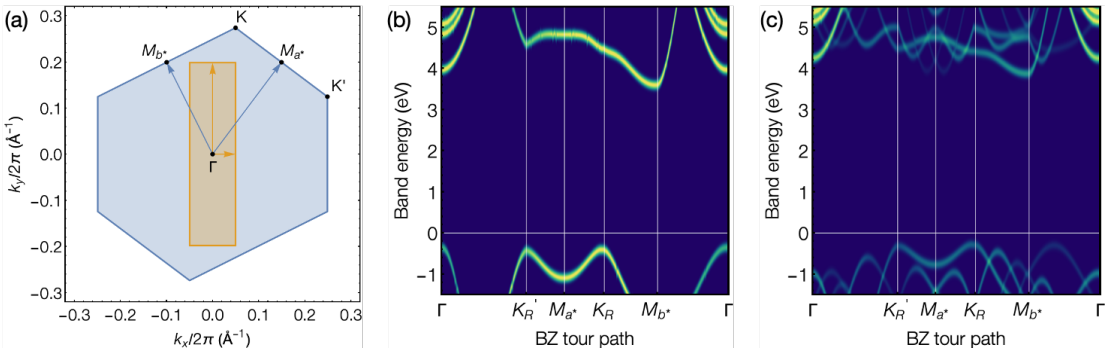

Figure 4.9, Band structures plots for hBN. The blue region in plot (a) shows the BZ of a unit cell of the hBN that has been strained and rotated to make it compatible with our compute cell of the diamond substrate. The gold region shows the BZ for the compute cell of the 5x1 supercell. Plot (b) shows the unfolded effective band structure for a 5x1 supercell of strained-planar hBN computed using vaspkit [127], and plot (c) shows that effective band structure for the same system when the sheet is free to form a ripple.

To understand the effect of rippling on surface-layer interactions in the 2D/H-diamond (100) heterostructures, we analyzed the charge transfer between the H-diamond (100) surface and the constituent 2D layer. The interface charge was evaluated by computing the charge density difference using the equation,

$$\Delta\rho = \rho_{(S/D)} - \rho_D - \rho_S \tag{4.3}$$

where $\rho_{(S/D)}$, ρ_D, and ρ_S represent the electron density of the heterostructure, H-diamond (100) surface, and hBN (graphene) layer, respectively. The $\Delta\rho$ for the planar (top-panel) and wavy (bottom-panel) graphene/H-diamond (100) and hBN/H-diamond (100) heterostructures are illustrated in Figures 4.10 (a) and (d), respectively. The areas enclosed by red surfaces are the charge accumulation regions, while the blue regions represent areas with charge depletion. A higher degree of charge transfer is observed for the rippled systems, due to sp^2 to sp^3 rehybridization of orbitals, which leads to the appearance of additional free orbitals ready to participate in surface reactions, resulting in stronger vdW interactions between the rippled layers and the H-diamond (100) surface as reported earlier in the Atomic Structure section. As a result, in the rippled heterostructures, the charge transfer across the interface looks inhomogeneous, with more charge accumulation around the valley, indicating a stronger vdW interaction due to rippling. As compared to the graphene/H-diamond (100) interface, a higher degree of charge transfer at the valley of hBN is observed, which can be attributed to the larger degree of rippling in the hBN layer.

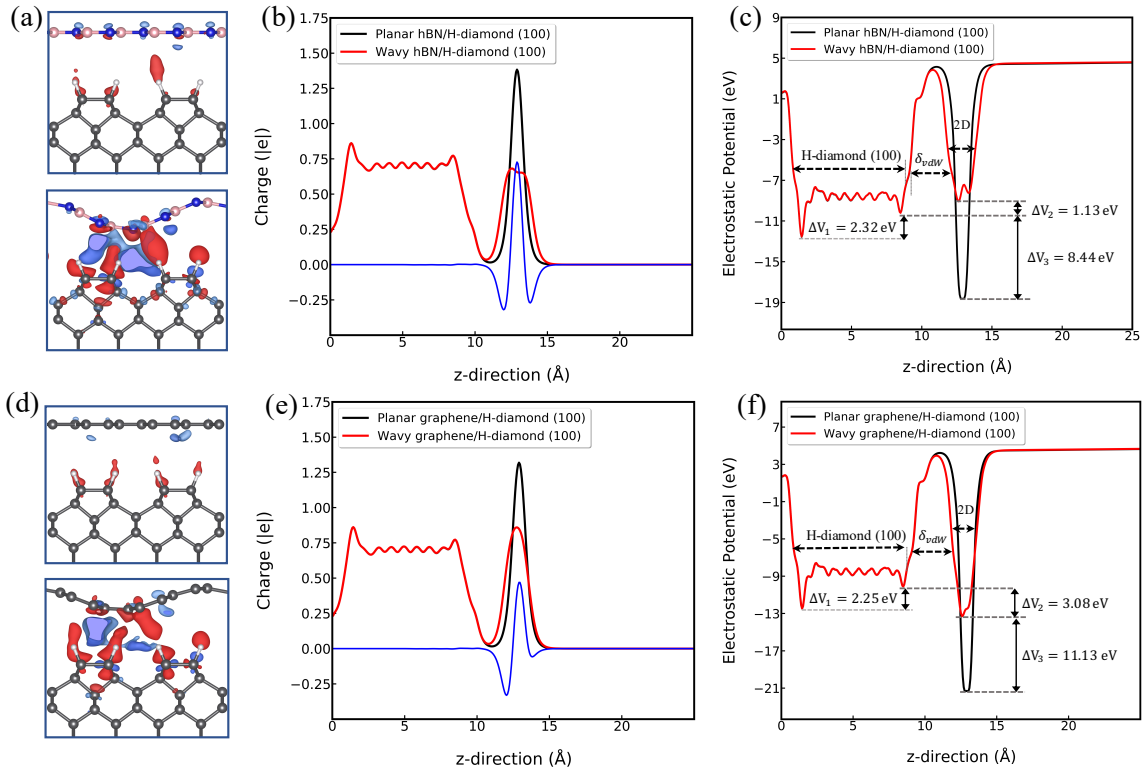

Figure 4.10, visual and qualitative analysis of charge transfer in the heterostructures are presented. Plots (a, d) show electron density difference maps for bringing the 2D layer into contact with the H-terminated diamond. Plots (b, e) show the averaged charge density vs depth into the heterostructure, and (c, f) show the corresponding effective potential profile through the heterostructure for the planar vs. wavy configurations of the hBN/H-diamond (100) and graphene/H-diamond (100) heterostructures. The blue line in plots (a, e) are the difference between the black and red lines. In the electron density difference maps (a, d), blue and red regions represent charge loss and gain in the space with respect to isolated 2D layer and H-diamond (100), respectively. The top and bottom panels illustrate systems with a planar and rippled constituent 2D layer, respectively. An isosurface value of 0.001 was used for this purpose.

Since the 2D layer rippling influences the interlayer electronic interactions, controlled by vdW forces, we extract the planar charge profiles across the 2D/H-diamond (100) interface by integrating charges along the normal direction [113], [128], [129], as shown in Figure 4.10 (b) and (e). As illustrated, for both the heterostructures, the overall feature of the out-of-plane (*z*-direction) charge profiles are similar. However, variations in the charge profile along the *z*-direction are observed in the proximity of the 2D layer. Quantitatively, the percentage charge differences of 51% and 35% around the vicinity of the rippled and strained-planar layers for the hBN and graphene layers, respectively, confirms a stronger

interaction between the rippled 2D layers and H-diamond (100) surface. In addition, a noticeably larger charge difference above the layer is observed for the rippled hBN layer as compared with graphene. Although a noticeable difference in charge transfer is observed between the heterostructures containing planar and rippled layers, our quantitative charge transfer evaluation using the Bader analysis [73] shows that the amount of charge transferred to the substituent layers in all the heterostructures are negligible, and the charge carriers are mainly preserved across the vdW region. Therefore, for all the rippled 2D/H-diamond (100) heterostructures, rippling does not significantly affect charge extraction by the 2D layer. The rippling, if engineered precisely, could have a much larger effect on the transport properties of systems with smaller vdW spacing, particularly where a covalent bond is formed between the layer and the diamond substrate, as suggested in an earlier work [85].

In H-diamond (100), surface dipoles are generated around the C-H bonds due to the electronegativity difference between the C and H atoms. These surface dipoles are also responsible for the modification of the system's work-function (ψ), which is defined as $\psi = V_{vac} - E_f$, as illustrated in Figure 4.10 (c) and (f). Since we are mainly focused on the relative shift in the ψ due to rippling, we utilize PBE functional to extract potential profiles and the Fermi levels for all the simulated systems. The work function of the H-diamond (100) computed using the PBE functional is 4.21 eV. For the planar and wavy hBN/H-diamond (100) heterostructures, the ψ values were evaluated as 3.93 eV and 4.07 eV, respectively. The ψ of planar and wavy graphene/H-diamond (100) were found to be slightly higher with values of 3.98 eV and 4.13 eV, respectively. These results indicate that integrating the 2D layers and the H-diamond (100) surface reduces the ψ of the H-diamond

(100) surface, regardless of the type and atomic composition of the 2D layer, mainly due to the suppression of the surface dipoles. This reduction of ψ due to the adsorption of 2D layers on the H-diamond (100) surface is consistent with the adsorption of organic molecule on Si (100) surface [130], and on diamond (100) surface [131]. In addition, for both types of 2D layers, the heterostructures comprising of a rippled layer have lower ψ. Quantitatively, a 3.6% and 3.8% reduction in the ψ of the hBN/H-diamond (100) and graphene/H-diamond (100) is observed when the constituent layer is rippled. This is mainly due to the rippled induced inhomogeneity in the dipoles along the *xy* plane leading to a reduction in the vacuum level. The change in work function, $\Delta\psi$, according to the Helmholtz equation, is defined as $\Delta\psi = \Delta\sigma.(A.\epsilon_0)^{-1}$, here $\Delta\sigma$, A, and ϵ_0 represent change in surface dipole moment, surface area, and vacuum permittivity. In the case of the simulated heterostructures, the bulk of the contributions to the $\Delta\psi$ (by corollary to the potential drop (ΔV)) should come from $\Delta\sigma$, a parameter which includes all the changes in surface dipoles, vdW interaction and charge transfer between these systems. Therefore, as illustrated in Figure 4.10 (c) and (f), a larger ΔV is observed for the rippled systems as compared with the planar ones, resulting from the inhomogeneity of dipoles, higher degree of charge transfer and stronger vdW interactions in the rippled heterostructures. Further analysis of the potential profiles reveals some of the device related features, such as potential drop and depletion width at the interface, are larger/wider in the hBN/H-diamond (100) than the graphene/H-diamond (100) system. This is mainly attributed to the relatively larger amount of charge transfer aided by the larger degree of rippling in hBN, which further confirms

the roles, albeit small, played by the structural features such as strain and rippling in modifying device related properties in 2D/3D heterostructures.

To obtain a better understanding of the effect of rippling on the electronic properties of the heterostructures, we analyzed and compared the site-resolved local density of states (LDOS) of the wavy and planar hBN(graphene)/H-diamond (100) systems, as illustrated in Figure 4.11 The hBN/H-diamond (100) heterostructures with strained-planar and wavy constituent layers, shown in Figure 4.11 (a) and (c), exhibit semiconducting characteristics with wide energy gaps. The PBE computed bandgap values for H-diamond (100), strained-planar, and wavy hBN/H-diamond (100) systems are 2.62 eV, 2.54 eV and 2.41 eV, respectively. Quantitatively, the energy gap of strained-planar and rippled hBN/H-diamond (100) is smaller than the gap of H-diamond (100) by 3.1% and 8%, respectively. A larger reduction is observed in the energy gap of the rippled hBN/H-diamond (100) heterostructure as compared with the planar system. This could be due to the stronger vdW interactions and the larger charge transfer, in the rippled structure as compared with the planar system, causing a more significant change in the electronic structure of the heterostructure. In both planar and wavy heterostructures, the H-diamond (100) states mostly contribute to the valence band edge (VBE) while the hBN states mainly contribute to the conduction band edge (CBE). The VBE in the wavy hBN is lower than that of the strained-planar layer by 0.3 eV. This 23% reduction in the VBE energy of the constituent layer as a result of rippling is an indication of a stronger interaction between the wavy layer and the H-diamond (100) surface, confirmed by the larger vdW energy and charge transfer in this system. Both heterostructures show a Type-II band alignment where CB edge of the hBN is below (above)

the CB (VB) edge of the H-diamond (100) surface, which is consistent with the band alignment feature extracted by the XPS method in a recent experimental study [132].

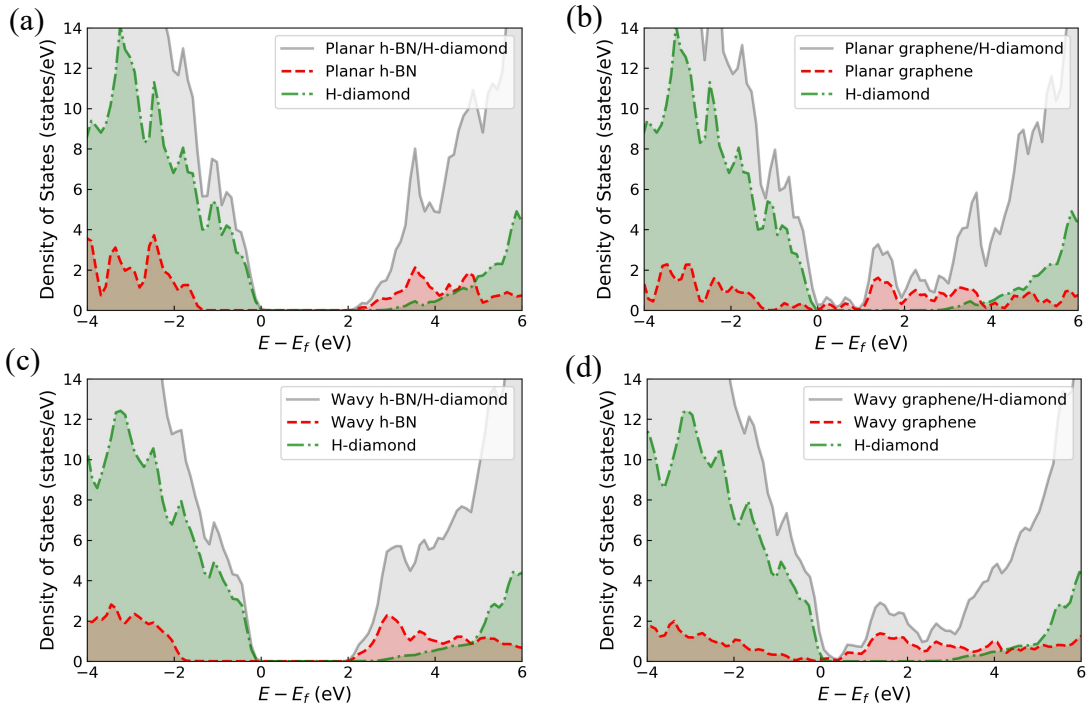

Figure 4.11, Total density of states (TDOS) and site-projected local density of states (LDOS) of H-diamond and 2D layer are shown. (a) Planar hBN/H-diamond (100), (b) Planar graphene/H-diamond (100), (c) Wavy hBN/H-diamond (100), and (d) Wavy graphene/H-diamond (100) TDOS and LDOS plots.

Though the conduction band offsets (CBOs) are similar in both the heterostructures, the valence band offsets (VBOs) between the hBN and H-diamond (100) in the wavy heterostructure is relatively larger than the planner heterostructure. The VBO increase of 26% in the wavy hBN/diamond (100), as compared to the planar counterpart, indicates a higher hole confinement at the heterojunctions. The band alignment of the wavy heterostructure predicted using the PBE functional is consistent with our previous study using HSE functional [125]. LDOS of strained-planar and wavy graphene/H-diamond (100) systems are illustrated in Figs. 7 (b) and (d). The LDOS plots of graphene/H-diamond (100) indicate

that regardless of the type of the graphene layer, the system remains metallic due to the preserved Dirac cone characteristic.

4.5 Effect of Surface Termination on Electrochemical Properties of Diamond (100) and hBN/diamond (100)

In SD method, the diamond surface is usually terminated with an element to passivate the dangling bonds, increase structural stability, and induce surface conductivity to facilitate charge transfer properties [133]. The most commonly used element for passivation of diamond surface is hydrogen. Hydrogenation is known to by uplift the valence band maximum (VBM) of diamond surface. Hydrogen terminated (H-) diamond (100) surface has a negative electron affinity, which results in a unique p-type conductivity at the diamond's surface and enables charge transfer from the upper valence band edge (VBE) of diamond to the lowest unoccupied molecular orbital (LUMO) of the adlayer [38], [65].

In addition to hydrogen termination, previous studies have utilized oxygen (O),[65], [134], [135] Boron (B),[136] hydroxyl (OH),[65], [135] NH_2,[137] and organic molecules,[131] to passivate diamond surface and modify its structural and electronic properties. Studies show that unlike hydrogen, oxygen terminated (O-) diamond shows positive electron affinities (EA) and large ionization potential (IP),[134], [138], and hence, does not induce surface conductivity [135]. O-diamond surface has been studied as a promising host for nitrogen-vacancy quantum sensors [139]. A previous first-principles study indicates that Boron terminated (B-) diamond (100) surface can have negative electron affinity depending on the boron coverage and arrangement [140]. Heavily B doped diamond was found to show metallic or superconducting characteristics in some previous studies [141].

A previous computational study reported a positive electron affinity for nitrogen terminated (N-) diamond (100) surface with three different surface arrangements. This study shows that N-diamond (100) is a promising surface for application in nano-sensing technology and quantum information processing [133].

Various surface terminations can be used to modulate the structure and electronic properties at the surface of diamond. Although previous studies have shed light on possible diamond (100) terminations, they are mainly narrowed down to investigate one or two terminating species. Our previous studies show that a hexagonal boron nitride (hBN) layer interfaced with H-diamond (100) can act as a Type-II semiconductor, where the hBN layer acts as a cap layer to preserve the p-type conductivity at the surface of H-diamond. The surface termination of diamond can hugely impact the interface and transport properties in diamond-based heterostructures. To the authors' knowledge, thus far, no study has investigated the effect of terminating species and arrangement on structural and electronic properties of diamond (100) based heterostructure. Here, we provide a comprehensive analysis of the effect of surface termination on structural and electronic properties of diamond (100) and hBN/diamond (100) systems. The terminating species investigated in this study include Hydrogen (H), oxygen (O), boron (B), and nitrogen (N).

4.5.1 Structural Modeling of Terminated diamond (100)

In this study, we used the 2×1 reconstructed diamond (100) surface terminated with H, O, B, and N atoms on the top surface. In all structures, the carbon bonds at the bottom of diamond surface were passivated with hydrogen. This method is conventionally used to avoid artificial charge interactions between the periodic diamond images along the z-

direction. It also helps to maintain the sp^3 orbital hybridization and bulk-like characteristic of diamond [135].

Hydrogenated diamond (100) surface was generated by placing hydrogen on top of carbon atoms in diamond surface. Addition of hydrogen changes the surface dimers from double to single bonds [65]. To generate oxygen-terminated facets, we can either position O on top of surface carbon atoms, known as ketone (T), or in a bridge position connecting the diagonal carbon atoms, i.e., ether (B) configuration. For boron and nitrogen, we analyzed two possible configurations of surface passivation, one by placing the terminating species on top of surface carbon atoms, and the other by replacing the first carbon row of diamond with the terminating species (S). The latter is selected based on high-symmetry adsorption sites on diamond (100) surface and agrees with previous computational studies [133], [136]. The diamond (100) surfaces with various terminations were relaxed to obtain the optimized atomic structures.

4.5.2 Structural and Electronic Properties of Terminated diamond (100)

In this section, we report an analysis of the structural and electronic properties of the surface terminated diamond (100). The relaxed atomic structures of the clean and passivated diamond (100) surfaces are depicted in Figure 4.12. To validate the structures, we evaluated the carbon dimer bond length at the diamond (100) surface to be 1.38 Å, which is consistent with previous DFT studies [65], [142], [143]. The double bond at the surface of clean diamond (100) gives rise to the appearance of π and π^* states in the energy gap [65]. As a result of hydrogen termination, the relaxed carbon dimer length is increased to 1.63 Å, which is consistent with previous computational,[65], [142], [144], and

experimental works [145]. For the oxygen terminated surfaces, the ketone (T) structure contains double C=O bonds, while the ether configuration has single C–O–C bonds at the surface of diamond. Passivation with boron on top of carbon atoms increases the relaxed carbon dimer length to 1.62 Å. The diagonal distance between the plane of oxygen atoms and the first carbon layer in the ether structure is 0.83 Å, a reduction of 0.22 Å compared to bare diamond. The C=O bond length in the ketone setup is 1.20 Å. These values are consistent with an earlier DFT calculation [65]. In B-diamond, each boron atom is bonded to another boron and one carbon atoms, forming a B=B and a B – C bond with bond distance of 1.53 Å and 1.56 Å, respectively. Whereas, in B-diamond (100) (S), each boron forms a single B – C bond with two carbon atoms at the diamond surface and a B –B bond with another boron atom, similar to C atoms arrangement at the surface of bare diamond (100). In addition, in this structure, each carbon atom is bonded to four other atoms at the surface, forming sp^3 hybridization. N-diamond has a similar structure to B-diamond, but each nitrogen forms a single bond with another nitrogen and a double bond with a carbon atom at the surface of diamond. N-diamond (100) (S) relaxed conformation is similar to B-diamond (100), with some variations in bond lengths as illustrated in Figure 4.12.

To compare the effect of terminating element on the stability of the diamond (100) surface, we evaluated the total energies per number of passivating species at diamond's top surface after geometric optimization. For O-diamond (100), the ether configuration was found to be more stable than the ketone setup, with an energy difference 0.36 eV/O atom. Previous studies also reported a higher stability for the ether configuration with a slight difference in the evaluated energies due to variations in computational setups and models [65], [135].

Although the ether setup is more stable, the lined-up C=O bonds at the surface of the ketone configuration could be interesting for charge transfer at the interface of diamond and the proximal layer. For boron terminated surfaces, the energy of B-diamond (100) (S) was found to be lower than B-diamond (100) (T) by 0.54 eV/B atom. Similarly, for the N-diamond (100), the (S) passivation type was also found to be stable than the N-diamond (100) (T) system.

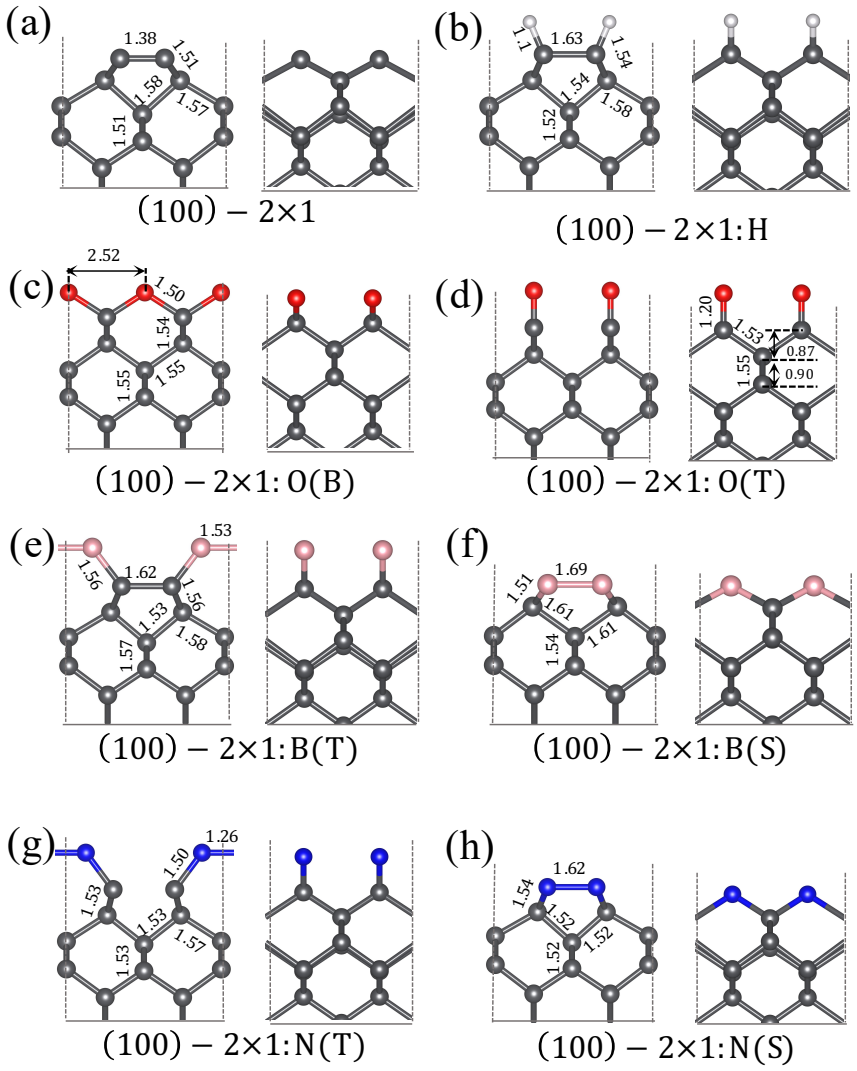

Figure 4.12, Relaxed atomic structure of (a) clean (100) diamond surface, (b) H–diamond (100) surface, (c) and (d) The O-diamond (100) surfaces with ether (C – O – C) and ketone (C=O) configurations, respectively. (e) and (f) The B–diamond (100) surfaces with boron on top and replacing the first carbon layer (S), respectively. (g) and (h) The N–diamond (100) surfaces with nitrogen placed on top and substituting the first carbon layer, respectively.

In addition, we compared the energetic stability of diamond (100) surface terminated with different elements. For this purpose, we selected the most stable termination type from each terminating species group (H – diamond, O – diamond (B), B-diamond (S), and N-diamond (S)). The results show that $E_N < E_O < E_B < E_H$, with $E_N, E_O, E_B,$ and E_H representing total energy per number of terminating species for N, O, B, and H,

respectively. Accordingly, termination of diamond (100) surface with N and H results in the most and least energetically stable structures, respectively.

To understand the effect of terminating species and surface bonds on the electronic properties of diamond (100) surface, we analyzed the density of states (DOS) plots, as illustrated in Figure 4.13. The PBE predicted gap of clean diamond (100) surface is 1.32 eV, slightly lower than the previously reported value of 1.46 eV [78]. Hydrogenation results in converting C=C to C–C at the surface of diamond (100), causing the energy gap to increase by 1.98 eV. Hydrogen passivation was found to uplift the diamond's energy bands by 2.5 eV in earlier theoretical works with passivation on one side of diamond [65]. In this work, the bottom surfaces of both clean and functionalized diamond surfaces are passivated with hydrogen, and as a result, hydrogenation of the top surface only uplifts the CBM and VBM of diamond remains almost intact. The ether O-diamond (100) exhibits a semiconducting structure with an energy gap of 1.84 eV, whereas the ketone structure shows a semi-metallic characteristic arising from the surface C=O bonds. The B-diamond (100) has a small gap of 0.22 eV, while the B-diamond (100) (S) structure shows a slightly larger bandgap of 0.35 eV. The N-diamond (100) surface shows metallic characteristic, whereas the N-diamond (100) (S) configuration is a wide bandgap semiconductor with a bandgap of 2.0 eV.

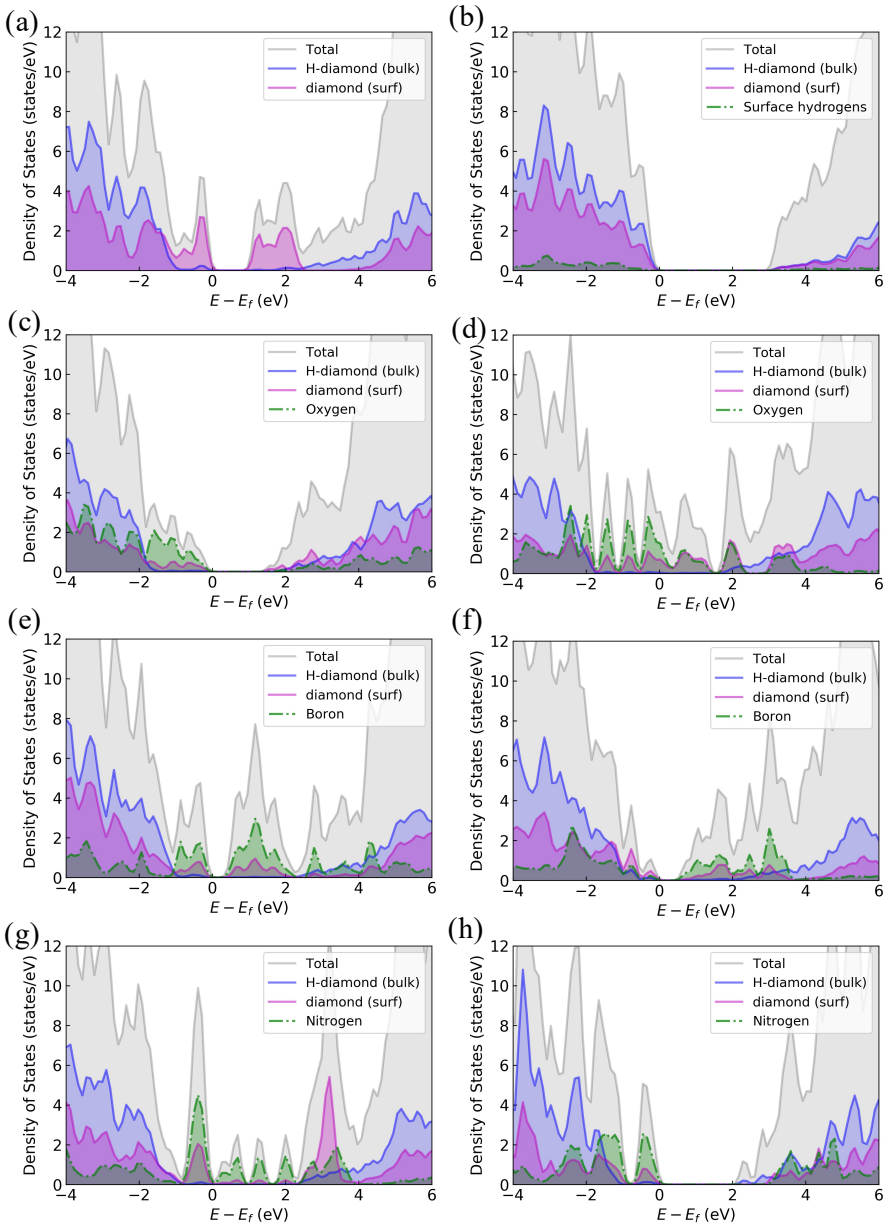

Figure 4.13, Partial density of states (DOS) plots of (a) clean (100) diamond surface, (b) H–diamond (100) surface, (c) and (d) The O-diamond (100) surfaces with ether (C – O – C) and ketone (C=O) configurations, respectively. (e) and (f) The B–diamond (100) surfaces with boron on top and replacing the first carbon layer (S), respectively. (g) and (h) The N–diamond (100) surfaces with nitrogen placed on top and substituting the first carbon layer, respectively

4.5.3 Structural and Electronic Properties of hBN/diamond (100) heterostructures

In order to garner comprehensive understanding of the roles of the surface terminations on the hBN/diamond heterostructures, relaxed diamond (100) surfaces with various

terminations were then interfaced with the relaxed hBN layer following the procedure described in section 4.2. Figure 4.14 (a – h) depicts the relaxed hBN/diamond heterostructures with various termination species and types. For the other heterostructures with vdW interfacial interactions, we evaluated the min vdW spacing (δ_{min}) at the valley of the corrugations. The computed δ_{min} values are 2.57 Å, 2.09 Å, 2.65 Å, 2.59 Å, 2.30 Å, and 2.50 Å for H, O (B), O (T), N, and N (S) passivation, respectively. The degree of rippling was defined as the vertical distance between the ridge and valley of the rippled layer. Accordingly, the degree of the ripple is 1.73 Å, 1.70 Å, 1.71 Å, 1.64 Å, 1.73 Å, and 1.72 Å for structures with H, O (B), O (T), N, and N (S) surface termination, respectively. The surface termination type affects both δ_{min} and degree of rippling, which could be attributed to different reactivity at these surfaces. As illustrated in Figure 4.14 (e) and (f), the B atoms at the surface of B-diamond (100), regardless of the configuration type, form physical bonds with the hBN layer, transitioning from a vdW bonding to the ionic bonding characteristics. In B-diamond (100), the boron dimer at the surface of diamond converts from double to single bond when B-diamond is interfaced with hBN. In this structure, a B atom from each pair bonds with an atom in the hBN layer. In B-diamond (100) (S), only one of the boron pairs in the supercell bonds with the hBN layer.

Furthermore, to understand the effect of diamond (100) surface termination on adhesion strength and the bonding between the layer and the substrate, we computed the adhesion energies (E_{Ad}) and binding energies ($E_{binding}$) using equation 4.1.

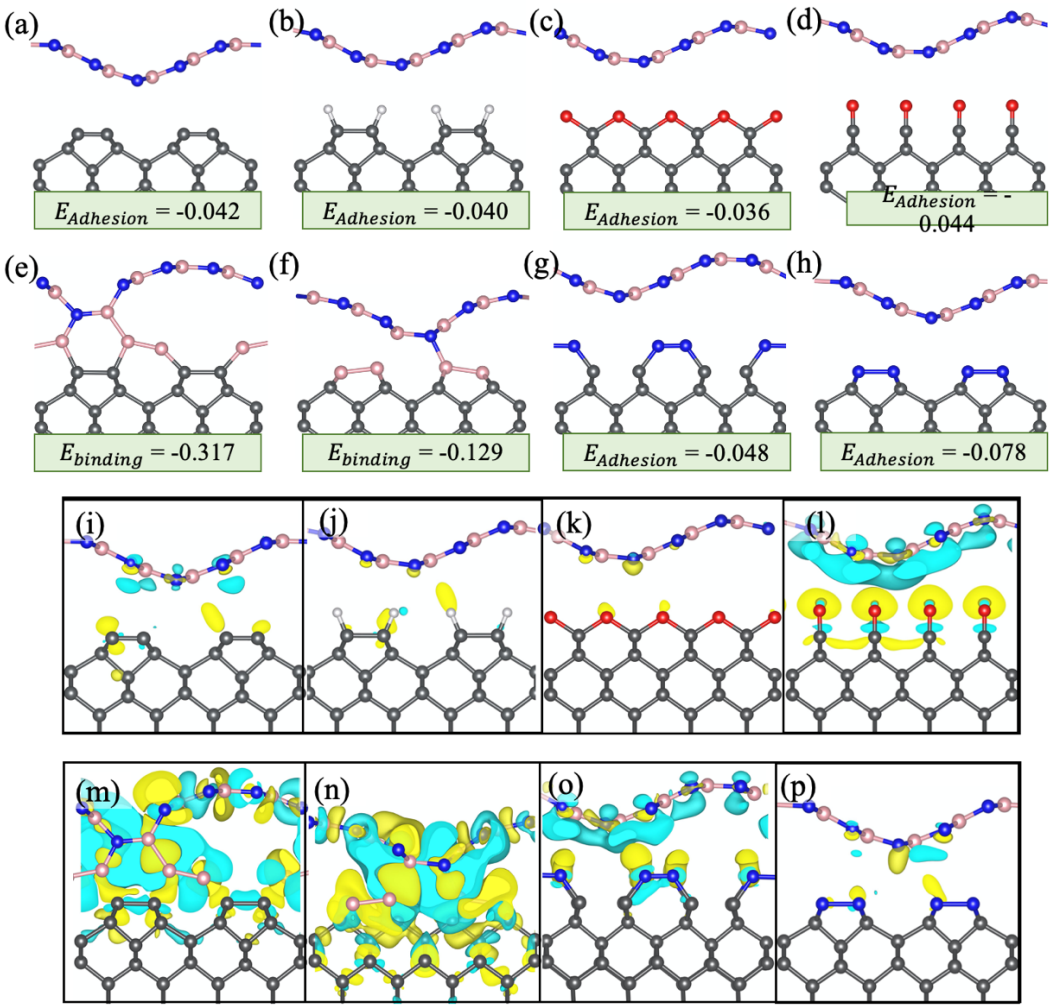

Figure 4.14, Top two rows show the relaxed atomic structure of hBN layer interfaced with diamond (100) with various passivation types, including (a) clean, (b) H-, (c) O- with ether configuration, (d) ketone type O-, (e) B- where B atoms are placed on top of surface carbon layer, (f) B- with B atoms replacing diamond's first carbon layer, (g) N- with N atoms on top, and (h) N- with N atoms substituting diamond's first carbon row. (i – j) last row shows charge density difference plots for hBN/diamond (100) heterostructures where diamond (100) is clean, hydrogenated, ether and ketone type oxygen passivated, Boron terminated with B atoms on top and replacing diamond's first carbon layer, Nitrogenated with N atoms on top and substituting diamond's first carbon row, respectively. The blue areas indicate regions with charge loss, and the yellow regions represent the areas with charge gain. A similar isosurface value was used for all plots to obtain an accurate comparison.

For B terminated systems, we report the binding energies, as the hBN layer is chemisorbed to the diamond surface in these structures. Adhesion energy values are evaluated to compare vdW interactions where the layer is physiosorbed. As expected, the binding is stronger in B-diamond compared with B-diamond (S) due to breaking of the B=B bonds and

formation of more bonds per cell. The lowest and highest adhesion energy values belong to the ether type hBN/O-diamond (100) and the (S) configuration of hBN/N-diamond (100), indicating the weakest and the strongest vdW interactions between the layer and the diamond surface in the two mentioned systems, respectively. For the heterostructures with O-diamond (100), ketone shows stronger adhesion compared to ether due to the presence of C=O bonds. In addition, the heterostructure with the (S) type N-diamond surface (Figure 4.14 (g) and (h)) shows a stronger vdW interaction despite the larger δ_{min} in this structure. This could be related to the presence of double N=N bonds at this surface. Except for the cases with B termination, diamond surface C-C bonds are intact even after the adsorption of the hBN layer. Except for the cases with B termination, diamond surface C-C bonds are intact even after the adsorption of the hBN layer.

In addition to the structural properties, the choice of surface termination is also expected to modify the surface electronic properties of the diamond surface. Consequently, the surface terminations also influence the interactions and charge transfer between the hBN layer and the diamond surface. To understand the interactions across the interface, we evaluated the interfacial charge between the hBN layer and the diamond surface by calculating the charge density difference ($\Delta\rho$) using equation 4.3. The resulting charge density difference maps for the studied heterostructures are depicted in Figure 4.14 (i – p). The yellow regions represent the areas with charge accumulation, and the blue areas indicate regions with charge depletion as a results of the interfacial interactions between the hBN layer and diamond surface. The relatively large amount of charge transfer across the interface in boron terminated structures is mainly due to the chemical bonds between

the hBN layer and diamond surface (Figure 4.14 (e) and (f)). The O-terminated heterostructures exhibit a varying degree of charge transfer even with the common surface termination. The ether O-terminated heterostructure exhibit a nominal amount of charge transfer as compared to the bare surface. Whereas, in the hBN/O-diamond (100) of type ketone, charge accumulation and depletion are observed on surface oxygen and the hBN layer, respectively. This could be attributed to the presence of C=O dangling bonds at the diamond surface, which are well-known to result in a positive electron affinity (EA) [134]. The larger charge accumulation across the interface of hBN/O-diamond (100) of ketone compared with ether is also consistent with the larger adhesion strength for this system. Regardless, the charge depletion and accumulation regions in ketone are separated, and we did not observe a charge flow in between the hBN layer and the diamond surface. For the heterostructures with boron terminated diamond surface, a larger degree of charge accumulation is observed across the interface of the heterostructures with N atoms on top of diamond as compared to the ones with N atoms substituting the first carbon row. This could be resulted from the smaller vdW spacing in the former, which also seems to yield a flow of charge across the interface.

To gain a better understanding of how surface termination impacts the interfacial interactions and states hybridization in the hBN/diamond (100) system, we analyzed the site projected density of states (PDOS), as illustrated in Figure 4.15. Here, the first three carbon layers of diamond were considered as surface and the rest for bulk contribution. We also evaluated the contribution from surface terminating atoms and the hBN layer. The heterostructures composing of diamond with B on top, and replacing the first carbon row

of diamond, and N on top show a metallic characteristic, as illustrated in Figure 4.14 (d – g). This could relate to the rearrangement of orbitals at the surface. Whereas, the hBN/diamond systems with clean diamond surface, H-diamond (100), O-diamond (100) of type ether, and N-diamond (100) with (S) configuration show semiconducting characteristic with a finite gap. In comparison to heterostructures with clean diamond surface, hydrogenation increases the bandgap of system by 84%, while surface passivation with O (B) and N (S) reduces the gap by 30% and 21%, respectively.

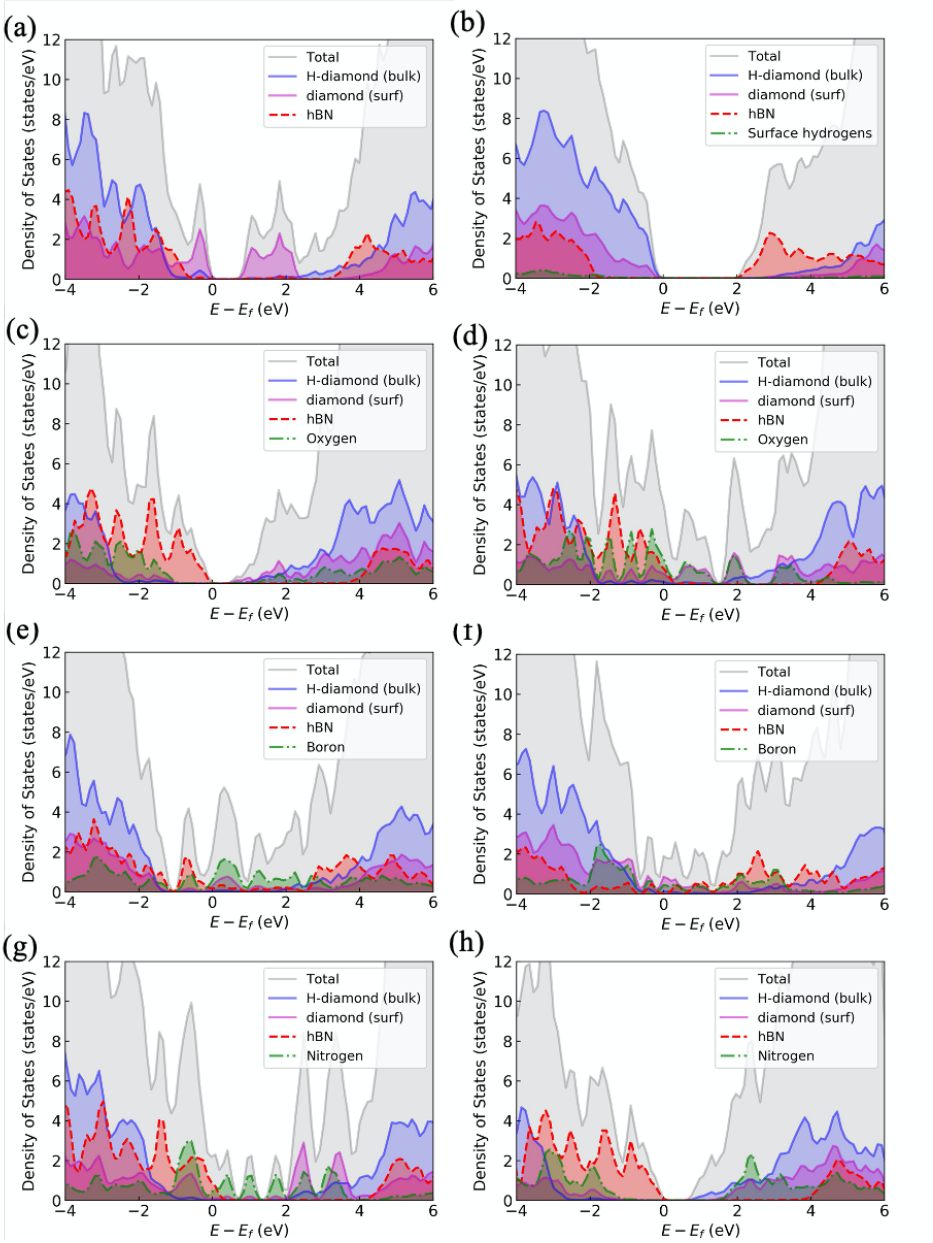

Figure 4.15, Partial Density of states (PDOS) plots for total, bulk and surface diamond, surface terminating atoms, and the hBN layer in hBN/diamond (100) heterostructures with (a) clean (100) diamond surface, (b) H–diamond (100) surface, (c and d) The O-diamond (100) surfaces with ether (C – O – C) and ketone (C=O) configurations, respectively. (e and f) The B–diamond (100) surfaces with boron on top and replacing the first carbon layer (S), respectively. (g and h) The N–diamond (100) surfaces with nitrogen placed on top and substituting the first carbon layer, respectively.

Similar to the charge transfer process, the choice of surface termination element and type is expected to affect the electronic properties of the heterostructure. In order to elucidate

this impact, we evaluated the bandgap (E_g), work function (ψ), electron affinity (EA), and ionization potential (IP) of the semiconducting following the method discussed in section 4.. The predicted parameters are tabulated in Table 4.4. Hydrogenation was found to reduce the *IP* of the system by 14%. On the other hand, oxygenation (B) and nitrogen passivation (S) increase *IP* of the clean system by 10% and 9%, respectively. Similarly, hBN/H-diamond (100) has a smaller ψ, while heterostructures with ether, and (S) type N-terminated surfaces have higher work function compared with hBN/diamond(100). A similar trend is observed in the *EA* values, i.e., hydrogenation reduces the *EA* by 52% while oxygenation and nitrogenating of the diamond surface were found to increase the *EA* by 18% and 15%, respectively.

Table 4.4, Calculated values of $E_f - E_{vbm}$, $E_{cbm} - E_f$, bandgap (E_g), work function (ψ), ionization potential (*IP*), electron affinity (*EA*)

System	$E_f - E_{vbm}$	$E_{cbm} - E_f$	E_g	ψ	IP	EA
hBN/diamond	0.238	0.897	1.31	4.82	5.06	3.92
hBN/H-diamond	0.2891	2.1243	2.41	4.036	4.327	1.913
hBN/O-diamond (B)	0.2944	0.6196	0.914	5.2568	5.551	4.637
hBN/N-diamond (S)	0.2529	0.7865	1.0395	5.281	5.534	4.494

4.6 Conclusions

In this chapter, we presented three projects to provide a comprehensive analysis of structural and electronic properties of diamond (100) surface and 2D/diamond (100) heterostructures.

I the first section, we presented systematic DFT calculations and analysis of the structural and electronic properties of 2D/H-diamond (100) heterostructures. Both the hBN and graphene layers are physiosorbed on the H-diamond (100) surface through vdW-like interactions and exhibit a structural corrugation around the reconstructed diamond surface. The corrugation is an artifact of the in-plane strain between the 2D layers and the H-diamond (100) surface and was found to have little or no effect on the electronic properties. Though the charge transfer from the H-diamond (100) to either of the 2D layers is minimal, the charge transfer occurs through the valley of rippling, and the majority of transferred charges are confined within the vdW gaps between the 2D layers and the H-diamond (100) surface. The graphene/H-diamond (100) system retains the linear band dispersion characteristic of the graphene layer and exhibits semi-metallic properties. Conversely, the hBN/H-diamond (100) heterostructure maintains the wide bandgap characteristics of each constituent system with an energy gap of 3.35 eV. Band alignment analysis reveals a TYPE-II band alignment between the hBN layer and the H-diamond (100) surface with the CBO and VBO of 0.10 eV and 1.38 eV, respectively. A significant finding of this work is that a thin layer of hBN not only offers a defect-free interface with the H-diamond (100) surface, but also provides a layer-dependent tunability of electronic properties and band alignment with the acceptor layer in the SD-based diamond devices.

In the second part, we presented *ab initio* studies to compare the structural stability and electronic properties of rippled (wavy) and planar hBN (graphene) layer and hBN(graphene)/H-diamond (100) heterostructures. We carefully selected and analyzed the structural alignments between the 2D layers and H-diamond (100) surface using chemical

intuition and cluster analysis. We found that rippling affects the structural and electronic properties of 2D layers and 2D/diamond heterostructures regardless of the 2D layer type. The rippled hBN layer shows a larger electron affinity and bandgap compared with the planar counterpart, with an indirect gap type in both structures. In graphene, remarkably, rippling does not open a band gap but does cause the Dirac cone to *shift* away from the corner of the BZ. Rippling of the strained layers is an exothermic process, i.e., energetically favorable. Also, the heterostructures with a rippled layer were identified as the low-energy structures. Therefore, the strained layers are expected to develop ripples through the growth process, both as an isolated layer and as an interfacial layer on the H-diamond (100) surface. Thus, the planar heterostructures can only be achieved under applying additional constraints to the 2D layer, such as external forces (or clamping) to keep the layer flat. A larger vdW interaction and charge accumulation was observed at the interface between the rippled layers and H-diamond (100) surface. Both wavy and planar hBN/H-diamond (100) heterostructures indicate a Type-II band alignment, but a relatively larger VBO results in stronger hole confinement in the rippled system. Although rippling had a minimal effect on the electronic properties, its impact can be magnified depending on the 2D layer quality, vdW spacing and magnitude of rippling. Hence, understanding the impact of ripples, though small, is essential in determining the overall performance of the fabricated device design.

Lastly, we reported a computational analysis of the effect of diamond surface termination on structural and electronic properties of hBN/diamond (100) heterostructures. We selected oxygen (O-), boron (B-), and nitrogen (N-) termination for this study. Among diamond

(100) surfaces passivated with various species, N-termination was found to yield the highest stability. In hBN/diamond (100) heterostructures with B- termination, the hBN layer forms chemical bonds with the B atoms at the diamond surface. Other diamond surfaces form a van der Waals (vdW) heterostructures with hBN, among which structures with N-terminated diamond show the strongest vdW interfacial interaction. hydrogenation was found to increase the bandgap of the heterostructure, while surface passivation with O and N reduce the gap. Add electron charge transfer.

5. Structure and Properties of Amorphous Oxide Acceptors

5.1 Overview

Transition metal oxides (TMOs) with high work function and high electron affinity such as vanadium pentoxide (V_2O_5) can act as an electron acceptor layer when interfaced with hydrogen terminated (H-) diamond surface to facilitate surface transfer doping [16], [17]. Thin metal oxide films offer higher thermal stability and easier processing, and therefore are more desirable acceptors than the molecular counterparts for surface transfer doping of diamond [146]. Previous experimental studies have utilized V_2O_5 to achieve surface transfer doping of H-diamond with high thermal stability. These studies have reported a carrier density of $1.8 \times 10^{13} - 1.1 \times 10^{14}$ at the interface of V_2O_5 and H-diamond [17], [147], [148]. A previous DFT study investigated using crystalline V_2O_5 as an acceptor layer for surface doping of H-diamond (100) surface [146]. On the other hand, experimentally grown oxides usually contain amorphous phases, which can introduce additional states acting as electron traps, locally increasing the oxide electric field, for the electron transferred from the diamond surface. Computational modeling of amorphous solids is a challenging task. Due to the lack of long-range order in amorphous solids, there exist several possible structures, and as most of these structures are away from equilibrium, evaluating them is hard. In addition, experimentally grown amorphous solids usually contain a combination of various structures, and hence it is important to consider the many possible conformations in modeling. A few computational studies have investigated modeling and analysis of bulk amorphous indium oxide (In_2O_3) [149], aluminum oxide (Al_2O_3) [150], and V_2O_5 [151]. However, to the author's knowledge, a computational model and analysis that provides a

deep understanding of amorphous V_2O_5 (a-V_2O_5) films (slabs) is still lacking. Computational simulations and calculations for amorphous slabs pose additional difficulties compared to bulk structures. The common method of slab generation used for crystalline materials, i.e., cutting the slab out of bulk structure, is not feasible for amorphous systems due to the lack of a clear crystalline plane as a reference to cut the slab. Moreover, cutting slabs out of bulk may result in a charge imbalanced surface and therefore a need for surface passivation, such as Ref. [152].

In this project, we first present a systematic modeling and analysis of the structural properties of a-V_2O_5 slabs using melt-quench molecular dynamics (MD) simulations and analyze their electronic properties using density functional theory. Furthermore, we integrate the a-V_2O_5 slabs with the H-diamond (100) surface and evaluate the heterogeneity induced charge transfer across the interface using density functional theory calculations. The presented approach in this study can be used to generate and analyze other amorphous TMO slabs and heterostructures. Therefore, our study based on the experimentally observed structural models provides a fundamental insight into the transfer doping process in the TMO/diamond-based devices.

5.2 Computational Details

The a-V_2O_5 bulk and slabs were generated through melt-quench MD simulations as implemented in the Large-scale Atomic/Molecular Massively Parallel Simulator (LAMMPS) package [153]. The interatomic potentials were defined using a combination of the Born-Mayer-Huggins, also known as Tosi/Fumi, potential [154], [155], Morse potential [156], and the coul/cut style for computing the standard Coulombic interactions. The selected

cutoff for the Coulombic interactions was 10.0 Å. The Born-Mayer-Huggins is defined using the equation:

$$E = Aexp\left(\frac{\sigma - r}{\rho}\right) - \frac{C}{r^6} + \frac{D}{r^8} \quad r < r_c$$

Where, σ and ρ are interaction-dependent and ionic-pair-dependent length parameters, respectively. here, r_c is the cutoff value for the interaction distance. The selected values for the Born-Mayer-Huggins parameters are reported in Table 5.1.

The Morse potential is described as:

$$E = D_o[e^{-2\alpha(r-r_0)} - 2e^{-\alpha(r-r_0)}] \quad r < r_c$$

Where, α is inversely proportional to the width of the potential. The parameters used for Morse potential are listed in Table 5.2.

Table 5.2, Born-Mayer-Huggins Potential Parameters

Interaction	***A*** **[kcal/mol]**	$\boldsymbol{\rho}$ **[Å]**	$\boldsymbol{\sigma}$ **[Å]**	***C*** **[kcal/mol Å^6]**	***D*** **[kcal/mol Å^8]**	$\boldsymbol{r_c}$ **[Å]**
V - V	0.22	0.22	2.0	0.0	0.0	10.0
V - O	0.195	0.195	2.415	0.0	0.0	10.0
O - O	0.17	0.17	2.83	0.0	0.0	10.0

The ionic relaxation of crystalline structures and the electronic structure evaluation for all samples were performed through density functional theory calculations as implemented in the Vienna Ab initio Simulation Package (VASP) using the Perdew-Burke-Ernzerhof (PBE) exchange correlation functionals [54]–[59]. We used the DFT+U method [157], with U= 3.25, which describes the coulomb interactions using a Hubbard model, to treat the strongly correlated 3d electrons of V and provide accurate prediction of the electronic

properties. An energy cutoff value of 520 eV was used, and the structures were optimized to minimize the forces on ions to equal or better than 0.007 eV. For the statistical analysis and pre-screening of the amorphous samples, we restricted the k-point sampling to the Gamma point. For the detailed analysis of structural and electronic properties, we used a 2×6×5 Gamma-centered grid to sample the Brillouin zone of the unit cell of V_2O_5. The grid of k-points to sample the Brillouin zone of the supercells and slabs were selected accordingly. All the presented slabs are periodic, and a vacuum space of 30 Å was added in the normal direction to avoid the interactions between periodic images.

Table 5.3, Morse Potential Parameters

Interaction	D_o **[kcal/mol]**	α **[Å^{-1}]**	r_o **[Å]**	r_c **[Å]**
V - V	0.0	5.0	1.75	10.0
V - O	4.5	2.0	1.84	10.0
O - O	0.0	5.0	3.0	10.0

5.3 Structural and Electronic Properties of Crystalline V_2O_5

We first present a systematic analysis of the structural and electronic properties for crystalline V_2O_5 (c-V_2O_5) bulk and (001) surface. This provides a useful reference for comparing the amorphous samples against it. Figure 5.1 shows the relaxed structures of the unit cell, common coordination found in c-V_2O_5, and the polyhedral network of the (001) slabs generated through cutting the bulk sample in z direction. The lattice parameters of the bulk c-V_2O_5 were computed as a = 11.55 Å and b = 3.62 Å, and 4.79 Å, which are in agreement with reported values by previous computational and experimental studies with minor differences [146], [158]. The building block of V_2O_5 is VO_5 equivalent to the first shell of

vanadium (figure 5.1, (a) and (b)). The second and third shells of vanadium correspond to edge-sharing and corner-sharing polyhedral, respectively.

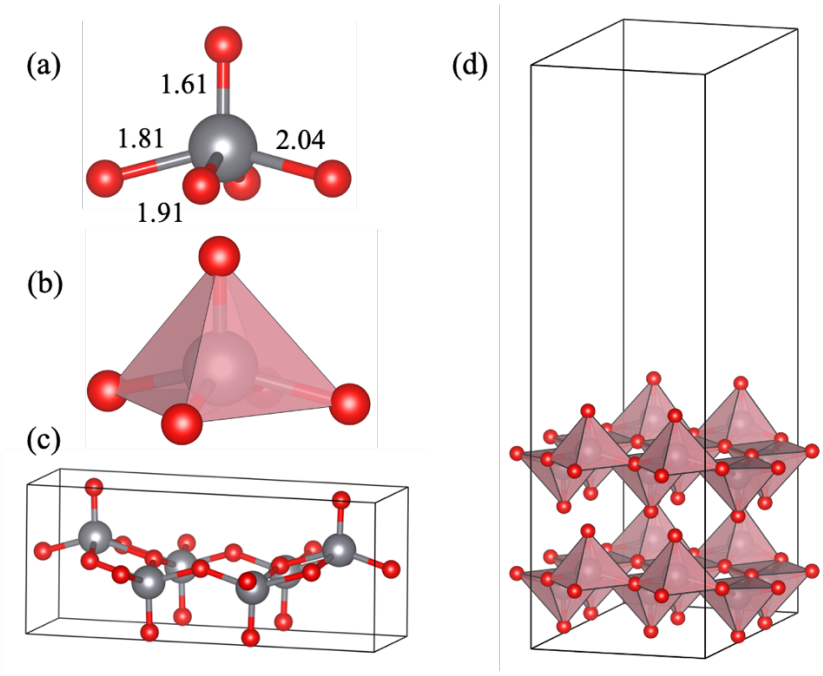

Figure 5.1, Three-dimensional illustration of relaxed crystal structure for *c*-V_2O_5 (a) building block ball-stick view, (b) building block polyhedron view, (c) unit cell ball-stick view, and (d) (001) slab polyhedral network.

To evaluate the short-range and long-range orders in the structure, we computed the radial distribution functions g(r) for *c*-V_2O_5, illustrated in figure 5.2. The radial distribution function g(r) shows the atoms environment and distribution, and it provides an important tool for validating simulations of amorphous systems presented later in this chapter. It also provides a great tool for comparison of theoretical and experimental data.

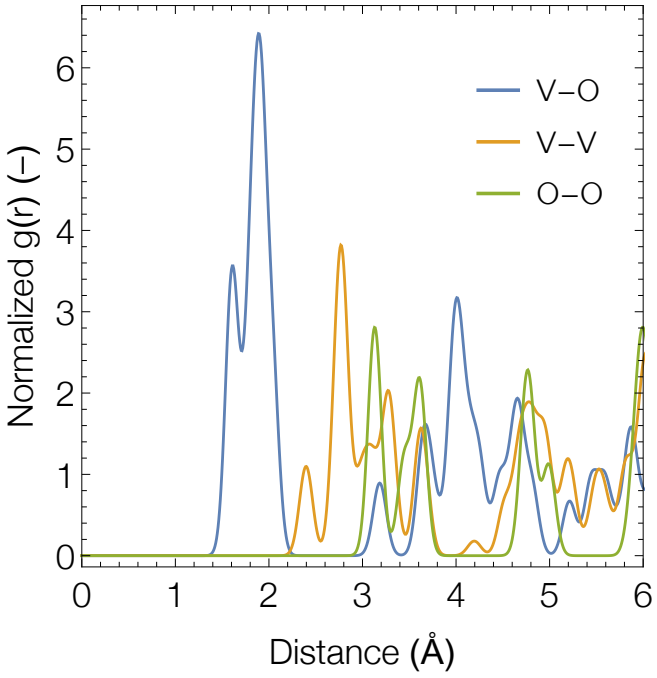

Figure 5.2, Pair distribution function g(r) for *c*-V_2O_5

Furthermore, to evaluate the electronic properties of the *c*-V_2O_5 unit cell and (001) slab, we calculated the local (atom-projected) density of states as depicted in figure 5.3. The electronic properties of *c*-V_2O_5 unitcell and slab are tabulated in table 5.3. As shown in figure 5.3, the states from oxygen are mainly contributing to the valence band valence band edge (VBE) states. Whereas the states from vanadium mainly contribute to the conductional band edge (CBE) states.

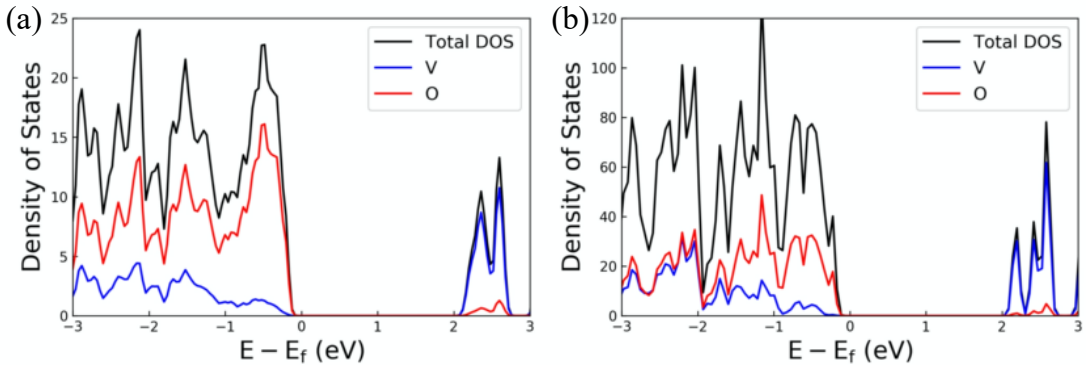

Figure 5.3, Atom-projected density of states (PDOS) of *c*-V2O5 (a) unitcell and (b) (001) slab

The calculated bandgap of *c*-V_2O_5 unit cell using U = 3.25 eV is 2.32 eV, which is in great agreement with the reported experimental value of 2.3-3.1 eV [159] with a difference below 1%. The alignment of bandgap and structural parameters with past studies validates the accuracy of our calculations. Analyzing the crystal structures is an important step to create a reference for the study of amorphous bulk and slab samples, especially due to the lack of sufficient studies in this area and the large number of possible structures for amorphous systems.

Table 5.4, Electronic properties of *c*-V_2O_5 unitcell and (001) slab

System	$E_f - E_{vbm}$	$E_{cbm} - E_f$	E_g (*PBE + U*)	E_g (*Exp. Ref.*)
V_2O_5 unit cell	0.221	2.136	2.357	2.3-3.1[159]
V_2O_5 (001) surface	0.260	2.138	2.398	-

5.4 Structural and Electronic Properties of Bulk Amorphous V_2O_5

Prior to modeling the slabs, we used melt-quench MD simulations to generate bulk amorphous V_2O_5 (*a*-V_2O_5) samples. In this section, we present the method, results, and analysis for simulation of bulk *a*-V_2O_5, statistical analysis, and evaluation of structural and

electronic properties of bulk models. This step is critical for providing an in-depth understanding and evaluation of amorphous slabs.

5.4.1 Modeling Bulk a-V_2O_5

A schematic of the melt-quench amorphous structure generation is presented in Figure 5.4. The amorphous bulk structures were generated through the following procedure. To allow the atoms rearrangement during melting, we expanded the simulation box by 0.5 Å in every direction. We heated up the crystal structure composing of 56 atoms up to 2500 K using NVT simulations at 10 $K.ps^{-1}$ to achieve the molten structure. To ensure that the crystal is fully melted, we selected a temperature above V_2O_5 melting point (2023.15 K). Then, we cooled down the molten structure to 300 K at three different cooling rates, 1 $K.ps^{-1}$, 10 $K.ps^{-1}$, and 100 $K.ps^{-1}$ using an NPT ensemble. The structures were further relaxed using *ab initio* quantum simulations as implemented in VASP.

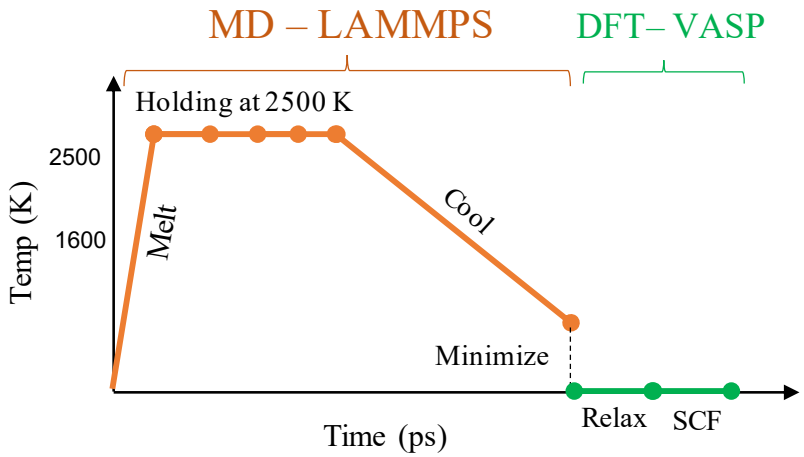

Figure 5.4, Schematic representation of the procedure of generating *a*-V_2O_5 bulk and (001) slabs: For bulk sample generation there is a single step for holding. However, for generating slabs, the holding procedure contained multiple steps: relaxing to a substrate, squishing the box along the in-plane directions, holding while making the substrate less sticky to allow rearrangement of atoms.

5.4.2 Statistical Analysis of Bulk a-V_2O_5

Thanks to the lack of long-range order in an amorphous system, a wide range of possible structures can be obtained. Evaluating a single amorphous model without pre-screening the large palette of possible structures may result in biased and unrealistic results. Therefore, we performed a comprehensive statistical analysis of various amorphous structures to provide a reliable prediction of structural and electronic properties. To generate the models for statistical analysis, during the holding stage at 2500 K, we took snapshots of the molten structure every 50 ps, and cooled down each structure at various cooling rates. This procedure resulted in a total of 117 simulated structures.

To evaluate the structural properties and stability of the a-V_2O_5 bulk samples, we computed the total energy and volume of the generated structures. Figure 5.5 illustrates plots of total energy, volume, and the correlation between them for the 117 a-V_2O_5 bulk samples. The structures cooled down at the slowest rate (1 $K.ps^{-1}$) show lower volume and higher energy compared with the ones cooled at 10 $K.ps^{-1}$, and 100 $K.ps^{-1}$. Traditionally, one would expect a lower cooling rate to result in a higher chance of crystallization and hence higher energetic stability. However, here the lower stability of the structures cooled at slowest cooling rate can be associated with their lower volume, giving atoms less free space to arrange themselves to form a low energy conformation. In addition, the lower volumes of slowest quenched structures can also be attributed to the fact that these structures were kept under pressure for the longest time.

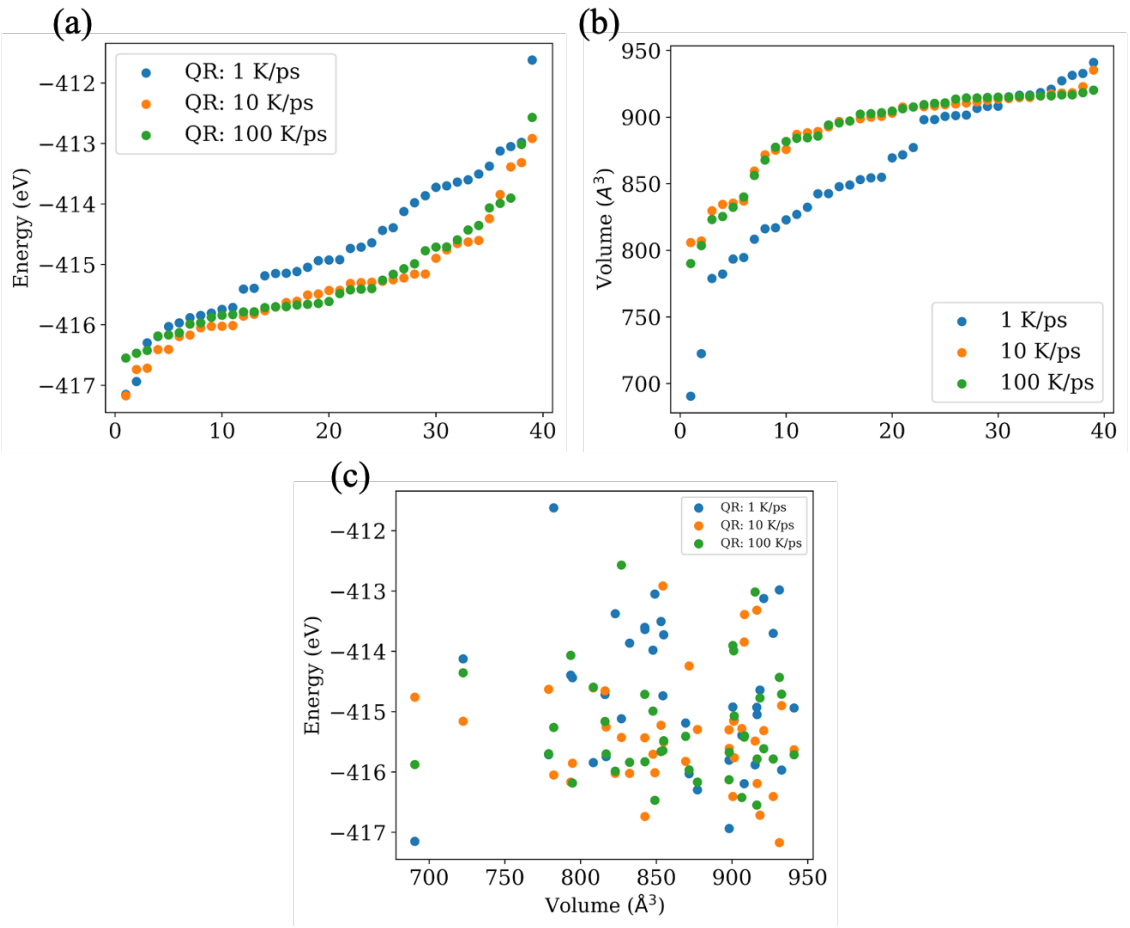

Figure 5.5, Statistical analysis of *a*-V_2O_5 bulk: (a) total energy plotted in ascending order (b) volume plotted in ascending order, (c) total energy vs. volume.

Next, we performed a quick evaluation of the electronic properties of the generated samples. Figure 5.6 illustrates the total energy plotted as a function of the band gap. For all simulated structures, the magnitude of the gap is smaller than the crystalline counterpart (2.3 eV), which could indicate the presence of electron/hole traps in the system. Further evaluation is needed to confirm the presence of traps. In addition, ten structures were found to have near-zero band gaps and semi-metallic characteristics.

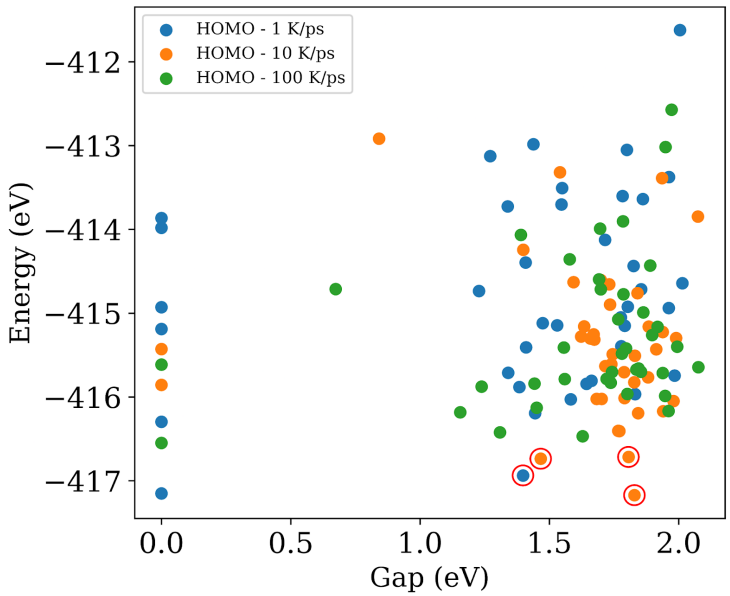

Figure 5.6, Statistical analysis of *a*-V2O5 bulk: total energy vs. energy gap.

5.4.3 Structural and Electronic Properties of Selected Bulk a-V_2O_5

To gain deeper understanding of the structural and electronic properties of the *a*-V_2O_5 bulk samples, we selected and evaluated one structure for each cooling rate with low energy and large bandgap, as annotated in figure 5.5. For easier reference, hereon, we use the quench rate (QR) and the snapshot ID (#) to refer to the selected structures. The relaxed structures of the selected bulk samples are illustrated in Figure 5.7 (a – d). As seen in Figure 5.7 (a – d), the generated structures no longer show the observed order in *c*-V_2O_5 (figure 5.1). To further evaluate the structures, we generated the pair distribution function $g(r)$ for each pair of elements in the bulk *a*-V_2O_5 samples. In all the examined structures, the first double-peak observed in *c*-V_2O_5, corresponding to the first V-O coordination shell, is no longer observed in the amorphous structures. Single V-O, V-V, and O-O peaks are nearly retained below 4 Å, with slight variations in O-O first peak intensity among the studied samples.

This observation indicates the presence of short-range order in the bulk *a*-V_2O_5 samples, albeit less strong than *c*-V_2O_5. On the other hand, the peaks above 4 Å are broadened and less intense compared with *c*-V_2O_5, indicating the significantly lower long-range order in the bulk *a*-V_2O_5 samples.

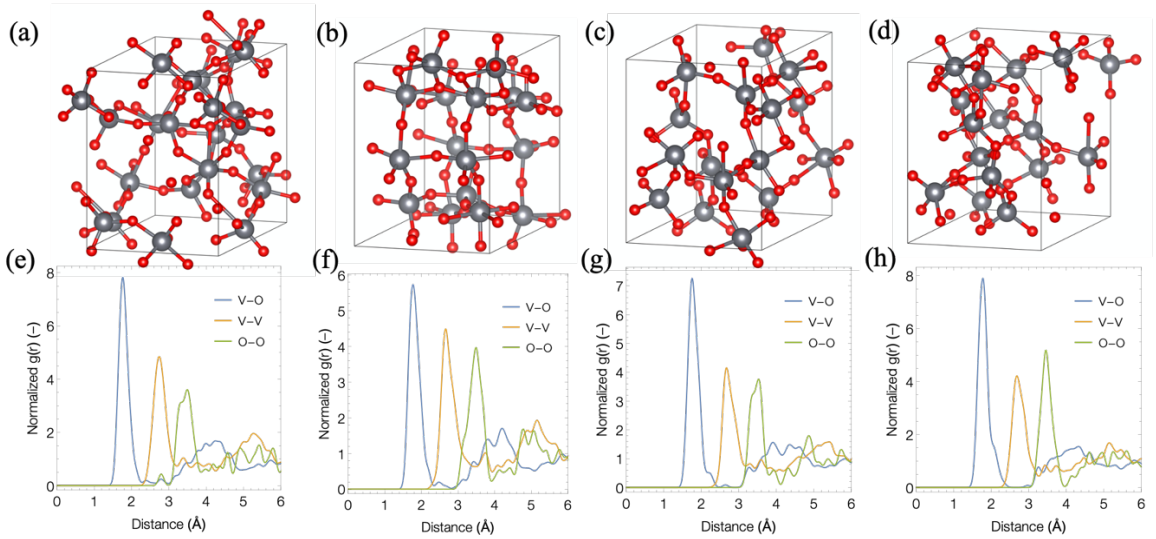

Figure 5.7, Structural analysis of selected bulk *a*-V_2O_5 samples: (a – d) relaxed structures, and (e – h) radial distribution function g(r).

Furthermore, we evaluated the atom-projected density of states plots for the bulk *a*-V_2O_5 samples, as illustrated in Figure 5.8. The calculated electronic properties of the bulk *a*-V_2O_5 samples are presented in table 5.3.

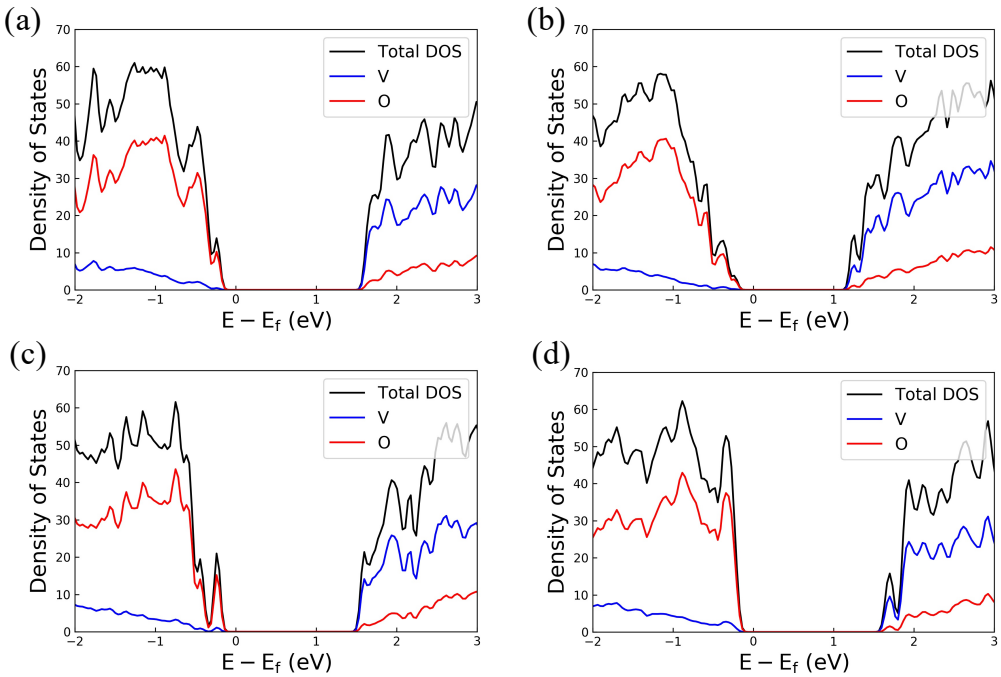

Figure 5.8, atom-projected density of states for bulk a-V_2O_5 samples for (a) QR1 - #31, (b) QR10 - #10, (c) QR10 - #29, and (d) QR10 - #40.

Comparing to the c-V_2O_5 (figure 5.3), we did not observe a noticeable change in the value of $E_f - E_v$, but the conduction band minimum (CBM) has shifted towards the fermi level by ~ 0.5-1.0 eV. In addition, a significant increase in the CBE states is observed. These observations are indicatives of potential n-type doping in the bulk a-V_2O_5 samples.

Table 5.5, Electronic properties of selected bulk a-V_2O_5 samples

System	$E_f - E_v$	$E_c - E_f$	E_g
QR1 - #31	0.240	1.607	1.847
QR10 - #10	0.250	1.221	1.471
QR10 - #29	0.240	1.561	1.800
QR10 - #40	0.226	1.641	1.868

5.5 Structural and Electronic Properties of Amorphous V_2O_5 (001) Slabs

Unlike crystalline surfaces, amorphous slabs cannot be simply generated by cutting the slab out of bulk. This is mainly because in amorphous systems, there is no clear atomic plane to cut the slab from. Moreover, in these systems, cutting slabs from bulk may result in unbalanced dipole moments and charge distribution at the surface. Here, we present a novel approach for modeling amorphous slabs, which includes a set of steps to allow the atoms to rearrange themselves into a slab form during the melt-quench procedure. We implement this method to generate *a*-V_2O_5 (001) slabs as potential acceptor layers used for surface doping of H-diamond (100). Similar to the bulk analysis, we will first present a statistical analysis of the multiple slab models, followed by an in-depth evaluation of the structural and electronic properties for some selected structures.

5.5.1 Modeling a-V_2O_5 Slabs

The procedure to generate the *a*-V_2O_5 slabs follows the schematic representation in Figure 5.4, where the holding stage is accomplished in multiple steps. During the holding procedure, we first relaxed the atoms to an imaginary substrate placed in the normal direction of the slabs. Then, we squished the box using a sticky substrate in the other two directions. In the next stage, we held the structure at 2500 *K* while making the substrate less sticky by lowering the potential so that the atoms can freely rearrange into a low energy conformation. Finally, we cooled down the structure to 300 *K* and minimized it. We further relaxed the atomic structures and computed their electronic properties through DFT calculations.

5.5.2 Statistical Analysis of a-V_2O_5 Slabs

To perform a statistical analysis and pre-screening of amorphous slabs, we generated multiple structures by holding the molten structure at 2500 K and taking snapshots every 60 ns. We then cooled down each molten structure separately following the approach discussed in the previous section to obtain the a-V_2O_5 slabs. This process resulted in generating 84 amorphous structures. Figure 5.9 shows the weighted averaged radial distribution function $g(r)$ for the generated a-V_2O_5 (001) slabs. Similar to the bulk amorphous models, here we observe the retention of short-range order and diminishing of the long-range order compared to the g(r) of c-V_2O_5.

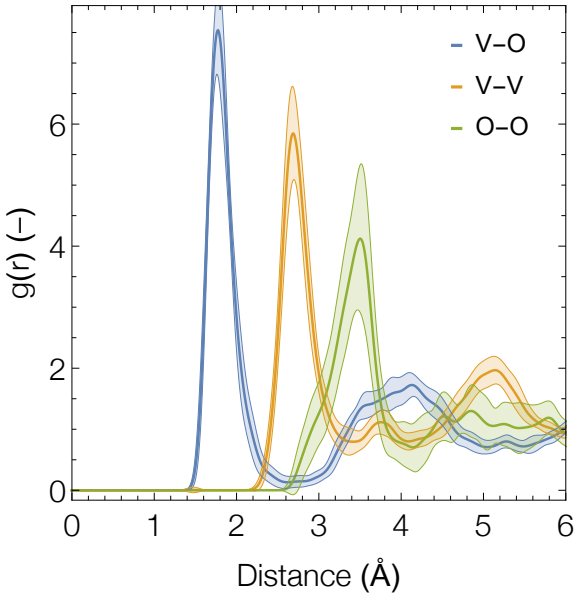

Figure 5.9, Statistical analysis of *a-V_2O_5* slabs: Pair distribution functions g(r)

Through the presented method, we were able to generate multiple a-V_2O_5 slabs with different properties. In searching for a pattern to understand these structures at a deeper level, we analyzed the correlation between properties of interest (Figure 5.10). The results show

some correlation between electronic property values. Rather strong correlation was observed between HOMO and E_f , as well as band gap and LUMO $- E_f$. On the other hand, we did not observe a clear correlation between energetic stability of the slabs and their electronic behavior. This motivated us to further analyze selected properties of interest.

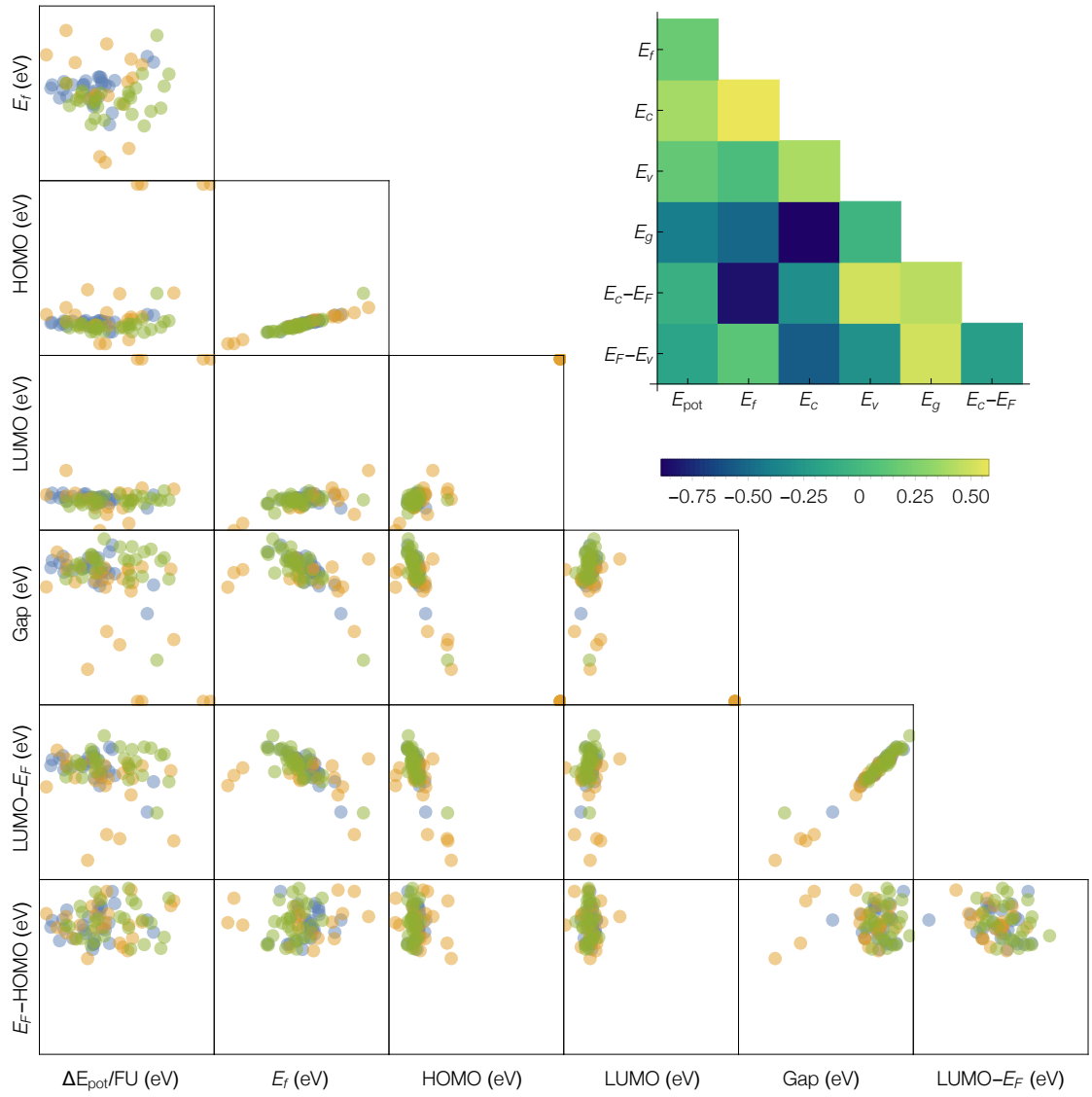

Figure 5.10, Statistical analysis of a-V_2O_5 slabs: correlation grid and Pearson correlation of properties.

We further evaluated the coordination number and average charge on V and O, and their correlation with the distance from the surface of the *a*-V_2O_5 slabs. The results are depicted in

Figure ***5.11***. The difference between the coordination number at the surface and bulk of slabs is small, which indicates that the surface is charge-balanced and does not require passivation. We also observe that the V and O atoms at the surface are associated with lower positive and negative charge, respectively, with much larger deviation in O charge compared to V. In addition, atoms with smaller nearest neighbor distance are associated with larger charge deviation.

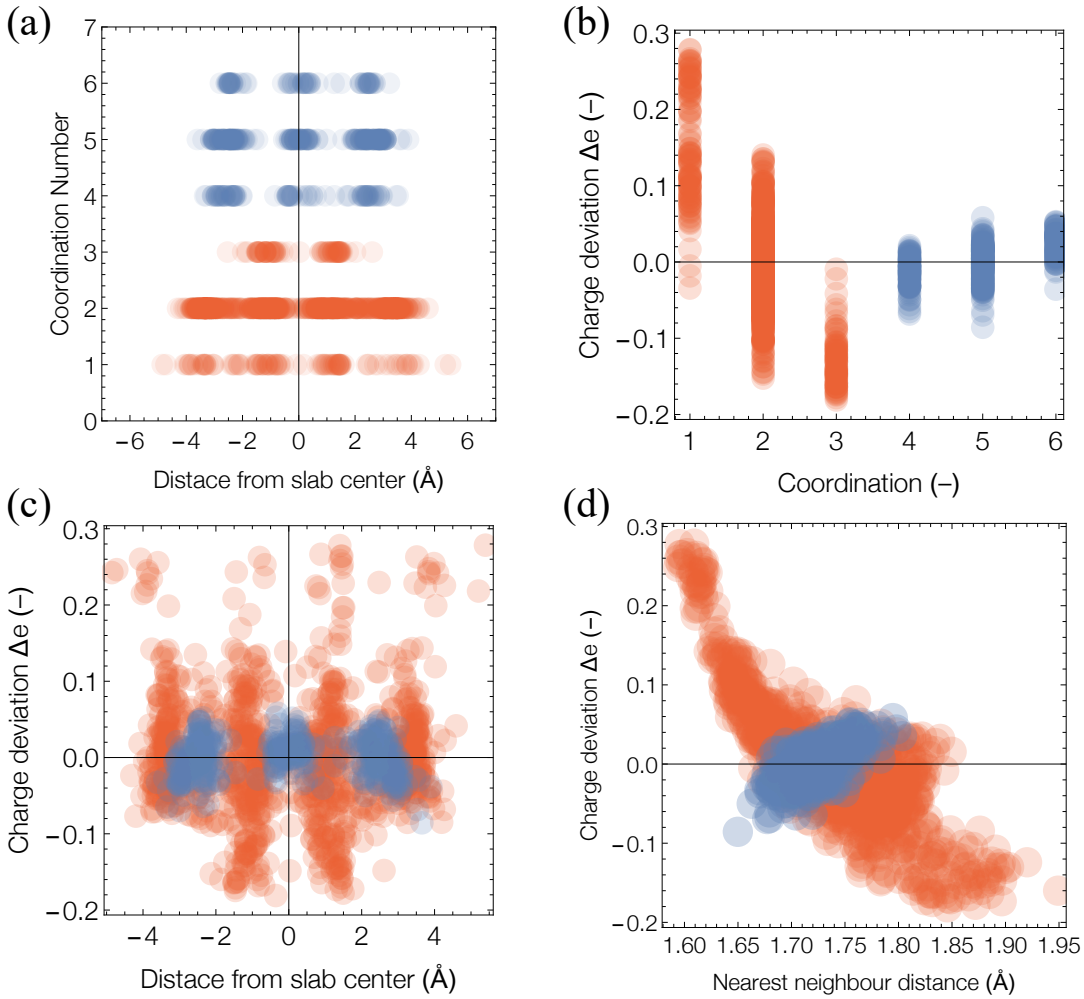

Figure 5.11, Statistical analysis of *a*-V2O5 slabs:(a) coordination number vs. distance from the center of the slab, (b) charge deviation (Δe) vs. coordination number, (c) Δe vs. distance from the center of the slab, and (d) Δe vs. nearest neighbor distance. Blue and red circles represent values for V and O, respectively.

To understand the structures at a deeper level, we took a closer look at relations between E_f − HOMO, LUMO − E_f, bandgap, thickness, and energy per formula unit, as illustrated in Figure 5.11. We noticed that all the generated slabs have a lower LUMO − E_f value as compared with the crystalline slab with comparable thickness and number of atoms, which could indicate the presence of electron traps and *n*-type conductivity for the amorphous slabs and is beneficial for surface doping of H-diamond.

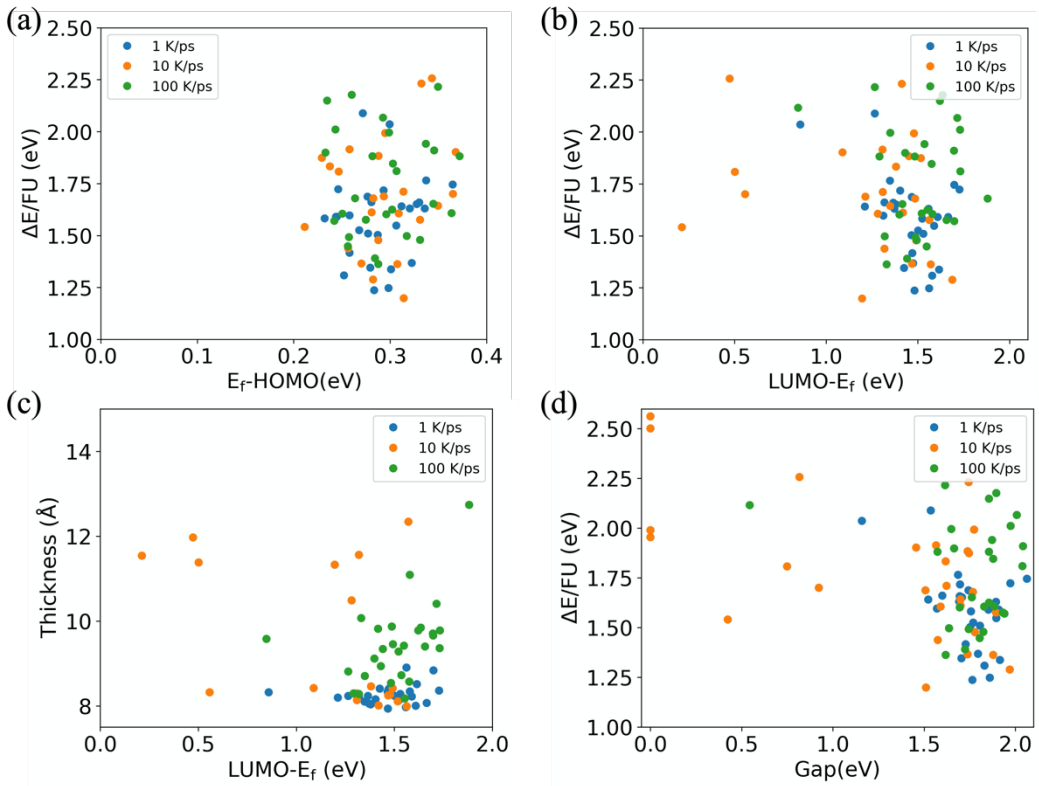

Figure 5.12, Statistical analysis of amorphous a-V_2O_5 (001) slabs: (a) and (b), total energy plotted as a function of $E_f - HOMO$ and $LUMO - E_f$, respectively. (c) Thickness plotted as a function of $LUMO - E_f$, and (d) total energy vs. bandgap.

Furthermore, we evaluated the average weighted energies of interest for these structures at three different temperatures (Figure 5.13). The weighting factor was defined as $\beta = \frac{1}{K_B T}$, where K_B is the Boltzmann constant and T is the temperature. The results indicate that at higher temperatures, some high energy structures become more likely. From this, we selected a few minimum energy structures with larger weight, and performed detailed structural and electronic property analysis.

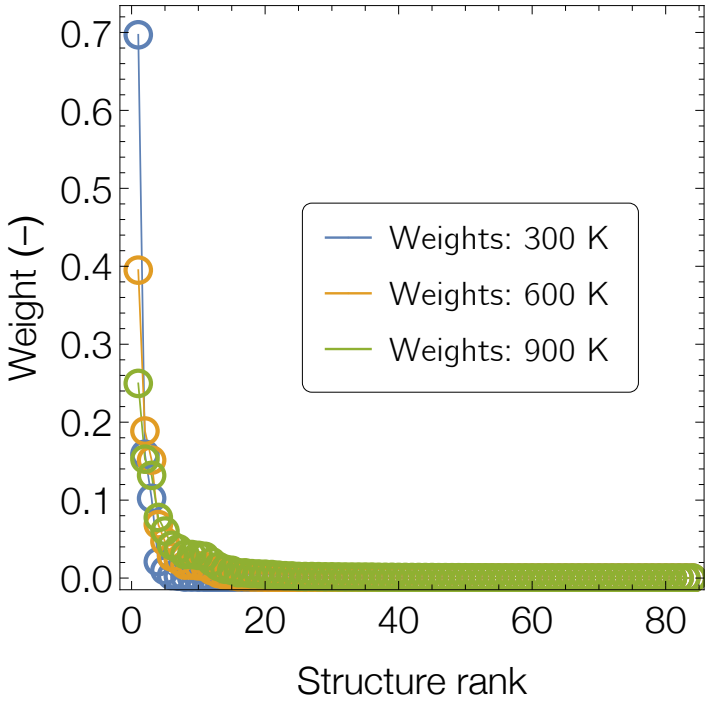

Figure 5.13, Statistical analysis of amorphous *a*-V_2O_5 (001) slabs: average weighted energy.

5.5.3 Structural and Electronic Properties of Selected a-V_2O_5 Slabs

The selected structures for detailed structural and electronic evaluation are QR1-#10, QR1-#11, and QR10-#18. The relaxed structures of the selected *a*-V_2O_5 (001) slabs are shown in Figure 5.14. While these structures show noticeably lower long-range order in their motifs, they form a nice slab shape, which is important for constructing *a*-V_2O_5/H-diamond heterostructures with homogeneous acceptor layer on top of the H-diamond surface.

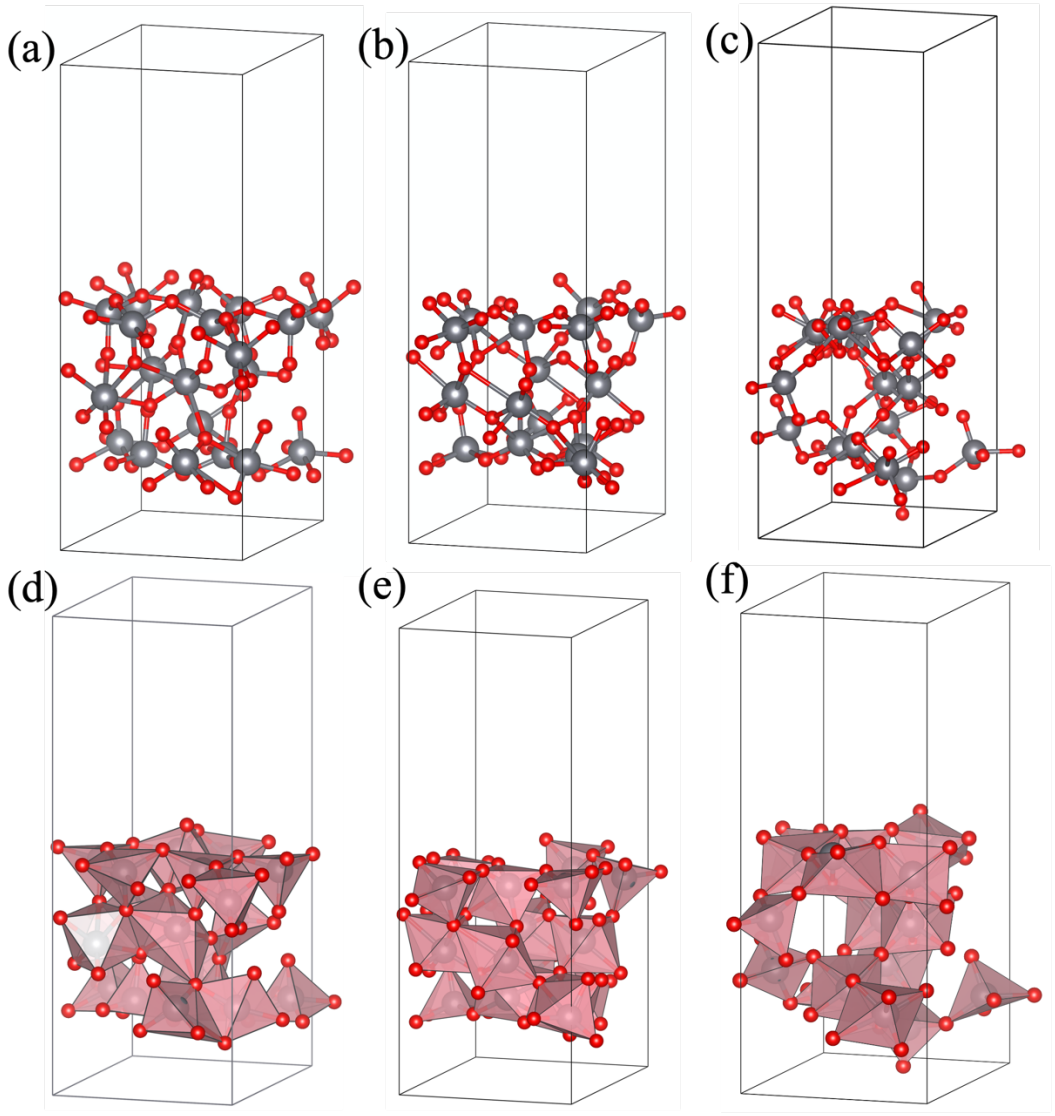

Figure 5.14, relaxed atomic structure of the selected *a*-V_2O_5 (001) slabs: (a – c) ball-and-stick view, and (d – f) polyhedral view of QR1-#10, QR1-#11, and (c) QR10-#18 models.

To further evaluate the short-range and long-range order in the selected *a*-V_2O_5 (001) slabs, we plotted the pair distribution function g(r) for V-V, V-O, and O-O element pairs (Figure 5.15). Like the bulk *a*-V2O5, the first V-O peak shoulder of *c*-V2O5 is vanished, and the dominant peaks below 4.0 Å (corresponding to the first coordination shells of V and O) are nearly preserved, with slight variations among the three tested samples. A distinct feature

observed in g(r) for *a*-V_2O_5 slabs is the presence of two or more O-O peak shoulders below 4.0 Å. These peak shoulders were not observed in the g(r) for *a*-V_2O_5 bulk and *c*-V_2O_5, indicating a larger variation in the coordination of O in the slabs. Here, the peaks above 4.0 Å are broadened and have lower intensity compared to *c*-V_2O_5, suggesting the absence of medium-range and long-range orders in the *a*-V_2O_5 slabs.

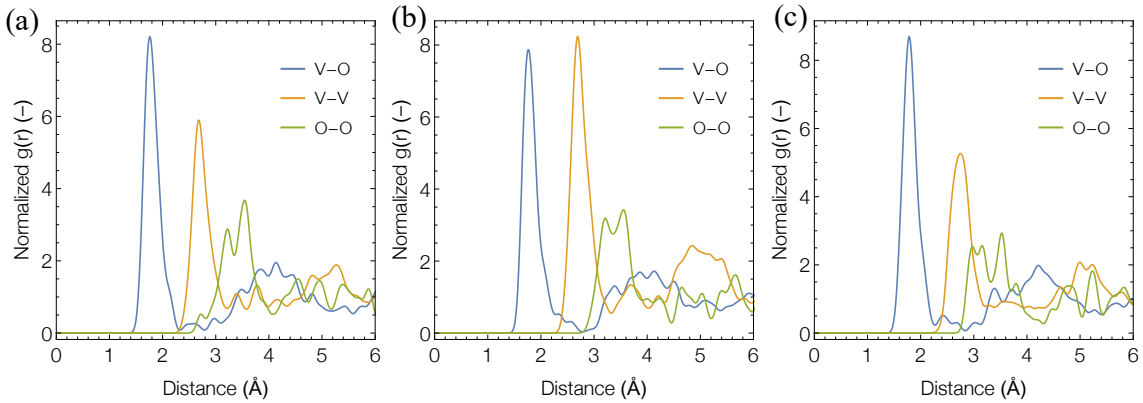

Figure 5.15, pair distribution function for the selected *a*-V_2O_5 (001) slabs: (a) QR1-#10, (b) QR1-#11, and (c) QR10-#18

The atom-projected density of states and the corresponding electronic properties for the selected *a*-V_2O_5 (001) slabs are depicted in Figure 5.16 and Table 5.6, respectively. Here, similar to the bulk amorphous samples, the states from O and V are mainly contributing to the VBM and CBM respectively.

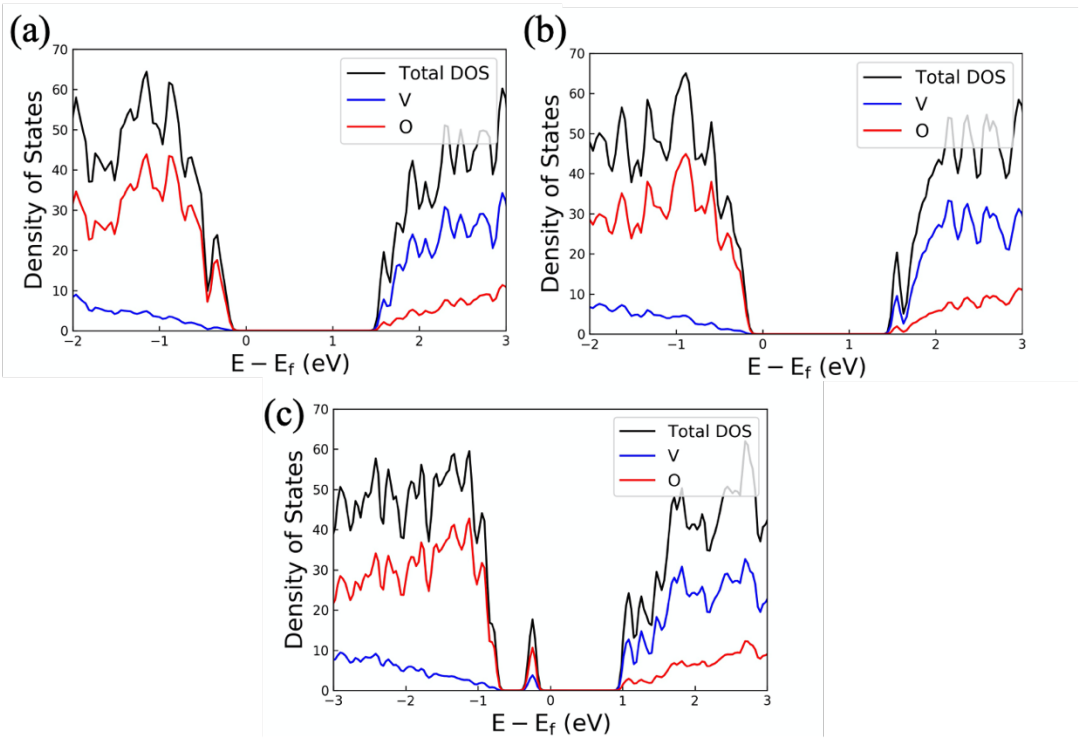

Figure 5.16, Atom-projected density of states for the selected a-V_2O_5 (001) slabs: (a) QR1-#10, (b) QR1-#11, and (c) QR10-#18

The calculated electronic properties of the a-V_2O_5 (001) slabs generated at 1 $K.ps^{-1}$, including $E_f - E_v$, $E_c - E_f$, and E_g are comparable to the amorphous bulk system with minor difference. This agreement between the bulk and slabs behavior is desirable and an indicative that the slab thickness is properly selected and modeled. For all structures, the conduction band is closer to the fermi level compared to both bulk a-V_2O_5 and c-V_2O_5 (001) slab with comparable thickness. An interesting observation is the presence of a mid-gap state right below the fermi level in the PDOS of QR10-#18, which can act as a charge trap.

Table 5.6, Electronic properties of selected *a*-V_2O_5 slabs

System	$E_f - E_v$	$E_c - E_f$	E_g
QR1 - #10	0.243	1.558	1.801
QR1 - #11	0.221	1.518	1.739
QR10 - #18	0.631	0.875	1.506

5.6 Structural and Electronic Properties of *a*-V_2O_5 /H-diamond (100)

To evaluate the structure and electronic charge transfer at the interface of *a*-V_2O_5 slabs and H-diamond (100), we generated heterostructures using the selected *a*-V_2O_5 slabs and the 2×1 reconstructed H-diamond (100) surface. For this purpose, the smallest box to allow rearrangement of atoms in an amorphous form was found to have a surface area of 3× the 2×1 reconstructed H-diamond (100) surface, which is equivalent to 10.089 × 7.567 $Å^2$. To generate the heterostructures, the amorphous slabs were initially placed at a van der Waals (vdW) spacing of 1.8 Å. The structures were then relaxed using DFT calculations as implemented in VASP, relaxing all the atoms in the *a*-V_2O_5 slabs and the first four carbon layers in H-diamond. Figure 5.17 illustrated the relaxed *a*-V_2O_5/H-diamond (100) structures. The adhesion energies (E_{ad}) of the heterostructures were computed using equation 4.1 in chapter 4. The resulting values are presented in Table 5.7.

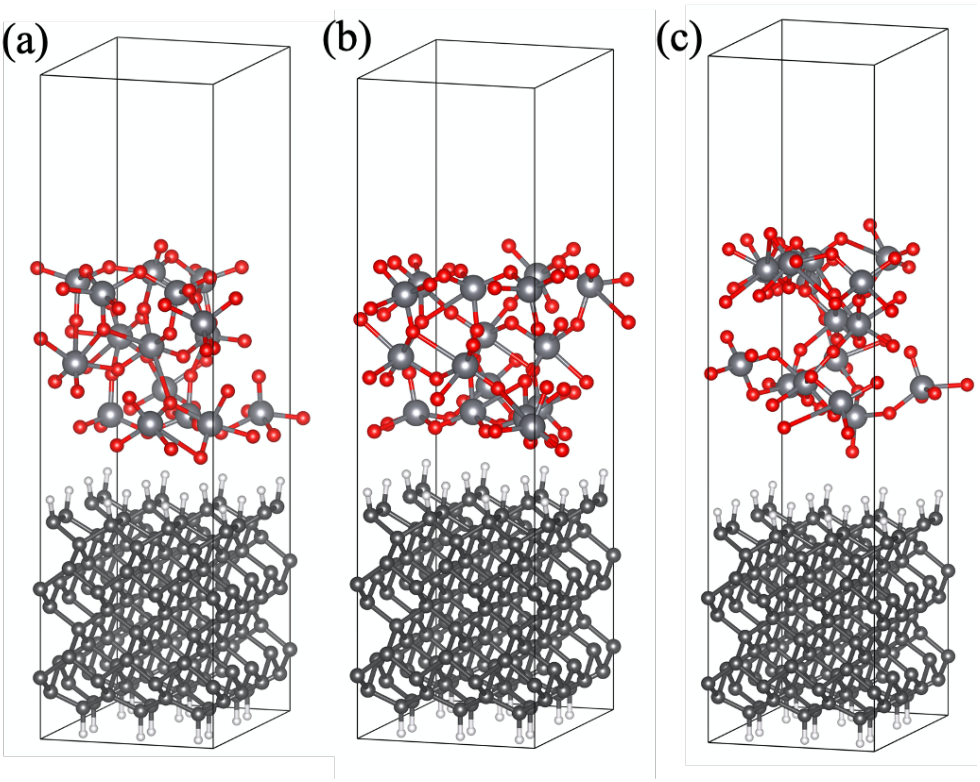

Figure 5.17, relaxed atomic structure of *a*-V_2O_5/H-diamond (100) heterostructures generated using (a) QR1-#10, (b) QR1-#11, and (c) QR10-#18 *a*-V_2O_5 slabs.

To evaluate the charge transfer across the interface of *a*-V_2O_5 and H-diamond, we computed the charge density difference ($\Delta\rho$) using equation 4.3. The resulting charge difference maps for the *a*-V_2O_5/H-diamond (100) heterostructures are shown in Figure 5.18. Here, the areas enclosed by yellow and blue surfaces represent regions with electron gain and loss, respectively. To quantify the electron density, we performed Bader charge analysis [73]. The results are presented in Table 5.7.

Table 5.7, The calculated adhesion energy (E_{ad}), electron gain and loss, and charge density for *a*-V_2O_5/H-diamond (100) systems

System	E_{ad} (eV)	Total electron gain by layer	Total electron loss by H-diamond	Charge density (cm^{-2})
QR1-#10	-0.989	0.482	0.482	6.32×10^{13}
QR1-#11	-0.998	0.515	0.515	6.74×10^{13}
QR10-#18	-0.980	0.385	0.385	5.04×10^{13}

The $\Delta\rho$ isosurface shows electron depletion (~ hole accumulation) at the surface of H-diamond (100), and electron gain by *a*-V_2O_5 atoms interfacing with H-diamond. This observation shows electron transfer from H-diamond surface to the *a*-V_2O_5 layer. Previous studies have reported similar electron transfer from H-diamond surface to *c*-V_2O_5 [146], MoO_3 [16], [146], etc. The evaluated charge density at the interface of H-diamond is 5.04×10^{13} cm^{-2} to 6.74×10^{13} cm^{-2}, which is larger compared to the DFT-calculated charge density difference reported for *c*-V_2O_5 interfaced with H-diamond (100) (2.17×10^{13} cm^{-2}) [146]. The larger charge density difference observed for the amorphous slab compared to the crystalline counterpart could arise from the presence of structural defects acting as traps that facilitate electron transfer in this system. In addition, $\Delta\rho$ maps indicate that most of the charge is transferred from the surface layers of diamond, which is in desirable for device fabrication. As expected, structures with stronger adhesion energy show larger charge density difference across the interface.

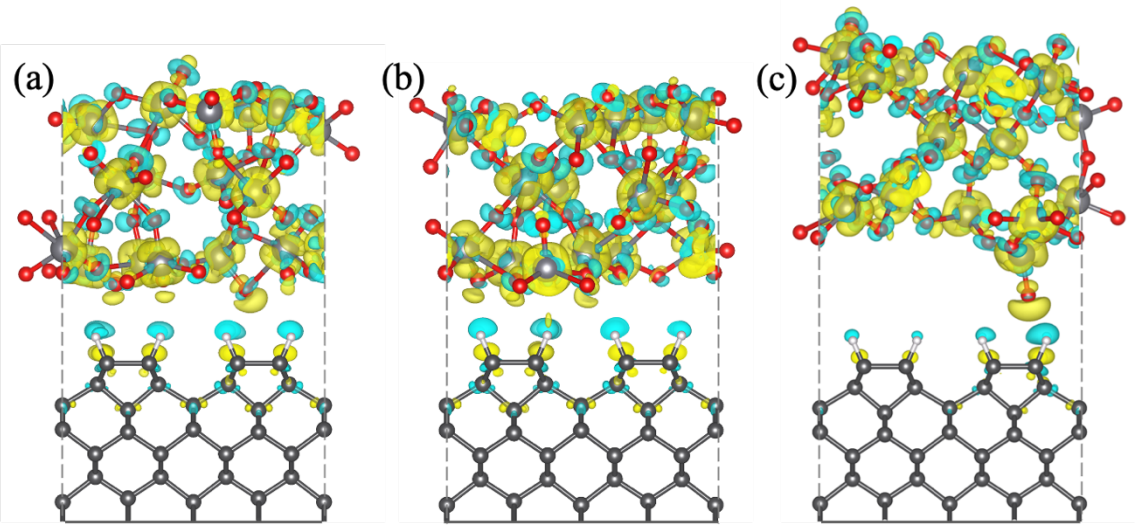

Figure 5.18, charge density difference maps for a-V_2O_5/H-diamond (100) heterostructures generated using (a) QR1-#10, (b) QR1-#11, and (c) QR10-#18 *a*-V_2O_5 slabs. The regions bound by yellow and blue show areas with electron gain and loss, respectively.

To gain further insight about the electronic properties at the *a*-V_2O_5/H-diamond (100) interface, we evaluated the site-projected density of states for the modeled heterostructures, as depicted in Figure 5.19 (a – c). To enable electron transport from H-diamond surface to the acceptor layer, the VBM of H-diamond needs to be placed above the LUMO of the acceptor layer after interfacing. In the site-projected density of states plots, the VBE of H-diamond crosses the CBE of the *a*-V_2O_5 layer, which is an indication of charge transfer from H-diamond to the *a*-V_2O_5 adsorbate. We also plotted the density of states (DOS) for H-diamond (100) substrate before and after interfacing with the *a*-V_2O_5 adsorbate (Figure 5.19 (d – f)). For all the studied heterostructure, we observe a shift of states to higher energies in DOS of H-diamond after interfacing with the *a*-V_2O_5 slabs. Additionally, in the DOS of H-diamond after heterostructure formation, the VBE states cross the fermi level, and the density of CBE states has decreased significantly. This indicates that some previously occupied states have become empty. This observation provides further proof for

electron transfer after *a*-V_2O_5 deposition and is consistent with previous DFT studies of *c*-V_2O_5/H-diamond (100) system [146].

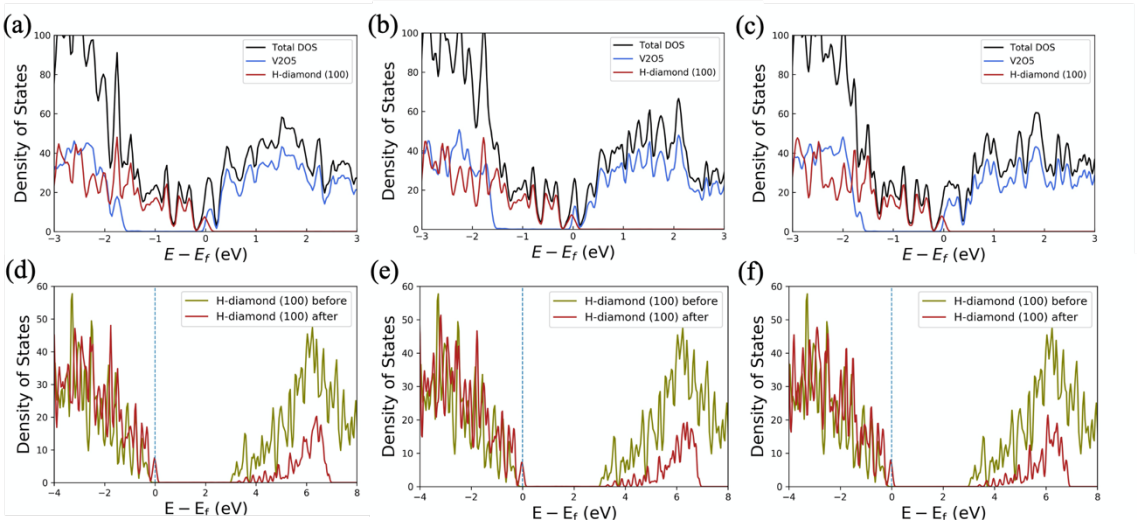

Figure 5.19, (a – c) site-projected density of states for *a*-V_2O_5 /H-diamond (100) heterostructures with QR1-#10, (b) QR1-#11, and (c) QR10-#18 *a*-V_2O_5 slabs, respectively. (d – f) density of states plots of H-diamond (100) before and after it is interfaced with *a*-V_2O_5 slab with QR1-#10, (b) QR1-#11, and (c) QR10-#18 conformations, respectively.

5.7 Conclusions

In this chapter, we presented a novel method for modeling amorphous oxide slabs, and implemented this method to perform computational analysis of *a*-V_2O_5 slabs. To present a comprehensive prediction that is representative of experimentally grown slabs, we performed statistical evaluation of various *a*-V_2O_5 polymorphs. The *a*-V_2O_5 slabs show *n*-type doping and, in some cases, mid-gap states, which can facilitate charge transfer at the interface of H-diamond. Furthermore, we evaluated *a*-V_2O_5 /H-diamond heterostructures and demonstrated that the generated *a*-V_2O_5 slabs can be utilized as an acceptor layer to facilitate surface doping of H-diamond. We also observed that the defects in *a*-V_2O_5 slabs, acting

as charge traps, enable higher charge transfer as compared to *c*-V_2O_5 reported in the literature.

6. Accelerating computational exploration of surface structures

6.1 Overview

In this chapter, we report a novel approach based on Bayesian Inference optimization to accelerate computational studies of molecule-molecule or molecule-surface interactions. In these problems, we often deal with numerous choices for selecting the initial molecule configuration. The traditional method of finding the lowest energy structure is to perform and compare several possible simulations. Not only the common trial-and-test approach requires performing many calculations to increase the chances of success, but different simulations also often converge at the same result, which is a waste of computational effort. As opposed to this inefficient method, the Bayesian inference optimizer uses past observations to predict the behavior of many other possible structures, leading to faster computations. Our method couples Gaussian Processes (GPs) and atomistic simulations to accelerate the search for the minimum energy structure. We also introduce a method based on integrating forces with the Bayesian inference model to accelerate prediction at no additional computational effort.

To demonstrate application of the proposed method and verify its' accuracy, we used the approach to study water molecules on the zinc oxide semi-polar surface. However, the presented approach can be used to study molecule surface interactions in other material systems. Therefore, it addresses a long-standing challenge in computational chemistry and any other problem in which we deal with a large dataset and overlap of the targets.

6.2 Background and Related Works

A perennial challenge in computational chemistry is the process of finding the minimum energy configuration of weakly interacting molecules, or molecules interacting with a surface. The minimum energy configuration indicates the most stable structure, corresponding to the structure with the highest chance to grow in experiment. Hence, finding the minimum energy configuration is critical for many applications, such as designing efficient hydrogen fuel generators, water purification reactors, aircrafts for enduring harsh environments, and targeted drugs. Figure 6.1 shows a few samples of a molecule interacting with a surface, ranging from a small molecule (water on ZnO) to a large biomolecule (a protein on various surfaces). To determine the stability of surface attachments, we need to find the structure corresponding to the global minimum energy (GME). The problem, however, is that we often have many options for choosing the initial attachment configuration. Thus, developing a time and cost-efficient approach to search for the GME is imperative for computational chemistry research.

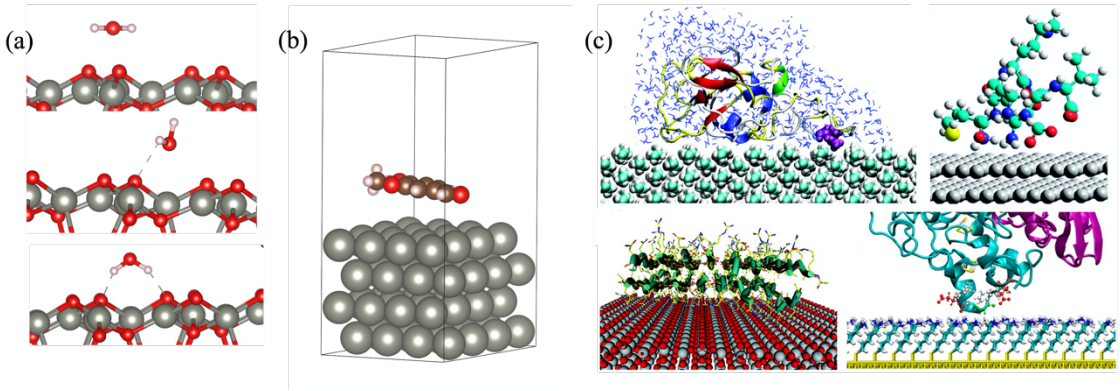

Figure 6.1, Atomic structure of sample molecule-surface interactions, including (a) a few configurations of water molecule on ZnO surface, (b) vanillin molecule on Zn (001) slab, and (c) proteins on various surfaces [160].

The traditional method implemented in determining the GME is by performing quantum or classical simulations. Density functional theory (DFT) calculations and molecular dynamics (MD) simulations are two common methods used to perform quantum and classical simulations, respectively. DFT can provide an accurate estimation of materials properties when their atomic or molecular structure is known [27]. However, its' time complexity is $O(N^{3-4})$, where N is the density of electrons. This makes DFT very slow and computationally impracticable for studying large material systems. MD simulations study movements and interactions between atoms and molecules [161]. Therefore, they can be used to analyze relatively larger material systems, but they do not provide the accuracy of DFT. Materials scientists are therefore searching for a method, which provides an accuracy of DFT, but performs much faster. To find the GME using the traditional method, one would make a guess for the initial structure, relax the geometry using atomistic simulations, compare energies of different structures formed through the geometry relaxation, pick the structure with the minimum energy among them, and hope it is the GME. Figure 6.2 (a) and (b) illustrate a few possible water attachment configurations on the ZnO $(10\bar{1}0)$ surface, and

the schematic energy plot of these configurations, respectively. The complexity of this problem is twofold: First, there are a large number of options for choosing the initial molecule configuration. Further, some of these structures will relax to the same local minimum well as shown in Figure 6.2 (b) and (c). Although performing more calculations increases the chances of finding the GME, there is no way to guarantee that the GME is found with this approach. Not only the traditional method requires performing many calculations, but different calculations also often converge at the same result which is a waste of computational effort. Thus, developing a time and cost-efficient approach to find GME is important in quantum chemistry.

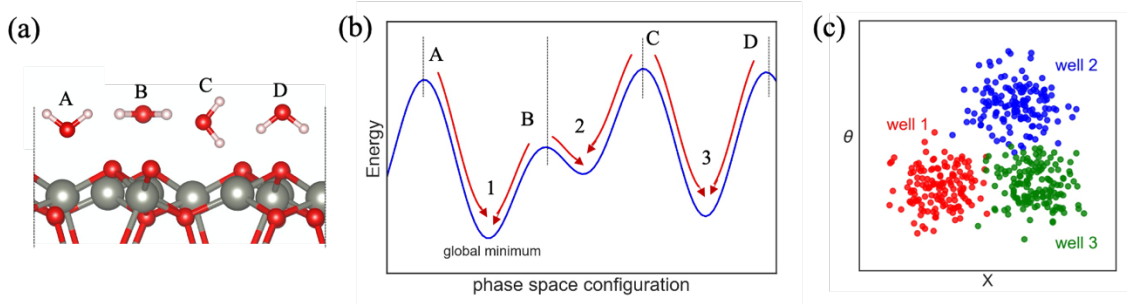

Figure 6.2, (a) different configurations of water molecule attachment on ZnO $(10\bar{1}0)$ surface, (b) and (c) schematic energy plot and Bayesian sampling of data, respectively.

Materials scientists are actively looking for alternative methods that allow fast and accurate discovery of novel materials. With advances in computer science, researchers have become interested in incorporating machine learning (ML) and artificial intelligence (AI) models to accelerate computational discovery of materials. Previous studies have incorporated ML and AI models to predict materials properties [162]–[164], develop force fields [165], [166], and predicting atomic structure of materials using large databases [167]. Mathematical models including evolutionary algorithms [168], basin hoping [169], and high

throughput (HT) [170] were developed to deal with the large stream of data in structure prediction. Different ML models, including regression [167], random forest [171], [172], neural networks [173]–[175], etc. have been used to study material systems computationally. Although these ML models are advantageous for studies of material systems, their training efficiency and accuracy significantly depends on the availability of a large dataset, which limits their performance where access to large datasets is limited. For instance, for complex materials systems, generating a large dataset through atomistic simulations is time-consuming and costly. In these cases, we seek an alternative approach, which does not heavily depend on the data size. Statistical models are on the other hand useful when dealing with complex systems and high uncertainty levels. They do not rely on large datasets and have the benefit of capturing the likelihood associated with each data point. Lately, Todorovic et. al presented the Bayesian Optimalization Structure Search (BOSS) method to accelerate potential energy surface (PES) computations in DFT [176]. BOSS considers the GPs posterior mean as the most likely PES for a given set of data and was found to yield convergence after around 600-700 steps for up to 6-dimensional space. The Fast learning of atomistic rare events (FLARE) was developed using a Bayesian approach to train force fields in MD simulations. FLARE uses the uncertainty of GPs to decide whether to accept the predicted forcefields or to perform additional DFT simulations [177]. Although the previous models have shed light on accelerated materials discovery and contributed to inspiration for the presented work, they have problems such as being limited to lower dimensions, not accounting for energy gradients and materials symmetry. Moreover,

applying ML and AI to materials science is in early stages and requires more in-depth studies to generate robust models that can handle complex real-world systems.

Herein, we present a statistical approach based on Bayesian Inference to accelerate the search for the minimum energy structure. In this method, we use GPs to tease out new and useful information from the auxiliary data generated in the process of classical or quantum simulations. The GPs predictions are used to decide the molecule's configuration in the next simulation setup. This enhances chances of exploring dissimilar regions of the potential energy surface (PES), which leads to faster prediction of GME. One important innovation that we introduce is using energy gradient (forces) to update the GP belief. Integration of forces was found to significantly improve the model's performance.

6.3 Methods and Modeling

This section presents an overview of the concepts, method, code implementation, feature selection, and data preprocessing.

6.3.1 Multivariate Normal Distributions

The multivariate normal (MVN) distribution, also called multivariate Gaussian Distribution, of X can be written as $\mathcal{N}(\mu, \Sigma)$, where X is a k-dimensional random vector, μ is the k-dimensional vector of means, called mean vector, and Σ is the $(k \times k)$ covariance matrix. If Σ is *positive-definite*, which means all of its' eigenvalues are positive, the distribution density can be defined as [178],

$$f_x(x_1, \dots, x_k) = \frac{exp(-\frac{1}{2}(x-\mu)^T\Sigma^{-1}(x-\mu))}{\sqrt{(2\pi)^k|\Sigma|}} \tag{6.1}$$

here, $|\Sigma|$ represent the determinant of Σ , and x is a real k-dimensional vector. For two variables (a bivariate problem), the probability density function can be written as [37],

$$f(x,y) = \frac{1}{2\pi\sigma_X\sigma_Y\sqrt{1-\rho^2}} e^{-\frac{1}{2(1-\rho^2)}[\left(\frac{x-\mu X}{\sigma_X}\right)^2 - 2\rho\left(\frac{x-\mu X}{\sigma_X}\right)\left(\frac{x-\mu Y}{\sigma_Y}\right)+\left(\frac{x-\mu Y}{\sigma_Y}\right)^2]} \tag{6.2}$$

here, both σ_X and σ_Y are positive, and ρ denotes the correlation between X and Y defined as,

$$corr\ [X,Y] \triangleq \frac{Cov[X,Y]}{\sqrt{\mathbb{V}[X]\mathbb{V}[Y]}} = \frac{\sigma_{XY}^2}{\sigma_X\sigma_Y} \tag{6.3}$$

μ and Σ are found via,

$$\mu = \begin{pmatrix}\mu_X \\ \mu_Y\end{pmatrix} \tag{6.4}$$

$$\Sigma = \begin{bmatrix}\sigma_X^2 & \rho\sigma_X\sigma_Y \\ \rho\sigma_X\sigma_Y & \sigma_Y^2\end{bmatrix} \tag{6.5}$$

The diagonal of Σ represents the variances for each random variable, while the off-diagonal elements show the correlation between X and Y random variables.

6.3.2 Gaussian Processes and Bayesian Inference

Gaussian processes (GPs) are used in machine learning and artificial intelligence to make predictions based on some prior knowledge. GPs allow us to assign a probability to each possible prediction and evaluate the uncertainty. While GPs are widely used in regression

problems to model a function, such as time series forecasting, they can also be used to tackle clustering and classification problems [179].

GPs are built based on multivariate Gaussian distributions. One important algebraic property of Gaussian distributions is that they are closed with respect to marginalizing and conditioning. This means that after performing these operations, the result will still be a Gaussian distribution.

To obtain partial information from MVN distributions, we can marginalize out some variables from the distribution. According to Ref. [180], factor marginalizing is defined as "let $\boldsymbol{X}$ be a set of variables, and $Y \notin \boldsymbol{X}$ a variable. Let $\phi(\boldsymbol{X}, Y)$ be a factor. We define the factor marginalization of Y in ϕ, denoted $\sum_Y \phi$ to be a factor ψ over $\boldsymbol{X}$ such that,

$$\psi(\boldsymbol{X}) = \sum_{Y} \phi(\boldsymbol{X}, Y) \tag{6.6}$$

Here, $\boldsymbol{X}$ is a subset of X. A factor ϕ is a function that maps a set of random variables to $\mathbb{R}$. This operation is also referred to as summing out Y in ψ. In a Bayesian network, if we want to marginalize a joint distribution $P(\boldsymbol{X}, Y)$ onto $\boldsymbol{X}$, we can sum out Y.

Conditioning refers to finding the probability of a variable given some information about another variable. We can define the conditional distribution, as [180],

$$P(Y|X) = \frac{P(X,Y)}{P(X)} = \frac{P(X|Y)P(Y)}{P(X)} \tag{6.7}$$

This is also equivalent to the simple Bayes rule, where given a prior knowledge $P(Y)$ and some likelihood $P(X|Y)$, we solve for the posterior $P(Y|X)$.

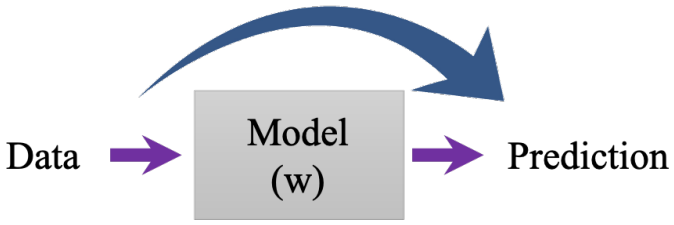

Figure 6.3, Simple illustration of Gaussian Processes (GPs) and Bayesian Inference as compared with discriminative machine learning models. In GPs, we skip the modeling part and directly use the data for prediction.

Using GPs, we can learn the underlying distribution of the trainset data *Y* given some known datapoints *X*. To perform regression, we can treat this problem as a Bayesian Inference. The posterior predictive distribution is [179],

$$P(Y|D,X) = \int_w P(Y,w|D,X)dw = \int_w P(Y|w,D,X)P(w|D)dw \tag{6.8}$$

here, *D* shows the set of data which *X* and *Y* subsets are driven from, and *w* shows the set of parameters that need to be optimized in a machine learning model. In simple words, through marginalizing out *w*, we eliminate the need to generate a model. This helps us skip the modeling part, which significantly reduces the required data size to make reliable predictions (**Error! Reference source not found.**). As GPs are closed with respect to conditioning and marginalizing, the resulting probability $P(Y|D,X)$ is also a Gaussian distribution and can be written as [179],

$$P(Y|D,X) = \mathcal{N}(\mu_{Y|D}, \Sigma_{Y|D}) \tag{6.9}$$

This simply means that we can define the probability distribution in terms of a mean $\mu_{Y|D}$ and a covariance matrix, $\Sigma_{Y|D}$. The diagonal values in the covariance matrix help us determine the uncertainty of prediction. The word "inference" means "the act of passing from

sample data to generalizations, usually with calculated degrees of certainty", and the term "Bayesian" refers to Inference methods that enable evaluation of the "degrees of certainty" [37]. In Bayesian inference, the predicted distribution and uncertainty are updated as more data becomes available. Figure 6.4 shows a sample Bayesian Inference optimization problem. As more datapoints are observed, the prediction becomes more accurate.

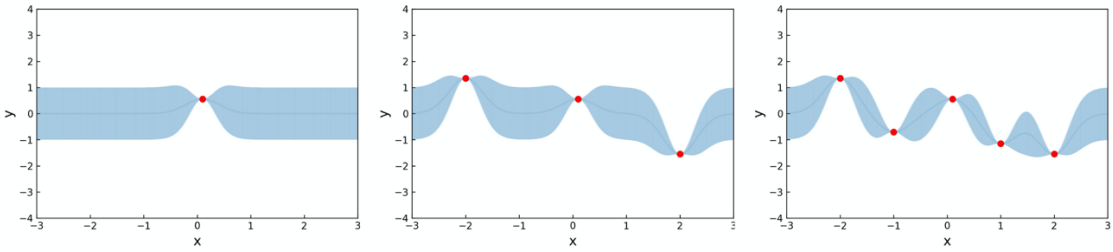

Figure 6.4, Learning a sample function through Bayesian Inference, from left) to right) starting with one prior datapoint and adding two points in each acquisition. As more datapoints are provided, the prediction is updated, and the uncertainty goes down.

6.3.3 Kernels

Kernels are used to define the covariance matrix in GPs. Kernel functions evaluate the pairwise similarity between the data points. There are many kernel functions (also known as covariance functions) which we can choose from. The selected kernel function decides most generalization properties of the GPs and the prediction [181]. Therefore, selecting the right kernel function is very important in determining the GPs' accuracy. The choice of kernel function depends on the characterization of the dataset that we aim to predict. Kernel functions can be stationary or non-stationary. Stationary kernels are invariant with respect to translation, which means that they depend on the distance of points relative to each other, but not the points themselves [182]. Here, we briefly discuss a few common kernel functions, some of which were used in this project.

The first kernel function we discuss here and perhaps the most commonly used kernel is the *squared exponential (RBF)* kernel,

$$k_{RBF} = \sigma^2 \exp\left(-\frac{d\left(x_i, x_j\right)^2}{2l^2}\right) \tag{6.10}$$

here, l is the length scale, and indicates the cutoff distance along each axis at which the values of function become uncorrelated. σ is the variance, which shows the average distance from the mean of data [179]. x and x_j are two data points, that the kernel function evaluates the similarity between them by incorporating the Euclidean distance $d\left(x_i, x_j\right)$. The kernel function is evaluated for each pair of points in the sample. The *RBF* kernel is a stationary kernel [181].

Next, we discuss the *Matern* class of kernel function, named after the work of *Matern* [1960]. The class of *Matern* kernels is defined as [179],

$$k_{Matern} = \frac{2^{1-\nu}}{\Gamma(\nu)}\left(\frac{\sqrt{2\nu d(x_i, x_j)}}{l}\right)^{\nu} K_{\nu}\left(\frac{\sqrt{2\nu d(x_i, x_j)}}{l}\right) \tag{6.11}$$

This kernel function is considered a generalization to the *RBF*, with an additional parameter ν indicating the degree of smoothness. Larger ν indicates smoother function. In this equation, K_{ν} denotes a modified Bessel function [183]. The spectral density $S(s)$ of the Matern covariance function in D dimensions is given by,

$$S(s) = \frac{2^D \pi^{\frac{D}{2}} \Gamma\left(\nu + \frac{\mathrm{D}}{2}\right)(2\nu)^{\nu}}{\Gamma(\nu) l^{2\nu}}\left(\frac{2\nu}{l^2} + 4\pi^2 s^2\right)^{-\left(\nu + \frac{\mathrm{D}}{2}\right)} \tag{6.12}$$

for $\nu \to \infty$, the *Matern* covariance function will become equivalent to the *RBF*.

The *dot product* kernel functions are used when the covariance matrix depends only on data points x_i and x_j through their dot product $x_i.x_j$. An example of the *dot product* kernel function is,

$$k(x_i, x_j) = \sigma_0^2 + x_i.x_j \tag{6.13}$$

This can be found by using linear regression with putting $\mathcal{N}(0,1)$ priors on the coefficients of $x_d(d = 1, \dots, D)$ and a prior of $\mathcal{N}(0, \sigma^2)$ on the bias [179]. The *dot product* kernel functions are invariant with respect to rotation, but not translation. Therefore, they are categorized as non-stationary kernel functions.

If our feature set contains multiple datatypes, we can combine or modify the kernel functions. To combine kernels, we can use various methods based on the problem. Some of the methods used for combining kernels include summation, product, vertical rescaling, convolution, direct sum tensor product, additive model, and functional ANOVA. A good description of these methods can be found in Ref. [179]. The sum and product rules state that the sum of two kernels is a kernel, and the product of two kernels is also a kernel. The proofs for these are available in Ref. [179].

In addition to selecting/constructing appropriate kernel functions, one also needs to find the proper hyperparameters (the free parameters of the kernel function). The hyperparameters of a kernel function can be optimized through maximizing the log marginal likelihood (LML). The marginal likelihood $p(y|X)$ is defined as,

$$p(y|X) = \int p(y|f, X)p(f|X)df \tag{6.14}$$

which is the integral of likelihood times prior marginalized over the latent function values f. For linear regression, $f(x) = x^{\top}w$, with x equal to the vector of input data and w denoting the weights vector (linear regression parameters), which is related to the observed target y by $y = f(x) + \varepsilon$.

In the GP model, $f|X \sim \mathcal{N}(0, K)$ and $y|f \sim \mathcal{N}(f, \sigma^2 I)$. Therefore, the log marginal likelihood conditioned on the hyperparameters of the covariance function (θ) can be written as,

$$\log p(y|X,\theta) = -\frac{1}{2}y^T\left(K_y\right)^{-1}y - \frac{1}{2}\log\left|K_y\right| - \frac{n}{2}log2\pi \tag{6.15}$$

here, σ_n^2 is the noise variance and K_y , is the covariance matrix of the noisy data, which is related to the covariance of the noise-free latent function K through $K_y = K + \sigma_n^2 I$. The first term in equation 6.15 is data-fit which involves the observed target y. The second term is the complexity penalty, and the last term is a normalization constant. As the length scale grows, the model becomes less complex, and the negative complexity penalty goes up. To find the set of hyperparameters θ that maximizes the LML, we need to solve the partial derivative of LML with respect to the hyperparameters,

$$\begin{aligned}\frac{\partial}{\partial\theta_j}\log p(y|X,\theta) &= \frac{1}{2}y^T K^{-1}\frac{\partial K}{\partial\theta_j}K^{-1}y - \frac{1}{2}tr\left(K^{-1}\frac{\partial K}{\partial\theta_j}\right)\\ &= \frac{1}{2}tr\left((\alpha\alpha^T - K^{-1})\frac{\partial K}{\partial\theta_j}\right) \text{ with } \alpha = K^{-1}y\end{aligned} \tag{6.16}$$

This could be either done by computing the derivatives, which has a time complexity of $O(n^3)$ for kernel inversion and $O(n^2)$ for the rest, or by using a gradient-based optimizer [179].

6.4 Model Description

6.4.1 Feature Selection and Data Preprocessing

For this project, we considered a six-dimensional (6D) feature space, based on the displacement and rotation of a reference molecule. The selected features were the translation of the molecule's center of mass (x, y, z) and the three angles (θ, ϕ, α) defining the rotation of the molecule about its center relative to a reference molecule. The first two of these angles are the polar and azimuthal angles of the rotation axis and α is the angle of rotation around this axis. The total energies were selected as the target. The validation data was computed by selecting a random combination of $x, y, z, \theta, \phi, \alpha$, transforming the reference molecule according to there, and then performing a single step molecular dynamics calculation to compute the energy of the entire water/substrate system with the water molecule in this configuration.

6.4.2 Model: Main

To couple GPs and atomic simulations, the Gaussian Processes package from scikit-learn ML library [184] was integrated with the LAMMPS MD simulation package [153] in a serial Python code.

Initially, we performed a single noninteractive GP acquisition. For this part, we generated a large dataset using MD simulations. This dataset was split into train and validation sets.

We fitted the GP function to the train set and predicted the total energy values for the validation set. We tested this approach with various kernel functions and hyperparameters. The hyperparameters were optimized during fitting of the GP function through maximizing the LML. In addition, we evaluated the effect of train size on the accuracy of the prediction.

Then, we interactively used a GP acquisition and MD simulations to search for the minimum energy structure. In the interactive mode, we generated a validation set using MD simulations. We started with generating a prior train set of random configurations of a molecule on the surface and their total energies computed from MD simulations. We fit a GP function to this prior set and computed the predicted energies for the validation set. We then added new samples to the train set and repeated the process. The added configurations at each step were selected to obtain a trade-off between minimizing the energy $y(\theta)$ and maximizing the variance (probing less visited regions). We performed this exploratory action by minimizing the acquisition function $A_t(\theta)$, defined as [185],

$$A_t(\theta) = y(\theta) - \eta_t \, v_t(\theta) \tag{6.17}$$

where $\eta_t^2 = 2log[t^{d/2+2}\pi\text{^}2 /(3\varepsilon_\eta)]$, ε_η is a constant with a small value, and $v_t(\theta)$ is the posterior variance. This interactive learning was carried on until convergence.

To obtain a more uniform sampling across the space, we analyzed a second sampling approach by generating a large pool of random samples, from which we selected structures that minimize the acquisition function (6.17). This approach is explained in more details for the case-studies of water molecule on ZnO in the next sections.

To implement forces, in each iteration, in addition to the configurations that minimize the acquisition function (6.17), we also generated a set of phantom points by displacing the molecule along the forces' direction. The energies of the generated phantom points are computed by taking the integral of the forces with respect to position via $U = -\int_{r_0}^{r} \vec{F}.\overrightarrow{dr}$, with $\overrightarrow{dr} = dx\hat{\imath} + dy\hat{\jmath} + dz\hat{k}$ as the displacement in a 3D space.

In the following sections, we present the application of the presented approach to study the problem of water molecules interacting with the ZnO $(11\bar{2}2)$ surface for: non-interactive learning using GPs, interactive learning coupling GPs and MD simulations, and integration of forces in non-interactive and interactive modes.

6.5 Case Study One: Water on ZnO, non-interactive

In this section, we report the results for performing one GP acquisition on a dataset generated using MD simulations (non-interactive mode). The results are presented for a dataset of molecules randomly shifted in xy (2D search space) and a dataset of molecules randomly shifted in xyz and rotated (6D).

6.5.1 Molecule Shifted Only in xy

We generated a dataset of a water on ZnO surface by randomly shifting the water molecule in x and y coordinates and computing their total energies using MD simulation. The optimized hyperparameters were selected according to the dataset, train size, and minimizing LML. Figure 6.5 depicts the train and validation prediction plotted vs. the true values of total energy for a single GP acquisition using 2000 train and 500 validation points. The results indicate accurate train and validation predictions. Qualitatively, the average and

maximum uncertainty of prediction were found to be 0.48 *kcal/mol* and 0.09 *kcal/mol*, respectively. The mean squared error is 0.007 *kcal/mol*.

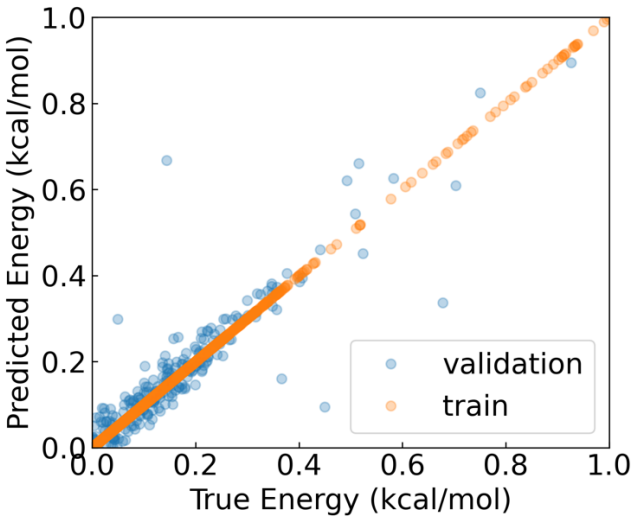

Figure 6.5, Plot of predicted vs. true energy. Train and validation points were regularized to obtain a range in (0,1).

Figure 6.6 shows the average uncertainty and mean squared error of prediction plotted as a function of train size. Accordingly, a train set of 500 datapoints was found to result in convergence of the mean squared error. Although such convergence is not achieved in the average uncertainty data, we note that to properly analyze the uncertainty, one should check the values of uncertainty at each point.

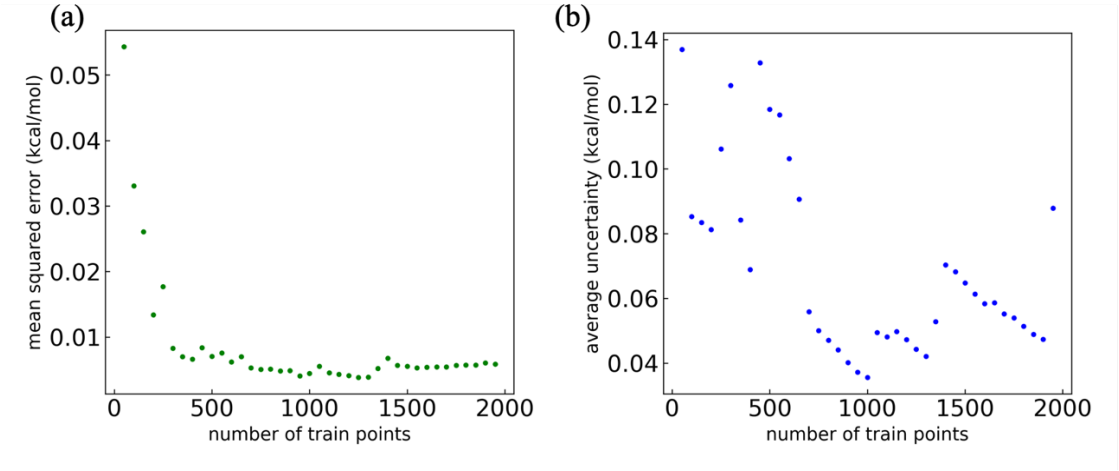

Figure 6.6, Plots of (a) Mean squared error, and (b) average uncertainty vs. train size for dataset of water-on-ZnO with water molecule shifting only in *x* and *y* axes.

6.5.2 Molecule Shifted in xyz and Rotated

The dataset for this part, was generated by randomly rotating and shifting the water molecule in x, y, z coordinates and computing their total energies using MD simulation. Figure 6.7 shows the relation between the predicted and true energies. A single GP acquisition using 2000 train and 500 validation points was performed. The average and maximum uncertainty of prediction are 0.12 *kcal/mol* and 0.04 *kcal/mol*, respectively. As the 6D problem is more convoluted than searching the 2D space, one would expect a slightly lower performance.

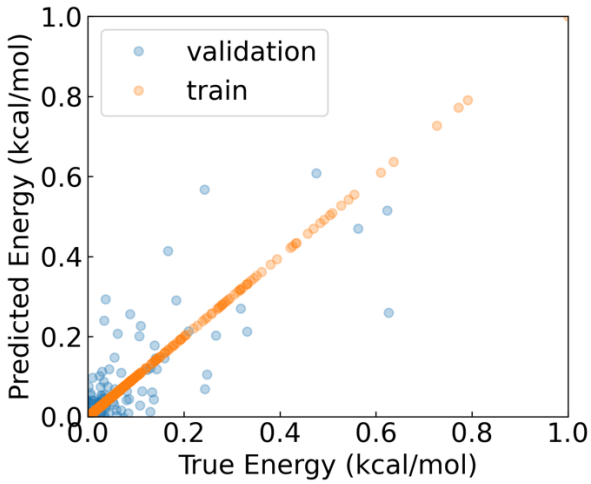

Figure 6.7, Predicted vs. True energy values for the train and validation sets after a single GP acquisition.

Figure 6.8 shows the mean squared error and the average uncertainty as a function of the train size. The uncertainty of prediction is converged at 1500 points. This shows the slow performance of single GP acquisition, especially in searching higher dimension. To achieve convergence using less data points, in the next section, we explore using the interactive Bayesian approach.

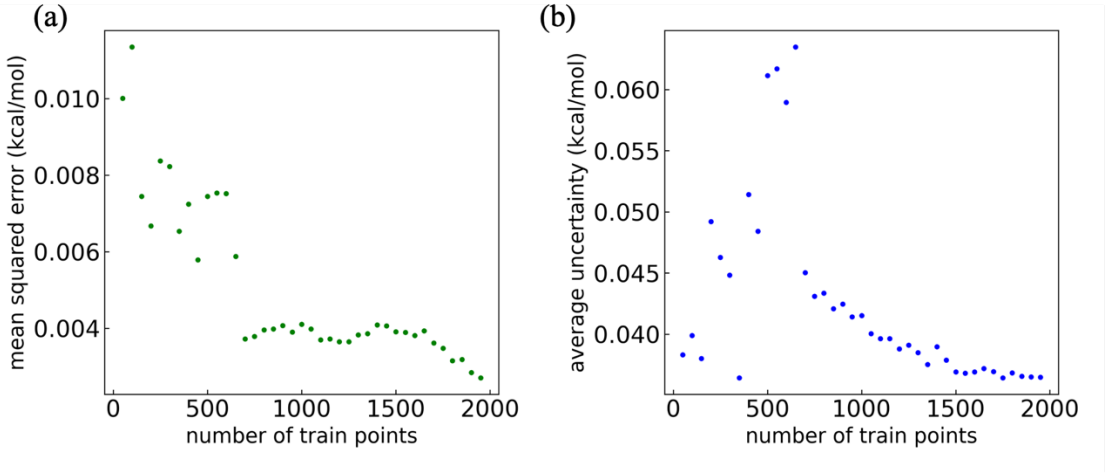

Figure 6.8, Plots of (a) Mean squared error, and (b) average uncertainty vs. train size for water-on-ZnO dataset generated by arbitrary shifting of xyz and angles of the water molecule

6.6 Case Study Two: Water on ZnO, Interactive

In this section, we report the results for interactively performing GP acquisitions and MD simulations to study the water-on-ZnO problem. Here also, we analyze structures with arbitrary configurations of molecule on surface obtained in two ways, simple problem: by shifting the molecule in xy (2D), and a more complicated case: molecules randomly shifted in xyz and rotated (6D).

6.6.1 Molecule Shifted Only in xy

In this section, we investigate implementing the Bayesian approach to study the problem of searching for the minimum energy structure in 2D, i.e., shifting the molecule only along the x and y coordinates, corresponding to two translational degrees of freedom. Searching the energy landscape in 2D is faster compared with higher dimensions. The new structures with shifted molecules in xy are selected using GP predictions and minimizing the acquisition function (equation 6.17). As opposed to a brute force search method, this intelligent

acquisition approach increases probability of visiting new areas, which accelerates the procedure of finding the minimum energy structure.

It is tempting to think that a more efficient convergence could be achieved by performing an optimization search of the acquisition function. However, we find that this process in fact, converges significantly slower than the biased random sampling (Figure 6.9, (a)). The reason for this is that the uncertainty in the GP prediction is largest between samples. As more samples are added, this makes the uncertainty landscape become more complex rapidly increasing the number of local minima in the acquisition function and preventing good coverage of sampling points. Figure 6.9, (b) shows the spatial distribution of the new sampling points generated during the interactive regression process through optimization of the acquisition function. For this approach, a stochastic global optimization scheme is needed. The biased random sampling takes us halfway there. A possibly better approach that will be tested in the future would be to combine biased random sampling followed by local optimization.

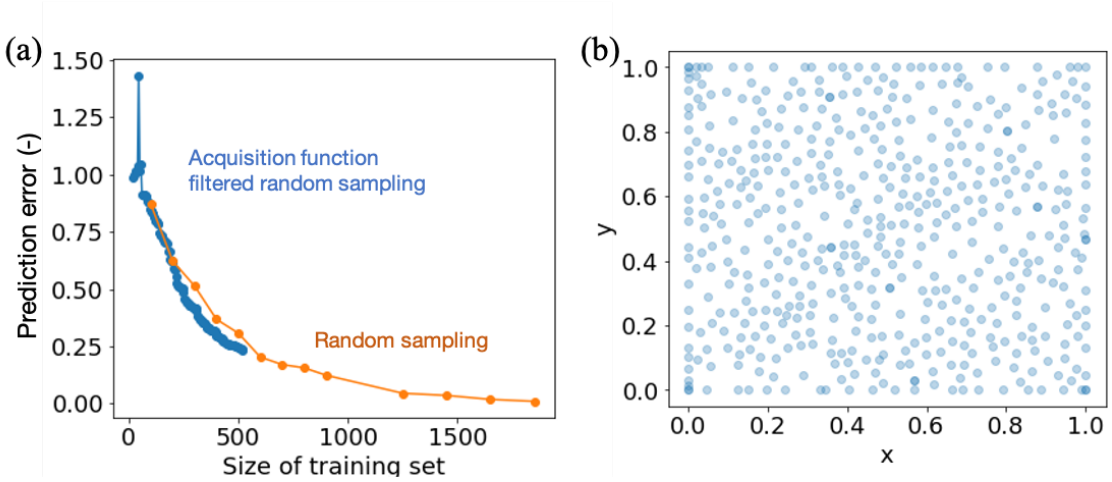

Figure 6.9, (a) Plot of the convergence of the GP regression prediction vs number of data points used acquired in the iterative regression (blue) as compared to non-interactive regression using random sampling (gold). New points are accrued though random sampling with the random samples filtered based on the acquisition function with only the best 0.5% added to the training data. (b) shows the spatial distribution of new sampling points obtained during interactive regression using optimization of the acquisition function. While the points are mostly uniformly separated there exist sparce pockets that a local minimum search is not able to find.

6.6.2 Molecule Shifted in xyz and Rotated

The task of searching the energy landscape in six dimensions (three translational degrees of freedom and three in rotation) is significantly more challenging that just 2D rastering of the surface. Figure 6.10 shows the energy variation that arises from displacing the reference molecule along each of these six degrees of freedom individually. The ZnO substrate is cut on a high index semipolar plane—it has a large repeat unit containing several local minima, and it is highly corrugated leading to very large energy variations if one simply scans the molecule horizontally without varying its height. While periodic in x, y and the angles ϕ and α, it is anti-symmetric in θ, and is not periodic in z. The scale of fluctuations varies by an order of magnitude along different degrees of freedom starting from this reference point. With a brute force scan of the potential landscape in this 6D space, one would expect to need at least three or four points along each dimension, and with several local minima as

there are in x and y, and many more. Four sampling points in each direction would require $4^6 = 4096$ samples, a considerable computational cost, if these are to require full blown density functional theory calculations.

Instead, we use Gaussian process regression using iterative Bayesian inference to identify new molecule configurations, that will deliver the maximum amount of new information to the next iteration of the regression. Specifically, new points were chosen at locations in which the acquisition function (described above) was minimized. Two different approaches were taken for this. The first approach was a standard optimization scheme as implemented in the python *scikit.learn.optimization* module. In this approach, 10 new points were generated by running the minimization from randomly selected starting points.

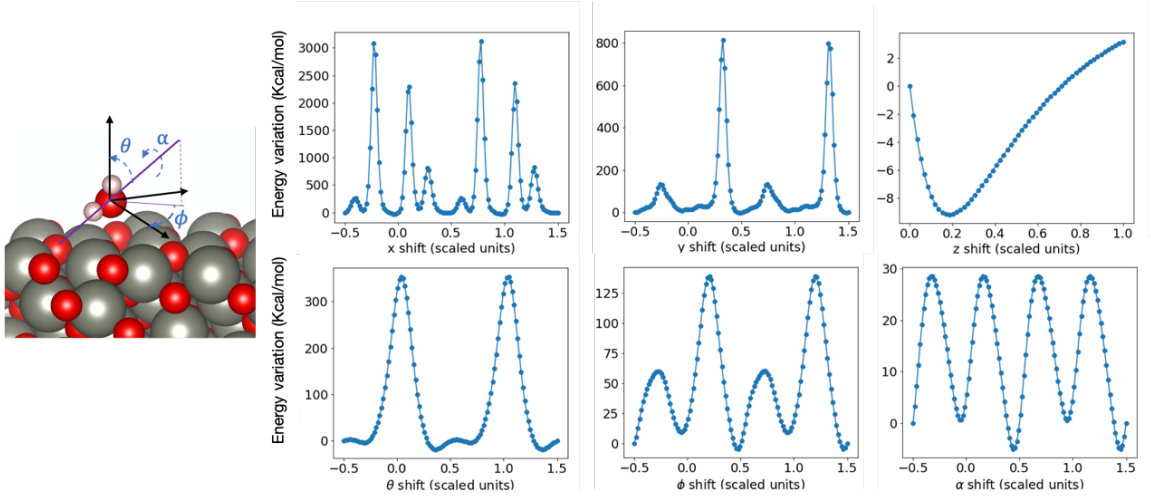

Figure 6.10, left) atomic visualization of water molecule on ZnO $(11\bar{2}2)$ surface, depicting directions and angles used to shift and rotate the water molecule. Right) Plots of the energy variation found when moving the reference H_2O molecule along each of the six degrees of freedom.

In this process, any new points that were found to be too close to the existing points in the new set were discarded, and the process was repeated until there were 10 unique new points. The optimizer was constrained to stay within the search domain of the scaled translations and rotations. In plotting the distribution of the new points during the learning

process, it was observed that often the minimizer relaxed to the boundaries of the search domain. As an alternative approach that prevents the accumulation of new points on the domain boundaries, we randomly sample 2000 points, as from this select the 10 with the minimum value of the acquisition function. The performances of both approaches are shown in Figure 6.11.

Analysis of the optimized hyperparameters from both approaches shows that the regression puts significant weight in its interpolation on the z separation between points with little dependence on their x-y separation. A second kernel contributing to the covariance matrix is sensitive to correlations between the rotation angles and the spatial translation. Numerous kernel combinations were tested. It was found that the results were not sensitive to the choice of *RBF* or *Matern* kernel functions, and when adding any more than two kernel functions into the composite kernel, the additional flexibility in the kernel was redundant.

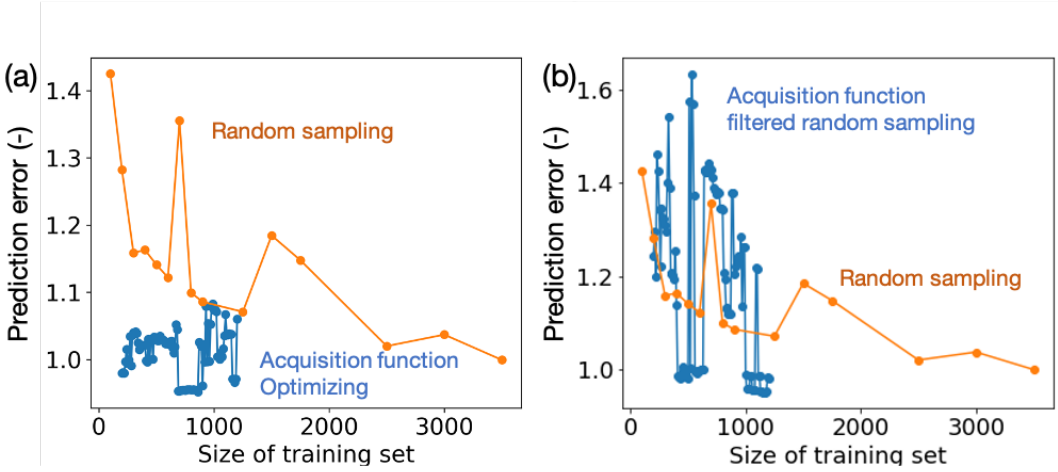

Figure 6.11, Plots of the convergence of the GP regression prediction vs number of data points used acquired in the iterative regression (blue) as compared to non-interactive regression using random sampling (gold). Plot (a) shows the results for iterative regressing with new points acquired using constrained optimization of the acquisition function. Plot (b) shows the results when new points are accrued though random sampling with the random samples filtered based on the acquisition function with only the best 0.5% added to the training data. It can be seen that optimization offers a significant improvement over the other method.

6.7 Case Study Three: Water on ZnO, Integrating Forces – non-interactive

6.7.1 Molecule Shifted Only in x

With molecular dynamics simulations and density functional theory, when one computes the energy of a molecular configuration, they obtain the forces on the atoms for free. Here, we test whether the gradient information obtained from forces can be used to accelerate the regression (reduce the number of regression points needed) and make more accurate predictions. One simple approach is to add two points for each configuration evaluated to the regression data, one corresponding to the true configuration, and a second phantom point slightly displaced along the force direction with an energy estimated from the force magnitude as discussed in the method and modeling section. Figure 6.12 illustrates true and auxiliary points displaced by *dx* generated for water molecule shifted along *x* via a regular

sampling approach. As illustrated, including the phantom points enables observing more information without a need for performing additional molecular simulations.

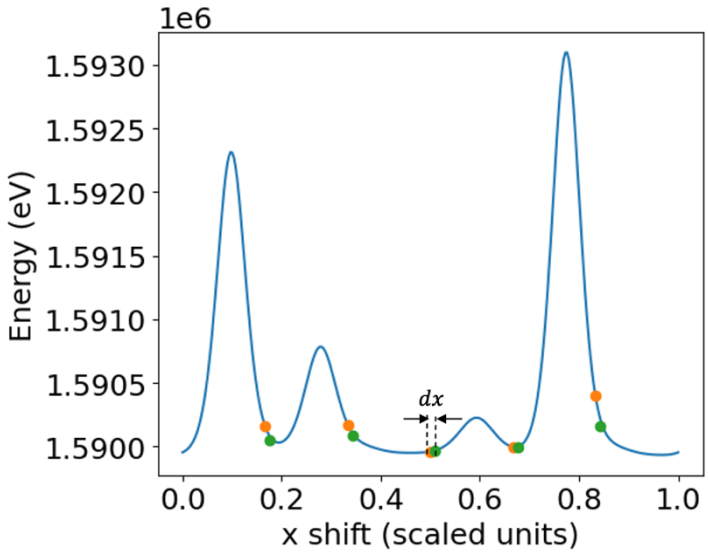

Figure 6.12, True (orange) and auxiliary points computed from forces (green) with a displacement of dx showing on the energy landscape of structures with molecules shifted in x.

In the non-interactive mode, addition of the force-computed points was found to improve the accuracy of the prediction. The benefit of adding the new points is even noticeable when we train GPs on a small train set. Figure 6.13 depicts the GP prediction for a train set of true points versus true + auxiliary points. The average uncertainty of prediction is improved by 50%, and the error is three times lower in the latter case.

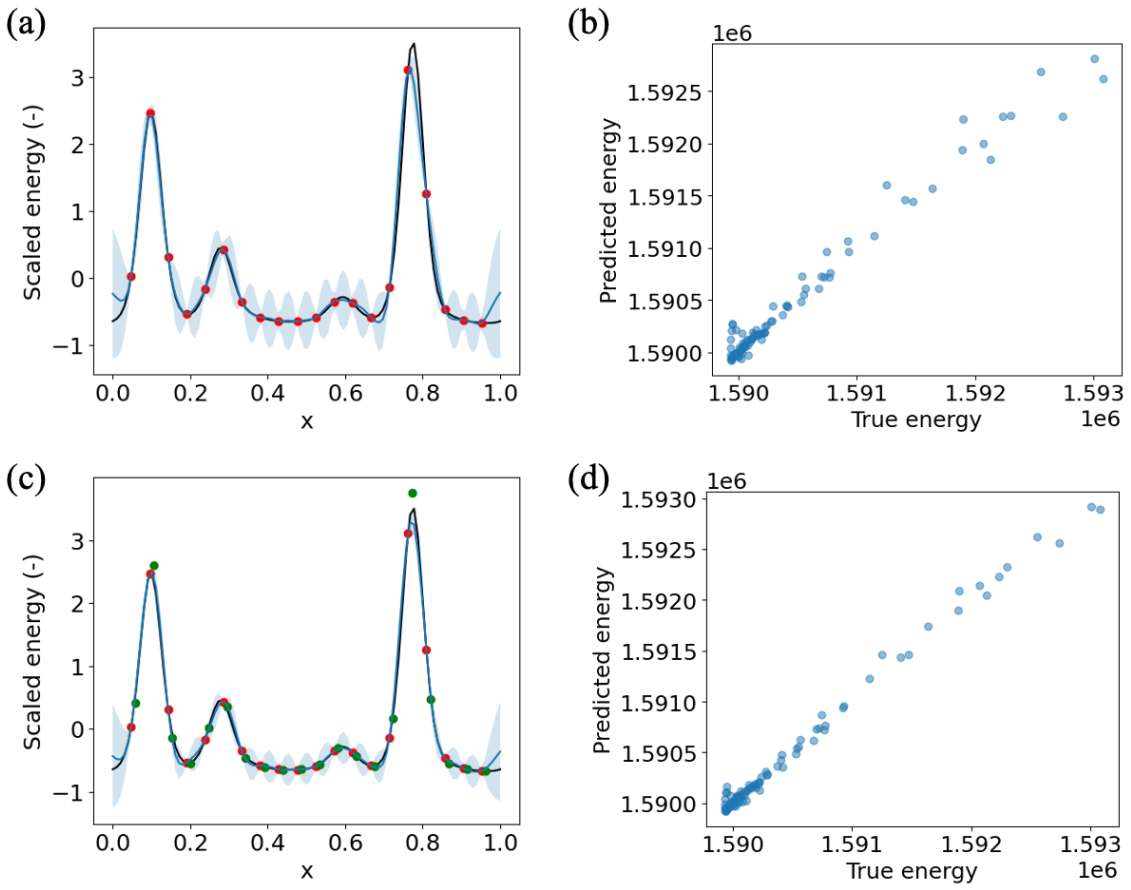

Figure 6.13, Plots of predictions using a single non-interactive GP acquisition for (a) and (b) using only true points, and (c) and (d) using both true points and the computed points using forces. In plots (a) and (c), black and blue lines show true and predicted potential energy surface for the validation set, respectively, red and green dots show the true and phantom points in the train set, and the light blue regions indicate the uncertainty of prediction. The initial training size is 20, the validation size is 100, and dx is 0.01.

When generating the phantom points, one important question is how to determine the value of dx. To answer this question, we evaluated the accuracy of the GP prediction using different values of dx ranging from 10^{-4} to 0.1 (scaled unit) in the 1D space. We then, repeated this evaluation for different $yshift$ values and plotted the average error of prediction as a function of dx value, as depicted in Figure 6.14. The minimum prediction error belongs to dx around 0.01. When using dx to compute the phantom points, we consider the linear regression and ignore the curvature in the energy surface. This approximation adds some

error to the system. The introduced error depends on the magnitude of dx. Larger dx values add more noise to the system; however, they also result in larger gradients. The optimum value of dx is achieved by a tradeoff between these two factors. In our model, we added the white kernel to the GP to treat the noisy data efficiently. This approach can handle the noise in data to some level. However, as illustrated in **Error! Reference source not found.**, one should still be careful not to use too large dx values, as they introduce a considerable noise to the system and lower the accuracy of the prediction.

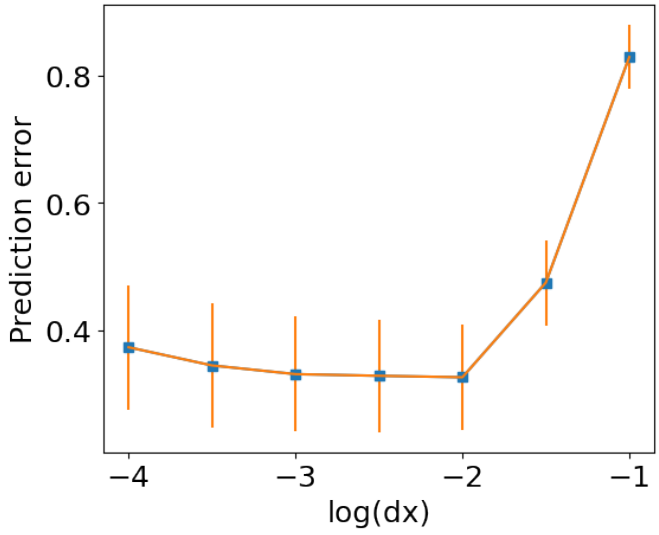

Figure 6.14, Plot of average prediction error vs. $log(dx)$ for a noninteractive GP acquisition performed on a 1D dataset of true and auxiliary points generated at a dx distance from the true points. Calculations were performed for 10 MD simulations and 10 phantom points shifted along the force direction in x, repeated for various $yshift$ values and averaged the prediction error.

To further evaluate the effect of dx choice on the model's performance, we plotted the prediction error as a function of the number of samples for datasets containing true and phantom points generated with various dx values (Figure 6.15). The results indicate that the regression procedure is accelerated, i.e., convergence is achieved with fewer number of MD simulations, as dx is increases from 0 (equivalent to no force) up to 0.01, while

increasing dx above 0.01 slows down the convergence and exacerbates the performance even compared to the no force case.

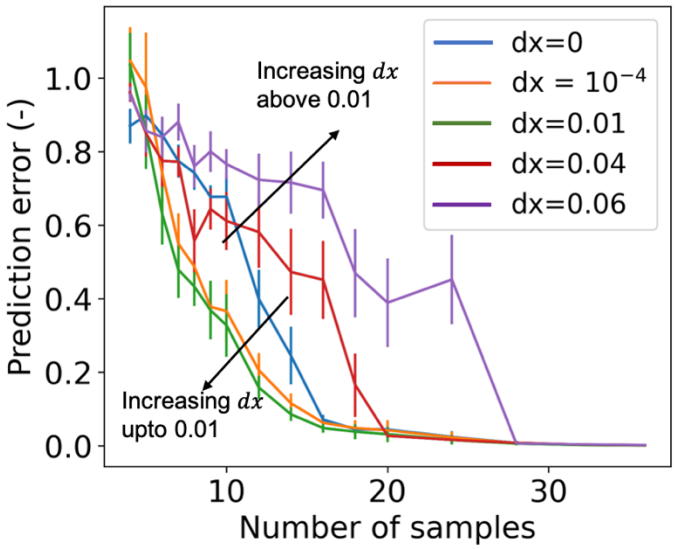

Figure 6.15, Plots of prediction error as a function of number of molecular simulations for a noninteractive GP acquisition performed on a 1D dataset of true and auxiliary points generated at a dx distance from the true points. Prediction was performed for various $yshift$ values, and the average prediction error was used for the plotting purpose.

It is important to note that the choice of dx may also depend on the nature of the dataset and therefore dx should be tuned according to the system. The value of dx should be selected in a way to improve sampling and enable observations of more distinct points across the space without adding a large noise to the system.

6.8 Case Study Three: Water on ZnO, Integrating Forces – Interactive

6.8.1 Molecule Shifted Only in x

In the previous section, we discussed how using forces to generate auxiliary data points helps us improve the performance and accuracy of GP prediction without need to perform additional molecular simulations. In this chapter, we seek to answer whether integrating

forces with the interactive Bayesian approach, results in faster and more accurate predictions. Here, in the iterative method, the added datapoints in each iteration includes set of new structures that minimize the acquisition function (and their energies computed using MD simulations) and the additional structures generated with a small displacement along the force direction. To provide a faster comparison, we reduced the configurational search space to 1D, shifting the molecule only in x .

Integrating forces in the interactive mode resulted in faster convergence and lower error of prediction. Figure 6.16 depicts the prediction results from interactive approach without and with using the auxiliary datapoints in each GP acquisition after 6 iterations, starting with 10 MD simulations and performing 10 additional molecular simulations in each iteration. One can see that the model that integrates forces outperforms the initial model. Reaching convergence after only 6 GP acquisition and performing only 60 MD simulations shows the significant robustness of the model. Although with increasing the search space dimension (to 6D), one would expect to achieve convergence slower, the performance of the model is yet expected to be better than other reported models, such as BOSS which is reported to reach convergence after 350 DFT simulations.

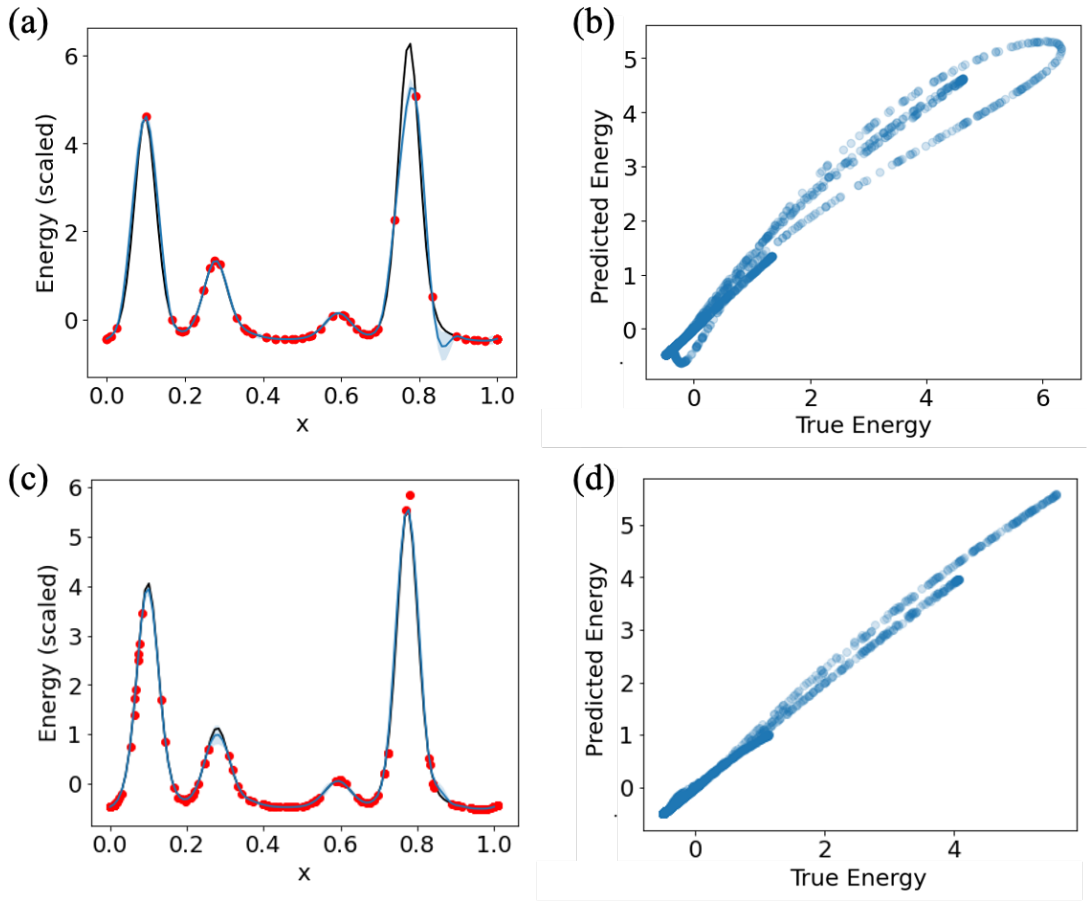

Figure 6.16, Plots of predictions using an interactive Bayesian inference for (a) and (b) implementing only true points, and (c) and (d) using true points and the displaced points in force direction to update the GP acquisition. In plots (a) and (c), black line and blue line represent true and predicted potential energy surface for the validation set, respectively, red dots indicate the train data, and the uncertainty of prediction is shown as light blue regions. The true prior set has 10 points, adding 10 additional points and their computed neighbors in each iteration.dx is 0.01. Plots show results after 6 Bayesian acquisitions.

To better evaluate the effect of integrating the forces into the Bayesian Inference approach, we calculated the error as a function of the number of molecular simulations (Figure 6.17). This confirms that adding information from forces to the model, accelerates convergence.

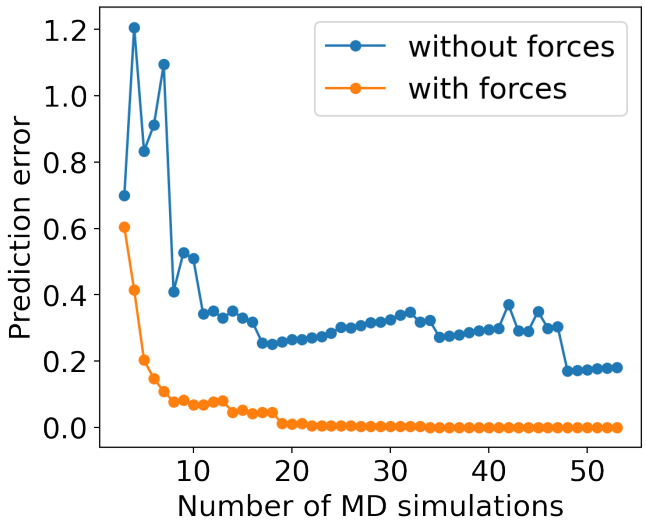

Figure 6.17, Plot of prediction error vs. number of molecular simulations for iterative methods with using only the true points (blue) and the true + auxiliary points (orange) to update the GP acquisition.

6.9 Conclusions

In this chapter, we presented an interactive method based on Bayesian Inference to search for the minimum energy structure in molecule-surface interactions. The input structures of MD simulations were filtered through minimizing the GP acquisition function to increase chances of generating new information in each acquisition, accelerating the process of finding the minimum energy structure. An innovation introduced in this project is integrating forces data with the Bayesian approach to make more accurate predictions using lower number of simulations (at no additional computational cost). This method was found to significantly speed up the Bayesian inference.

Further improvements of GP robustness can be made by more efficient sampling using periodic images of the structures, as well as trying other GP kernels and initial setups for the hyperparameters.

7. Structure-Property Relations in TiO_2 Photocatalytic Micro-reactors

7.1 Overview

This chapter reports the development of a Monte Carlo-based Ray Tracing model, named Light Capture, that simulates light-matter interactions in a microfluidic water-treatment reactor. The developed model is used to explore the operational behavior of a novel TiO_2 micropillars array being developed by our experimentalist collaborators that could provide a low-pressure and low-temperature system for decontaminating recycled wastewater in long-duration space missions.

The goal of this study is to understand the impact of micropillar geometry on the interplay of processes in the reactor and the resulting scaling of the reactor's overall photocatalytic performance. The aim is to create a model that can provide mechanistic understanding of the observed experimental trends, and to thereby generate guiding principles for reactor optimization. In section 7.4, the LightCapture model is used to find the effect of pillars' radius on light absorption efficiency. Further, the LightCapture model is coupled with a Lattice Boltzmann model [24], to simulate water flow around the pillars. Finally, the finite element method was used to model waste mass transfer as the overall efficiency of the reactors. In section 7.5, I report the effect of pillars' height on their photoabsorption efficiency using the LightCapture model.

7.2 Background and Related Works

Titanium dioxide (TiO_2) is the most widely used material for photocatalytic degradation of organic compounds – with the purpose of removing pollutants from water – due to its high catalytic activity, long-term stability against photo-corrosion and chemical corrosion, and low cost [186]–[188]. The most common phases of TiO2 include rutile and anatase with tetragonal structures and brookite with an orthorhombic structure. Among these phases, anatase has been found to have the highest photocatalytic activity because of its relatively high electron mobility [187], [189]. Anatase with its wide bandgap of 3.2 eV is only photocatalytically active under ultraviolet (UV) irradiation [187], [190], [191]. For terrestrial applications this is problematic and has driven much research on enhancing the light capture and quantum efficiency of anatase based photocatalysts. In space however, free from the shielding of the earth's atmosphere, the abundance of solar UV makes anatase TiO2 an attractive photocatalytic material.

TiO2's mechanism for water purification is through the generation of highly reactive hydroxyl radicals at the catalyst's surface. Absorption of UV light generates photoexcited electron-hole pairs in the TiO2 that can diffuse to the free surface where they take part in oxidation and reduction reactions. The holes can react with water to dissociate it into its components, hydrogen (H^+) and hydroxyl radicals ($OH^\bullet$). The generated $OH^\bullet$ radicals can be used for the degradation of organic pollutants in water [186]. As the photocatalytic reactions happen at the surface of the photocatalyst, their efficiency is controlled by the fundamental surface properties such as morphology and particle size of the photocatalytic material [192], [193]. Reducing the size of TiO2 provides a higher surface area for reduction

and oxidation reactions [189]. Among different morphologies, pillars and rods are favorable over particles due to their higher surface to volume ratio which provides a higher density of active sites for surface reactions as well as a higher interfacial charge carrier transfer rate. A higher length to width ratio of pillars also provides a direct pathway for the generated charge carriers to move freely through the length of the crystal, reducing the probability of electron-hole recombination [194].

TiO2 oxidized micropillars are synthesized by our experimentalist collaborators, Dr. Rao's team at *UC Riverside*, with the purpose of purifying wastewater in outer space. The photocatalytic microreactor is composed of a dense array of micropillars (10 μm radius, 40 μm pitch), each consisting of a titanium core with 1 μm thick nano-porous titanium dioxide (NPT) coating. The micropillar arrays are first defined using a novel micromachining technique that enables realization of micro to nano-scale device features with vertical sidewalls and high aspect ratios in bulk titanium substrates [195]–[197]. The NPT is then grown conformally from the surface of the titanium pillars via immersion in a heated hydrogen peroxide solution, followed by annealing to crystallize the NPT to anatase [198]. A UV-transmissive glass substrate is then attached to the upper surface of the reactor to seal the device. During device operation, a UV lamp is used for illumination, and a programmable syringe pump is used to control flow rate, and thus, residence time within the reactor. Error! R eference source not found. shows a schematic representation of the wastewater recycling procedure using TiO2 photocatalysts, from structure design – illustrated by the SEM image of TiO2 micropillars – to the photocatalytic oxidation and reduction, and the following contaminant degradation reactions.

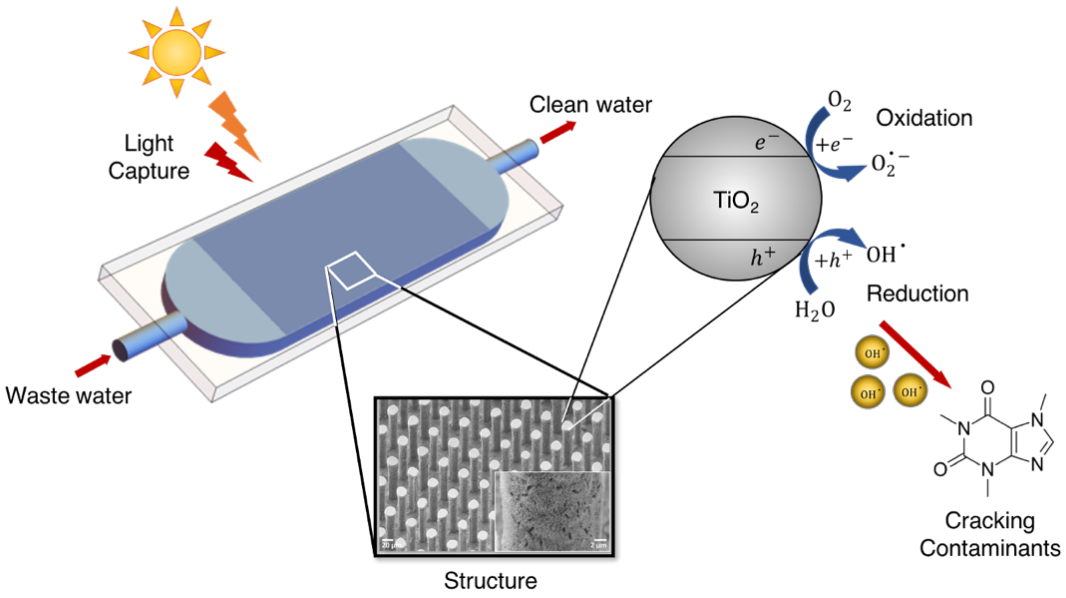

Figure 7.1, a schematic representation of the wastewater treatment process using TiO2 micropillars, from materials' synthesis and SEM image of fabricated array of pillars to oxidation & reduction reactions under light, and contaminant degradation.

7.3 Model Description

LightCapture is a Monte Carlo ray tracing model, which simulates light interactions at micropillars' surface. In this model, a random ray of light is followed from where it enters the reactor until it is absorbed by pillar, ground, or water or reflected out of the reactor. The system is composed of a periodic array of pillars. Therefore, to reduce the computation time, a model containing one quarter of a pillar in a box was considered for this study. To identify the hit points, intersections with the pillar's surface and walls of the imaginary simulation box are modeled by considering two angles, θ and φ. θ is the angle between the 2D projection of the ray and the horizontal axis, and φ is the angle between the ray and the vertical axis in 3D, illustrated in Figure 7.2, (a). A random ray is defined as a ray with a random start point and angle. The boundary condition is defined as the θ limits between

corners of the simulation box and endpoints of the pillar quarter (Figure 7.2, (b)). Figure 7.2, (c) shows a simple schematic of micropillars in the reactor. R is the pillar radius and L is the distance from the center of a pillar to the middle of the box, which is equivalent to half of the array's pitch. The model accounts for the reflectivity of the surface. It also accounts for both diffusive and specular reflections. Therefore, the results depend on the surface material and roughness as well as its geometry. In the results sections, to focus on the effect of geometry on light absorption and rule out the effect of other variables, we considered specific values of reflectivity, and all reflections were assumed to be diffusive so that the direction of an outgoing ray after reflection was random.

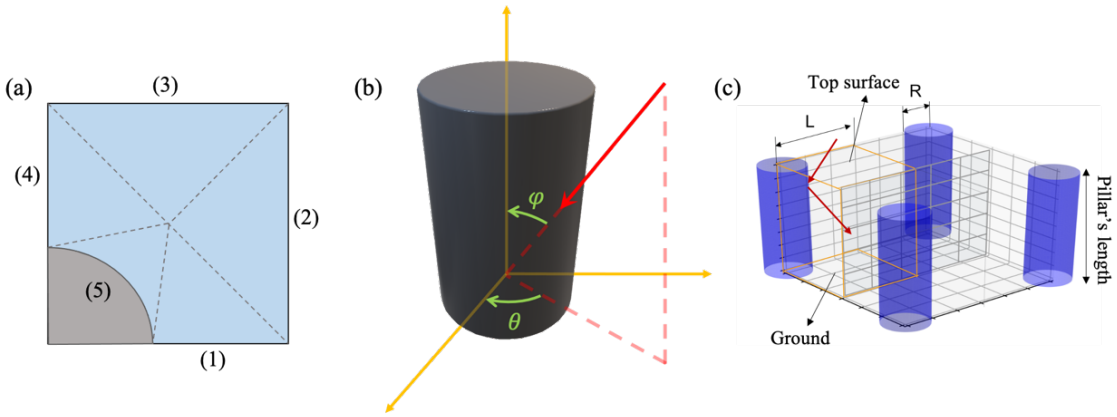

Figure 7.2, A schematic of (a) 2-dimensional simulation box with walls numbered and boundaries for angles set as dashed lines, (b) a ray hitting a pillar and $\boldsymbol{\theta}$ and $\boldsymbol{\varphi}$ angles, and (c) an array of pillars, Orange box shows the simulation model, R is the pillar radius, and L is the distance from center of pillar to the middle of pillar-to-pillar distance.

The model is composed of three main functions. The first function follows a ray path and determines where it hits the pillar or a wall. The second function runs the first function multiple times to account for the periodic boundary. Through this, the ray is either absorbed by the pillar or ground, or it is reflected and carries on bouncing in between surfaces until it gets absorbed by the pillar, ground, or water. The ray can also leave the reactor from the

top open surface. If the ray does not get absorbed after a certain number of simulations, we assume that it is lost. Using the third function, simulations are performed on tens of thousands of rays to construct the probability distribution of light capture, using multivariate Gaussian distributions, and to ensure good statistical averaging. The light capture model is a Python based program which has been made publicly available via a GitHub repository referenced here [199].

7.4 Optimization of Pillar's Radius

The first part of this chapter reports the results of using the LightCapture model to find out how the pillar's radius affects the light absorption efficiency. In addition, we present the results of coupling the LightCapture model with a Lattice Boltzmann flow model [24], [200], [201] to analyze the overall contaminant removal and water purification efficiency. A schematic of how these models are couples is illustrated in Figure 7.3.

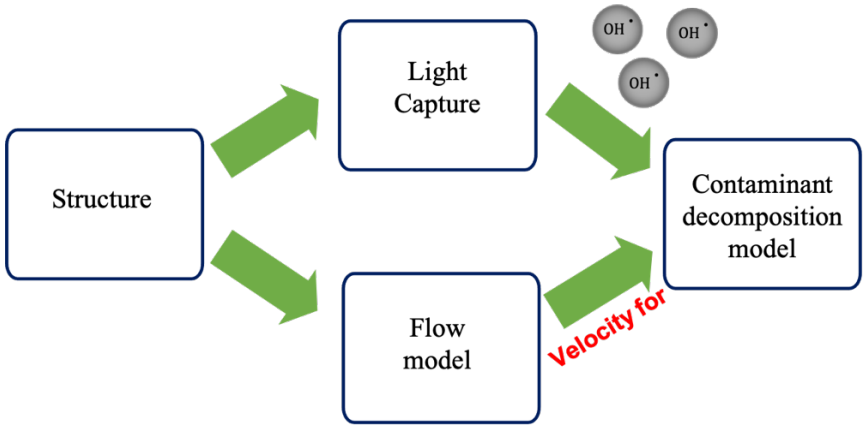

Figure 7.3, a visual explanation of the relation between the models used to predict the effect of pillar's radius on overall photocatalytic performance. The LightCapture model is used to model light absorption by pillars which affect the number of generated hydroxyls. The velocity of flow is found via the LBM flow model [24], [200], [201]. The results of the two models are used to evaluate the contaminant decomposition around the pillars.

7.4.1 LightCapture Results

The correlation between the amount of captured light and pillar's radius was found for pillars with reflectivity 0 and 0.5. the light capture distribution was computed for pillars with different radii and fixed L. The relative intensity of absorbed light is defined as the ratio of absorbed to incoming rays (I_p/I_{in}) and was obtained through multiplying the relative area (A_{water}/A_{pillar}) by the probability distribution of light absorption.

Figure 7.4, (a) and (d) depict the 2D polar plots of relative intensity of captured light on the surface of pillars with reflectivity 0 and 0.5, respectively. Figure 7.4, (b) and (e) show the mean probability distribution of absorbed rays vs. the position of hit points on the length of pillars with reflectivity 0 and 0.5, respectively. Figure 7.4, (c) and (f) depict the relative intensity of absorbed light at different points through the length of pillars with reflectivity 0 and 0.5, respectively. The mean probability distribution vs. height of hit points plots for all values of R have a maximum below – but close to the surface – suggesting that the maximum light absorption occurs somewhere below and not at the surface of the pillars. The mean probability distribution at maximum increases as the pillar's radius becomes larger. On the other hand, the available area for light transmission decreases as the surface area of the pillar increases. The interplay of these two factors results in a higher intensity of captured light for pillars with smaller radius. As a result, the polar plot surface becomes smaller (Figure 7.4, (a) and (d)), and the intensity peak value gets lower (Figure 7.4, (c) and (f)) as the radius of pillar increases.

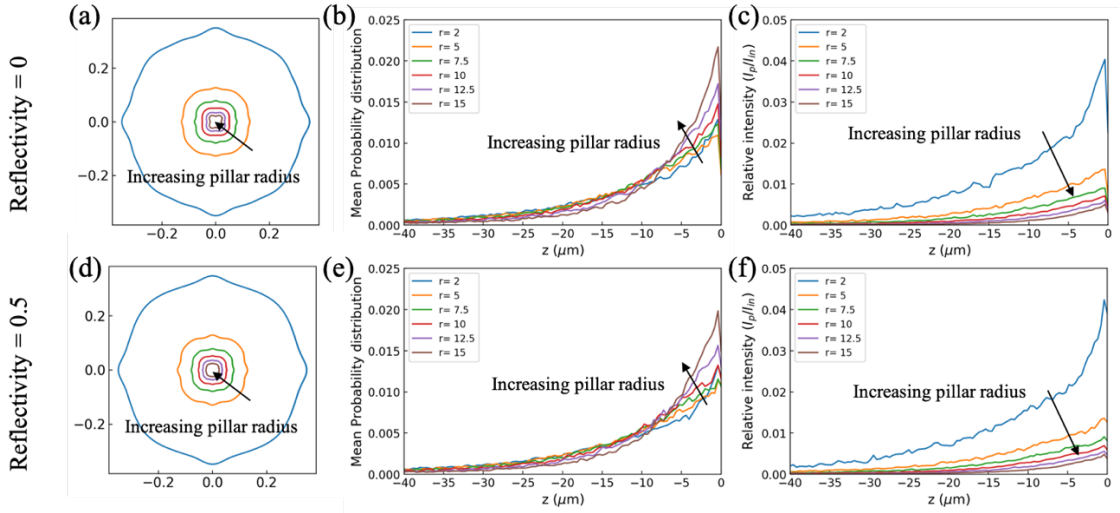

Figure 7.4, Intensity distribution of captured light on a pillar. In all plots, the data is sequential in radius along the arrows drawn on the plot for pillars of radii 2, 5, 7.5, 10, 12.5 $\boldsymbol{\mu m}$. Plots (a, c, and e) are computed with reflectivity of 0, and (b, d, and f) with reflectivity of 0.5. Polar plots (a and b) show the angular distributions of light capture intensity. Plots (c–f) show the axial distribution of light capture, (c and d) the probability that any ray is incident on a pillar at a given height, and (e and f) the intensity of light captured at a given height.

7.4.2 Coupling LightCapture with a Lattice Boltzmann Model

The fluid flow in between the pillars was simulated using a two-dimensional (2D) fluid flow model presented in Refs. [24], [200], [201]. In this model, the flow of water through the pillar arrays is modelled using the Shan and Chen (SC) type Lattice Boltzmann method (LBM) [202], which allows efficient treatment of fluid-solid boundaries. In SC LBM, fluid flow is modelled by solving for kinetic-theory rooted fluid density distribution in scheme-dependent number of lattice flow directions,

$$f(x + e_a\,\Delta t, t + \Delta t) = f(x,t) - \Omega(x,t) \tag{7.1}$$

here, $f(x,t)$ is the density distribution at position x and time t, e_a is a tensor of discrete velocities associated with each lattice flow direction, and $\Omega(x,t)$ is the collision term. The

macroscopic variables, velocity components and fluid density, are computed directly from the density distribution.

The flow of water through the micropillar reactor was modelled as a 2D problem with periodic boundaries on all sides. The flow was steady-state, laminar, and driven by a body force acting as a conventional pressure drop. The simulations were performed with cells of pillars with different radii in a staggered arrangement and the results are shown in Figure 7.5. The body force acting on the fluid was tuned for each geometry to obtain the same average residence time of the water in a single cell of the reactor with different pillar radii. In the motivating experimental work, the flows are controlled to give residence times ranging from 9.8 ms per cell to 78 ms per cell. In this flow regime the flow rate scales linearly with pressure drop, and the flow field is self-similar across the range of flow rates modelled. In arrays of wide pillars, the reduced volume of water means that the average water velocity is lower than in a thin pillar array with the same residence time. However, despite this, the increased drag from the additional surface area of the wide pillars requires a larger pressure drop to drive the flow, as is shown in Figure 7.5, (a).

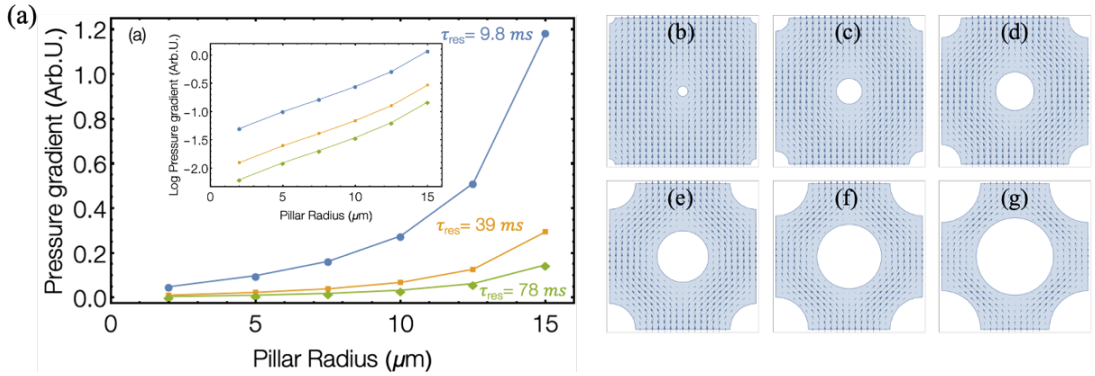

Figure 7.5, (a) shows the pressure drop required to drive water flow through different pillar arrays at a fixed residence time. Panels (b–g) show the velocity field of the water in the arrays of 2, 5, 7.5, 10, 12.5 and 15 μm pillars, respectively.

7.4.3 Contaminant Decomposition and Overall Performance

The contaminant in the water is decomposed by hydroxyl radicals produced at the surface of the TiO_2 pillars. Although this reaction happens in the fluid, the hydroxyl radicals are extremely short lived and so we can treat this as if the decomposition of contaminant molecules happens only at the surface of the pillars. The decomposition of contaminants is typically a multistep process, often producing intermediate reaction products that also react with hydroxyl radicals and can interfere with the reaction process by fouling the surface of the photocatalyst. To obtain a first understanding of the geometric scaling of the reactor we ignore this complexity. We treat the decomposition as a single step reaction with a rate that is first order in the concentration of hydroxyl and contaminant. The diffusion and decomposition of contaminant are modelled by solving the diffusion-advection equation for the contaminant field in a single cell of the micropillar reactor as shown in Figure 7.6. We solve the steady state equation in 2D:

$$0 = D\nabla^2 c(x,y) - \vec{v}(x,y) \cdot \nabla c(x,y) \tag{7.2}$$

where $c(x,y)$ is the concentration of contaminant, D is the diffusion coefficient of the contaminant in water, and $\vec{v}(x,y)$ is the velocity field of the flowing water that is obtained from the LBM simulations. We use the value of $D = 1.5 \times 10^{-5}$cm^2/s, the diffusion coefficient of caffeine in water (a particularly recalcitrant water contaminant) [203]. The concentration distribution of solute is solved in a single cell of the micropillar array with the boundary conditions shown in Figure 7.6. The rate of decomposition of contaminant at the pillar surfaces is given by,

$$\dot{c}_{\text{pil}} = k\, p(x,y)\, c(x,y) = D\hat{n} \cdot \nabla c(x,y) \tag{7.3}$$

where $p(x,y)$ is the light capture distribution plotted in Figure 7.4 (a). The reaction rate, k contains a number of unknown quantities: the intensity of illumination, the quantum efficiency of absorbed photons producing surface hydroxyl radicals, and the probability that an emitted hydroxyl will interact with a contaminant molecule. Because of these unknowns the reaction k coefficient is left as a floating parameter. We know from the experimental results that with a residence time of 78 ms per cell one can obtain decomposition of ~90 % of contaminant in a reactor of 512 cells. We have used this result to tune k to a value of 0.02 s^{-1} , to obtain a similar order of magnitude to the decomposition rate, and then verified that in this regime the performance varies linearly with k.

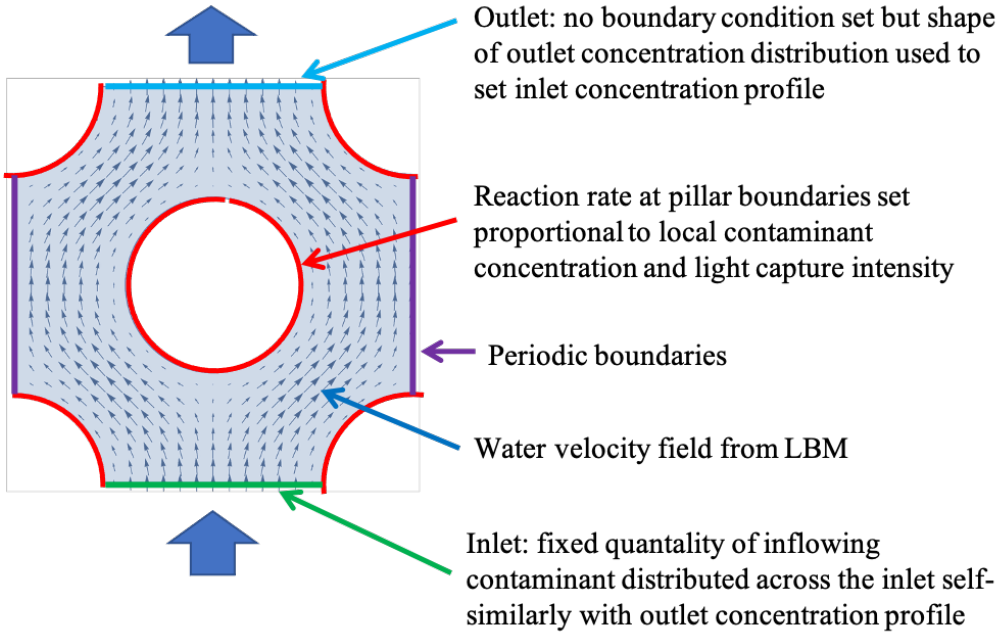

Figure 7.6, The solution domain and boundary conditions for the contaminant decomposition model.

Figure 7.7 shows the contaminant distribution in one face centered cell of the pillar array under conditions of a slow and fast flow (long and short residence time). These show the concentration gradient driving diffusion to the pillars where decomposition occurs, and the overall reduction in the concentration from inlet to outlet of the cell. As the pillars become larger there is more surface area available for reaction, but the rate of reaction at those surfaces goes down because of the reduction in intensity of captured light. However, the larger pillars have narrower constrictions that the water must flow through leading to shorter diffusion distances to deliver contaminant to the pillars. This is a significant qualitative difference in the contaminant diffusion field at high and low flow rates: At low flow speeds, Figure 7.7, *top* there is a large diffusive flux of contaminant striking the pillars head on where the flow impinges upon it. This leaves a depleted region in the concentration distribution down stream of each pillar. At high flow rate, Figure 7.7, *bottom,* this depleted

region in each pillar's wake extends all the way to the next pillar so the pillars shadow one another. In this high flow regime, the flux of contaminant to the pillars is mostly lateral to the flow direction.

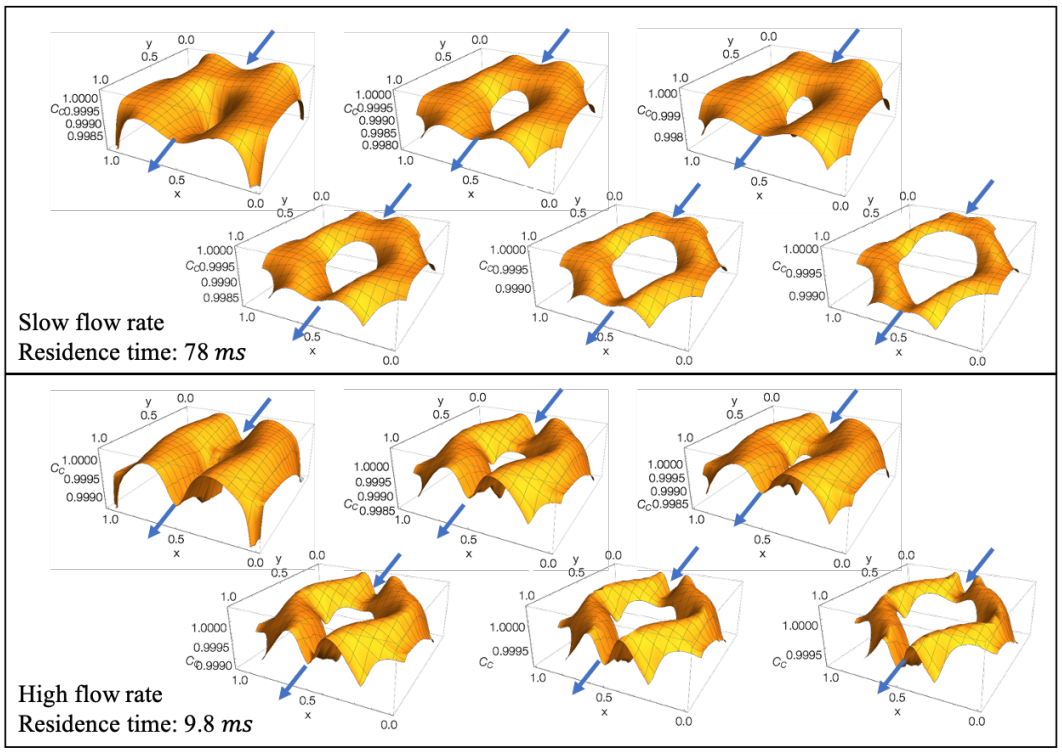

Figure 7.7, Steady state contaminant distribution profiles in the reactor. Top) (a–f) with long residence time, and bottom) with short residence time

Computing the fraction of the inlet contaminant concentration that is decomposed in each cell provides a useful metric of performance, and enables quantitative comparison of the different geometries, as plotted in Figure 7.8, (a) vs the pillar, and (b) vs the width of the narrowest constriction in the pillar array. Also plotted are the performance vs driving pressure gradient and the rate of contaminant removal (the performance scaled by residence time). These results show that longer residencies allow for more contaminant decomposition. They also show that at higher flow rates there is a general trend for improved

performance with larger pillars; however, at slow flow rates there is a maximum in the performance for pillars between 7.5 and 10 μm in radius. Given the increased pressure requirements needed to drive flow through wide pillared arrays, this suggests that experimental optimization should focus on thinner pillars with high flow rate and recycle the fluid through the reactor multiple times.

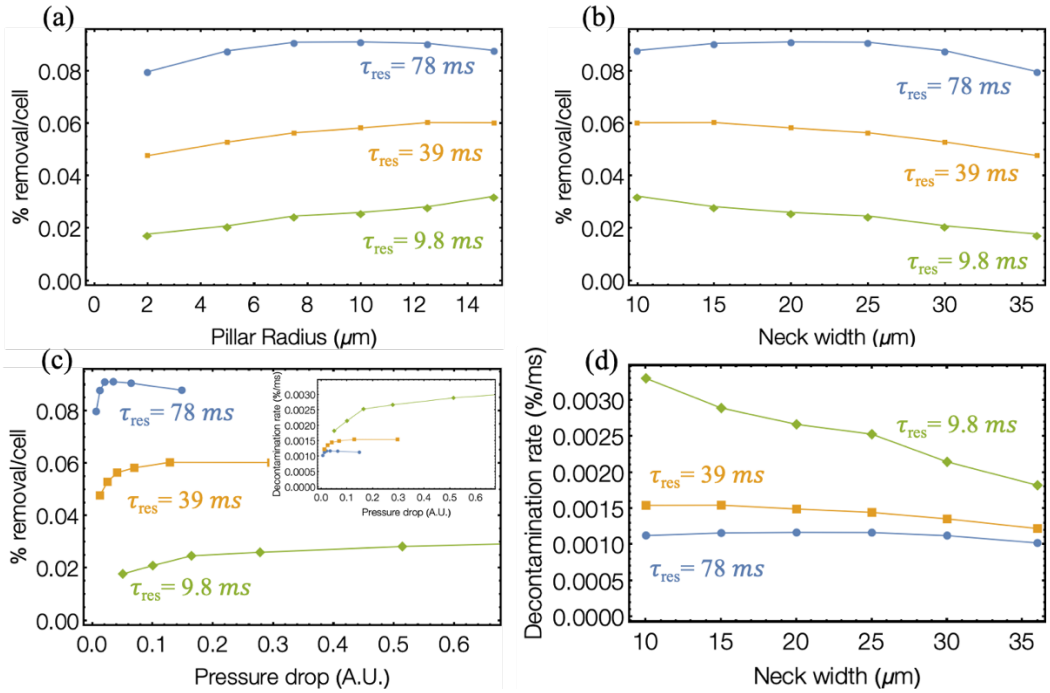

Figure 7.8, Plots of the photocatalytic performance of the micropillar arrays at fixed residence time as a function of (a) pillar radius, and (b) the width of the narrowest constriction in the water channel (c) performance vs driving pressure gradient, and (d) shows the rate of contaminant remove.

7.5 Optimization of Pillar's height: LightCapture Results

The second part of results focuses on elucidating the relationship between pillar's height and photoabsorption efficiency. For this part, we chose a system of pillars with radii 7.5 μm, and $L = 14.14\ \mu m$ to match the experimental setup.

Figure 7.9 shows the light capture distribution plots within a unit cell from the microreactor with a pillar pitch to diameter ratio of 1.9 and reflectivity values of 0, 0.2, 0.3, and 0.5. The plots show, for varying pillar height, the total proportion of light entering a reactor that is absorbed by the pillars, absorbed by the reactor floor, or reflected back from the top surface and lost. The values of pillar height in Figure 7.9, were normalized by the spacing between the diagonally adjacent pillars $W = \sqrt{2}L - 2r$ where L is the vertical pitch between adjacent pillars, and r is the radius of the pillar. It can be seen in Figure 7.9, that for all values of reflectivity, for pillars taller than five times their diagonal distance (here, >24.5 μm), critical height, there is little further change in the total fraction of light captured by the reactor. As expected, higher reflectivity results in increasing the ratio of rays that are leaving the reactor, but it does not cause a noticeable change in the critical pillar's height.

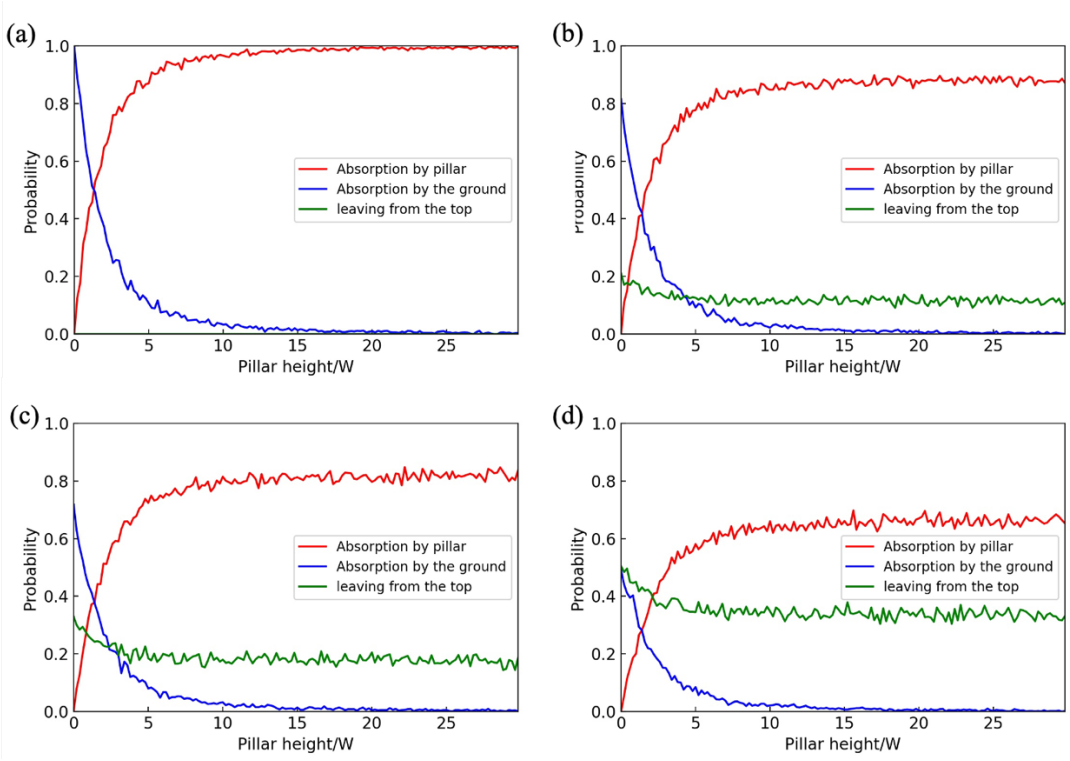

Figure 7.9, Probability that the photons get absorbed by the pillars surface or the ground or leave the reactor from the top surface plotted through pillars height normalized over the spacing between the diagonally adjacent pillars ($W = \sqrt{2}\,L - 2r$) for a surface with Ref. (a) 0, (b) 0.2, (c) 0.3, and (d) 0.5.

Figure 7.10 illustrates the heatmaps of simulated light absorption distribution on the ground and pillar for devices with depths of 50, 100, and 150 μm, respectively. For this, the TiO2 surfaces of the reactor were modeled with a reflectivity of 0.2 to match that measured experimentally. Figure 7.10 (e) and (f) show that most of the light is captured by the upper portion of the pillars. This would make the region near the top of the pillars highly photoactive while the surface near the foot of the pillar and the reactor floor are much less active. Thus, one would not expect a significant improvement in reactor performance for pillars taller than 50 μm. This is in perfect alignment with the results of the experimental study done by Dr. Rao's team. The results indicate that it may be beneficial to try other

geometries such as micro-cones instead of micropillars to achieve more uniformly distributed light capture and higher reactivity through the reactor. Varying pillar pitch and sidewall angle may also contribute to improving light capture. Figure 7.10 (a – c) show that absorption on the ground is low and largely similar at each depth except for the micropillars with length 50 μm which displays a slightly higher probability of absorption and better photon uniformity.

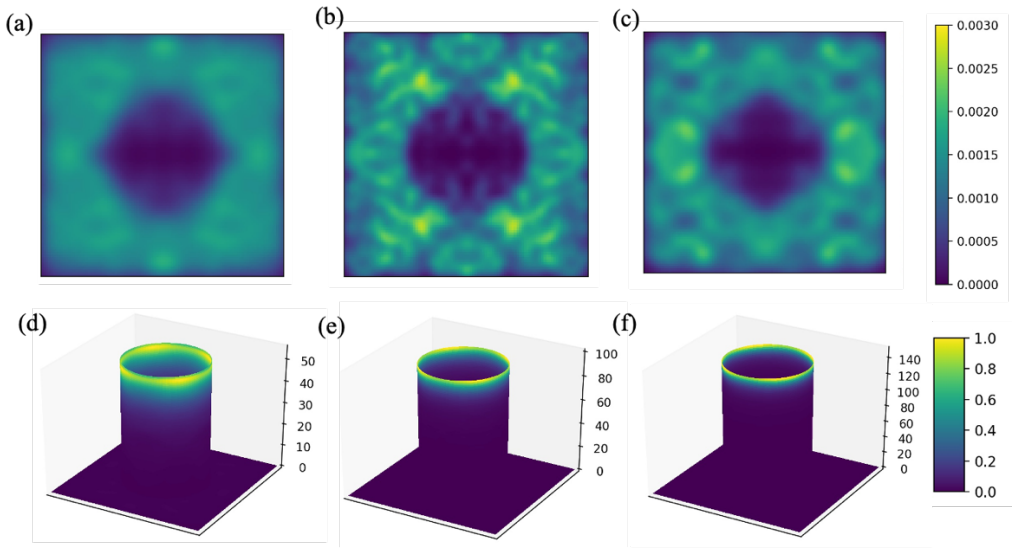

Figure 7.10, (b - d) light capture probability distribution heatmaps for absorption on top) (b - d) the ground, and bottom) (e – f) the walls of pillars with depths of 50, 100, and 150 μm, respectively. To enable reliable comparison, same range of distribution was used to visualize light capture on the ground and pillars of all reactors. Simulations were performed for 100,000 rays.

7.6 Model Evaluation

The model evaluation was done by calculating the uncertainty of the predictions and comparing the results of simulations against experimental tests.

To evaluate the uncertainty, we performed the simulations for N rays, with N varying in a range. Each time, we performed the simulations n times, and picked a fixed point p to evaluate the uncertainty at it. We computed the uncertainty U at point p as the standard error

of the average intensity $\bar{I}(p)$ from the n simulations divided by the mean of the n simulations. U is,

$$U = \frac{1}{\bar{I}(p)\sqrt{n}} \sqrt{\frac{\sum_i \left(I_i(p) - \bar{I}(p)\right)^2}{n-1}} \tag{7.4}$$

With $\bar{I}(p)$ defined as,

$$\bar{I}(p) = \frac{1}{n}\sum_i I_i(p) \tag{7.5}$$

Figure 7.11 shows the uncertainty plotted for simulations with different number of rays, using $n = 10$ and with p on the ground at the center of the four neighboring pillars. Accordingly, performing simulations with 20,000 rays resulted in an uncertainty value below 10%.

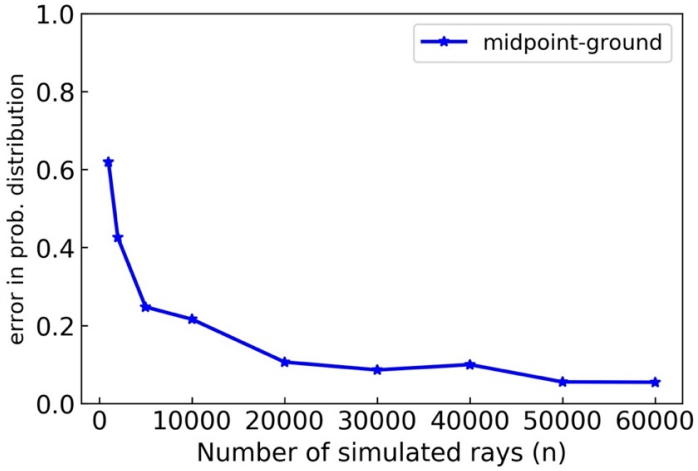

Figure 7.11, Average uncertainty plotted against the number of simulated rays for a point at the center of the four neighboring pillars on the ground. Each simulation was performed 10 times to obtain a good statistical averaging.

Moreover, the predictions from the LightCapture model were compared with the operational tests from experimental tests on the reactor. The predictions were found to be in perfect agreement with the experimental results.

7.7 Conclusions

The first chapter of this thesis focused on developing a numerical model that optimizes the design of microfluidic reactors for waste-water treatment in outer-space. The motivation for this model was to help an experimental group optimize the design of their reactor, which contains an array of Titanium dioxide (TiO2) micropillars.

The results of simulations indicate that as the radius of the pillars in the reactor are increased, the surface area of catalytic materials goes up, but the intensity of captured light goes down more quickly, and one thus, might expect that the performance would be worse with wide pillars; however moderate improvement in performance is observed due to the reduction in the diffusion path to the pillar surface. Increasing the flow rate of the

contaminated water produces a qualitatively different diffusion field, and although the contaminant decomposition per cell goes down the total rate of contaminant decomposition is increased.

For comparison of pillars height, the results show that the optimum light capture is obtained for pillars with height ~5 times their diagonal distance, above which changing the pillar's height does not increase the photoabsorption efficiency. This suggests that varying pillars' pitch and sidewall angle may contribute to improving light capture.

As opposed to trial and test methods, reliable mathematical models can help experimentalists make smarter and faster plans and save enormous amount of time and money. Although this project was targeted towards predicting the photoabsorption efficiency of TiO2 micropillars, the presented model can be readily expanded to apply to a wide range of other ray tracing problems such as rendering images and studies of heat transfer in porous materials.

8. Conclusions

In this thesis, we reported novel first-principles studies and computational methods to accelerate discovery of wide bandgap semiconductors.

We presented first-principles studies to elucidate structure-property relations in various WBGs. We presented DFT calculations for predicting the growth mechanism of ZnO nano-pyramidal structures for energy storage. The presented method can be implemented to engineer other structures away-from-equilibrium. We also reported on our comprehensive studies to facilitate surface transfer doping in diamond. This involved *ab initio* studies of 2D layers as interfacial layer to preserve the p-type bulk-like conductivity at the surface of diamond, as well as modeling amorphous V_2O_5 slabs as an acceptor layer for doping diamond. These predictions provide valuable insight for the semiconductor device community.

Furthermore, we presented a novel AI-based approach to accelerate computational studies of surface-molecule interactions. This method provides an active learning framework based on integrating Gaussian Processes and molecular dynamics simulations to accelerate the search for the minimum energy structure. We demonstrate that through integrating the forces, we can achieve nearly 2× faster performance. This method can also be used for accelerating structure optimization in quantum simulations to significantly reduce the time and cost of simulations. Finally, in the last chapter, we presented a novel ray tracing method based on Monte Carlo simulations to simulate light absorption in microfluidic water recycling reactors. The model was successfully applied to provide guidance for geometry

optimization in reactors designed by our collaborators for wastewater recycling during space missions.

Bibliography

[1] T. Lim, P. S. Mirabedini, K. Jung, P. A. Greaney, and A. A. Martinez-Morales, "High-index crystal plane of ZnO nanopyramidal structures : Stabilization , growth , and improved photocatalytic performance," *Appl. Surf. Sci.*, no. February, p. 147326, 2020, doi: 10.1016/j.apsusc.2020.147326.

[2] P. S. Mirabedini *et al.*, "Structural and electronic properties of 2D (graphene, hBN)/H-terminated diamond (100) heterostructures," *Appl. Phys. Lett.*, vol. 117, p. 121901, 2020, doi: 10.1063/5.0020620.

[3] P. S. Mirabedini, A. Truszkowska, D. Z. Ashby, M. P. Rao, and P. A. Greaney, "Coupled Light Capture and Lattice Boltzmann Model of TiO 2 Micropillar Array for Water Purification," *MRS Adv.*, vol. 467, p. 2689, 2019, doi: 10.1557/adv.201.

[4] "Sources of Greenhouse Gas Emissions." https://www.epa.gov/ghgemissions/sources-greenhouse-gas-emissions.

[5] "Offshore windfarms 'can provide more electricity than the world needs,'" *The Gaurdian*. https://www.theguardian.com/environment/2019/oct/24/offshore-windfarms-can-provide-more-electricity-than-the-world-needs.

[6] J. Isberg *et al.*, "High carrier mobility in single-crystal plasma-deposited diamond," *Science (80-.).*, vol. 297, no. 5587, pp. 1670–1672, 2002, doi: 10.1126/science.1074374.

[7] M. Kasu, K. Ueda, H. Kageshima, and Y. Yamauchi, "Gate interfacial layer in hydrogen-terminated diamond field-effect transistors," *Diam. Relat. Mater.*, vol. 17, no. 4–5, pp. 741–744, 2008, doi: 10.1016/j.diamond.2007.12.022.

[8] E. Kohn and A. Denisenko, "Concepts for diamond electronics," *Thin Solid Films*, vol. 515, no. 10, pp. 4333–4339, 2007, doi: 10.1016/j.tsf.2006.07.179.

[9] F. Maier, M. Riedel, B. Mantel, J. Ristein, and L. Ley, "Origin of surface conductivity in diamond," *Phys. Rev. Lett.*, vol. 85, no. 16, pp. 3472–3475, 2000, doi: 10.1103/PhysRevLett.85.3472.

[10] P. Strobel, M. Riedel, J. Ristein, and L. Ley, "Surface transfer doping of diamond," *Nature*, vol. 430, no. 6998, pp. 439–441, 2004, doi: 10.1038/nature02751.

[11] M. T. Edmonds *et al.*, "Surface band bending and electron affinity as a function of hole accumulation density in surface conducting diamond," *Appl. Phys. Lett.*, vol. 98, no. 10, p. 102101, 2011, doi: 10.1063/1.3561760.

[12] J. Ristein, "Surface transfer doping of semiconductors," *Science (80-.).*, vol. 313, pp. 1057–1059, 2006, doi: 10.1126/science.1127589.

[13] Z. Yin, M. Tordjman, Y. Lee, A. Vardi, R. Kalish, and J. A. Del Alamo, "Enhanced transport in transistor by tuning transition-metal oxide electronic states interfaced with diamond," *Sci. Adv.*, vol. 4, no. 9, p. eaau0480, 2018, doi: 10.1126/sciadv.aau0480.

[14] M. Kasu *et al.*, "Influence of epitaxy on the surface conduction of diamond film," *Diam. Relat. Mater.*, vol. 13, no. 2, pp. 226–232, 2004, doi: 10.1016/j.diamond.2003.10.025.

[15] Y. Yang, F. A. Koeck, M. Dutta, X. Wang, S. Chowdhury, and R. J. Nemanich, "Al2O3 dielectric layers on H-terminated diamond: Controlling surface conductivity," *J. Appl. Phys.*, vol. 122, no. 15, p. 155304, 2017, doi: 10.1063/1.4985808.

[16] S. A. O. Russell *et al.*, "Surface transfer doping of diamond by MoO3: A combined spectroscopic and Hall measurement study," *Appl. Phys. Lett.*, vol. 103, no. 20, p. 202112, 2013, doi: 10.1063/1.4832455.

[17] K. G. Crawford *et al.*, "Enhanced surface transfer doping of diamond by V2O5 with improved thermal stability," *Appl. Phys. Lett.*, vol. 108, no. 4, p. 042103, 2016, doi: 10.1063/1.4940749.

[18] K. G. Crawford *et al.*, "Diamond Field-Effect Transistors With V_2O_5-Induced Transfer Doping: Scaling to 50-nm Gate Length," *IEEE Trans. Electron Devices*, vol. 67, no. 6, pp. 2270–2275, 2020, doi: 10.1109/TED.2020.2989736.

[19] Y. Sasama *et al.*, "High-mobility diamond field effect transistor with a monocrystalline h-BN gate

dielectric," *APL Mater.*, vol. 6, no. 11, p. 111105, 2018, doi: 10.1063/1.5055812.
[20] H. Kawarada *et al.*, "Durability-enhanced two-dimensional hole gas of C-H diamond surface for complementary power inverter applications," *Sci. Rep.*, vol. 7, p. 42368, 2017, doi: 10.1038/srep42368.
[21] L. Colalongo, M. Valdinoci, G. Baccarani, P. Migliorato, G. Tallarida, and C. Reita, "NUMERICAL ANALYSIS OF POLY-TFTs UNDER OFF CONDITIONS," *Solid. State. Electron.*, vol. 41, no. 4, pp. 627–633, 1997, [Online]. Available: https://www.sciencedirect.com/science/article/pii/S0038110196002018.
[22] A. Alnuaimi, K. Islam, and A. Nayfeh, "Reduction of interface traps at the amorphous-silicon/crystalline-silicon interface by hydrogen and nitrogen annealing," *Sol. Energy*, vol. 98, pp. 236–240, 2013, doi: 10.1016/j.solener.2013.10.003.
[23] A. Yusuf, C. Garlisi, and G. Palmisano, "Overview on micro fl uidic reactors in photocatalysis : Applications of graphene derivatives," *Catal. Today*, vol. 315, pp. 79–92, 2018, [Online]. Available: https://doi.org/10.1016/j.cattod.2018.05.041.
[24] A. Truszkowska, P. A. Greaney, and G. Jovanovic, "Multiscale lattice Boltzmann modeling of two-phase flow and retention times in micro-patterned fluidic devices," *Comput. Chem. Eng.*, vol. 95, pp. 249–259, 2016.
[25] R. LeSar, *Introduction to Computational Materials Science: Fundementals to Applications*. Cambridge: Cambridge university press, 2016.
[26] E. Schrodinger, "An Undulatory Theory of the Mechanics of Atoms and Molecules," *Phys. Rev.*, vol. 28, p. 1049, 1926.
[27] P. Hohenberg and W. Kohn, "Inhomogeneous Electron Gas," *Phys. Rev.*, vol. 136, p. B864, 1964, [Online]. Available: https://journals.aps.org/pr/abstract/10.1103/PhysRev.136.B864.
[28] M. Ernzerhof and G. E. Scuseria, "Assessment of the Perdew – Burke – Ernzerhof," *J. Chem. Phys.*, vol. 110, p. 5029, 1999.
[29] H. J. C. Berendsen, J. P. M. Postma, W. F. van Gunsteren, A. DiNola, and J. R. Haak, "Molecular dynamics with coupling to an external bath," *J. Chem. Phys.*, vol. 81, p. 3684, 1984.
[30] G. R. Hofmann, "Who invented Ray Tracing?," *Vis. Comput.*, vol. 6, pp. 120–124, 1990.
[31] T. Whitted, "An Improved Illumination Model for Shaded Display," vol. 23, pp. 343–349, 1980.
[32] A. M. Johansen, *International Encyclopedia of Education (Third Edition)*. Elsevier Science, 2010.
[33] J.E. Gentle, *International Encyclopedia of Education (Third Edition)*. 2010.
[34] N. Metropolis, "The beginning of the Monte Carlo Method," *Los Alamos Sci. (1987 Spec. Issue Dedic. to Stanislaw Ulam)*, pp. 125–130, 1987.
[35] L. Athanasiou, D. Fotiadis, and L. Michalis, *Atherosclerotic Plaque Characterization Methods Based on Coronary Imaging*. Academic Press, 2017.
[36] S. K. Haldar, *Mineral exploration: principles and applications*. Elsevier, 2018.
[37] K. P. Murphy, *Probabilistic Machine Learning: An Introduction*. MIT Press, 2021.
[38] C. Tang, J. S. Spencer, and A. S. Barnard, "Activity of ZnO polar surfaces : an insight from surface energies," *Phys. Chem. Chem. Phys.*, vol. 16, pp. 22139–22144, 2014, doi: 10.1039/c4cp03221g.
[39] A. Phys, "Graphene / GaN diodes for ultraviolet and visible photodetectors," vol. 073103, no. August 2014, 2016, doi: 10.1063/1.4893609.
[40] A. Sirelkhatim, S. Mahmud, and A. Seeni, "Review on Zinc Oxide Nanoparticles : Antibacterial Activity and Toxicity Mechanism," *Nano-Micro Lett.*, vol. 7, pp. 219–242, 2015, doi: 10.1007/s40820-015-0040-x.
[41] W. I. Park, D. H. Kim, S.-W. Jung, and G.-C. Yi, "Metalorganic vapor-phase epitaxial growth of vertically well-aligned ZnO nanorods," *Appl. Phys. Lett.*, vol. 80, p. 4232, 2002, doi: 10.1063/1.1482800.
[42] Y. Ma, Y. Dai, M. Guo, and B. Huang, "Graphene-diamond interface: Gap opening and electronic spin injection," *Phys. Rev. B*, vol. 85, no. 23, p. 235448, 2012, doi: 10.1103/PhysRevB.85.235448.
[43] L. Yan, A. Uddin, and H. Wang, "ZnO Tetrapods: Synthesis and Application in Solar Cells," *Nanomater. Nanotechnol.*, vol. 5, p. 19, 2015, doi: 10.5772/60939.
[44] C. Peng, J. Guo, W. Yang, C. Shi, and M. Liu, "Synthesis of three-dimensional fl ower-like hierarchical ZnO nanostructure and its enhanced acetone gas sensing properties," *J. Alloys Compd.*,

vol. 654, pp. 371–378, 2016.
[45] C. Jin, J. Li, S. Han, J. Wang, and Q. Sun, “A durable , superhydrophobic , superoleophobic and corrosion-resistant coating with rose-like ZnO nanoflowers on a bamboo surface,” *Appl. Surf. Sci.*, vol. 320, pp. 322–327, 2014, doi: 10.1016/j.apsusc.2014.09.065.
[46] X. Wang, G. Liu, G. Qing, and H. Cheng, “Stable photocatalytic hydrogen evolution from water over ZnO – CdS core – shell nanorods,” *Int. J. Hydrogen Energy*, vol. 35, pp. 8199–8205, 2010, doi: 10.1016/j.ijhydene.2009.12.091.
[47] S. B. A. Hamid, S. J. Teh, and C. W. Lai, “Photocatalytic Water Oxidation on ZnO : A Review,” *catalysts*, vol. 7, p. 93, 2017, doi: 10.3390/catal7030093.
[48] D. Tang, L. F. Allard, A. Boley, D. J. Smith, and J. Liu, “Structure and morphology of polar and semi-polar pyramidal surfaces coating wurtzite ZnO micro-wires,” *J. Mater. Sci.*, vol. 48, pp. 3857–3862, May 2013, doi: 10.1007/s10853-013-7187-y.
[49] E. Debroye *et al.*, “Facet-Dependent Photoreduction on Single ZnO Crystals,” *J. Phys. Chem. Lett.*, vol. 8, pp. 340–346, Jan. 2017, doi: 10.1021/acs.jpclett.6b02577.
[50] K.-P. Wu, W.-F. Ma, C.-X. Sun, C.-Z. Chen, L.-Y. Ling, and Z.-G. Wang, “Band offset and electronic properties at semipolar plane AlN($1\bar{1}01$)/diamond heterointerface,” *Chinese Phys. B*, vol. 27, no. 5, p. 058101, May 2018, doi: 10.1088/1674-1056/27/5/058101.
[51] J. Zhang, Y. Zhang, K. Tse, B. Deng, H. Xu, and J. Zhu, “New approaches for calculating absolute surface energies of wurtzite (0001)/(000): A study of ZnO and GaN,” *J. appl. phys.*, vol. 119, p. 205302, 2016, doi: 10.1063/1.4952395.
[52] J. G. Lee, *Computational materials science : an introduction*. Boca Raton, FL: Taylor & Francis, 2012.
[53] B. Meyer and D. Marx, “Density-functional study of the structure and stability of ZnO surfaces,” *Phys. Rev. B*, vol. 67, no. 3, p. 035403, Jan. 2003, doi: 10.1103/PhysRevB.67.035403.
[54] G. Kresse and J. Furthmüller, “Efficiency of ab-initio total energy calculations for metals and semiconductors using a plane-wave basis set,” *Comput. Mater. Sci.*, vol. 6, no. 1, pp. 15–50, 1996.
[55] G. Kresse and J. Furthmüller, “Efficient iterative schemes for ab initio total-energy calculations using a plane-wave basis set,” *Phys. Rev. B*, vol. 54, pp. 11169–11186, 1996, doi: 10.1103/PhysRevB.54.11169.
[56] G. Kresse and J. Hafner, “Ab initio molecular dynamics for liquid metals,” *Phys. Rev. B*, vol. 47, no. 1, pp. 558–561, 1993, doi: 10.1103/PhysRevB.47.558.
[57] G. Kresse and J. Hafner, “Ab initio molecular-dynamics simulation of the liquid-metal–amorphous-semiconductor transition in germanium,” *Phys. Rev. B*, vol. 49, no. 20, pp. 14251–14269, May 1994, doi: 10.1103/PhysRevB.49.14251.
[58] J. P. Perdew, K. Burke, and M. Ernzerhof, “Generalized gradient approximation made simple,” *Phys. Rev. Lett.*, vol. 77, no. 18, pp. 3865–3868, 1996, doi: 10.1103/PhysRevLett.77.3865.
[59] J. P. Perdew, K. Burke, and M. Ernzerhof, “Generalized Gradient Approximation Made Simple [Phys. Rev. Lett. 77, 3865 (1996)],” *Phys. Rev. Lett.*, vol. 78, no. 7, pp. 1396–1396, Feb. 1997, doi: 10.1103/PhysRevLett.78.1396.
[60] G. Kresse and D. Joubert, “From ultrasoft pseudopotentials to the projector augmented-wave method,” *Phys. Rev. B*, vol. 59, no. 3, pp. 1758–1775, 1999.
[61] P. E. Blöchl, “Projector augmented-wave method,” *Phys. Rev. B*, vol. 50, no. 24, pp. 17953–17979, Dec. 1994, doi: 10.1103/PhysRevB.50.17953.
[62] W. H. Press, S. A. Teukolsky, W. T. Vetterling, and B. P. Flannery, *Numerical Recipes 3rd Edition: The Art of Scientific Computing*, 3rd ed. Cambridge university press, 2007.
[63] Y. Sasama *et al.*, “Quantum oscillations in diamond field-effect transistors with a h -BN gate dielectric,” *Phys. Rev. Mater.*, vol. 3, no. 12, p. 121601, 2019, doi: 10.1103/PhysRevMaterials.3.121601.
[64] G. Daligou and J. Pernot, “2D hole gas mobility at diamond/insulator interface,” *Appl. Phys. Lett.*, vol. 116, no. 16, p. 162105, 2020, doi: 10.1063/5.0002768.
[65] S. J. Sque, R. Jones, and P. R. Briddon, “Structure, electronics, and interaction of hydrogen and oxygen on diamond surfaces,” *Phys. Rev. B*, vol. 73, p. 085313, 2006, doi: 10.1103/PhysRevB.73.085313.

[66] J. MacQueen, “Some methods for classification and analysis of multivariate observations,” *Proc. fifth Berkeley Symp. Math. Stat. Probab.*, vol. 1, no. 14, pp. 281–297, 1967.
[67] G. Kresse and J. Hafner, “Ab initio molecular-dynamics simulation of the liquid-metalamorphous-semiconductor transition in germanium,” *Phys. Rev. B*, vol. 49, no. 20, pp. 14251–14269, 1994, doi: 10.1103/PhysRevB.49.14251.
[68] S. Grimme, “Semiemperical GGA-Type Density Functional Constructed with a Long-Range Dispersion Correction,” *J. Comput. Chem.*, vol. 32, pp. 174–182, 2012, doi: 10.1002/jcc.
[69] A. V. Krukau, O. A. Vydrov, A. F. Izmaylov, and G. E. Scuseria, “Influence of the exchange screening parameter on the performance of screened hybrid functionals,” *J. Chem. Phys.*, vol. 125, no. 22, p. 224106, 2006, doi: 10.1063/1.2404663.
[70] S. Grimme, J. Antony, S. Ehrlich, and H. Krieg, “parametrization of density functional dispersion correction (DFT-D) for the 94 elements H-Pu,” *J. Chem. Phys.*, vol. 132, p. 154104, 2010, doi: 10.1063/1.3382344.
[71] S. Grimme, S. Ehrlich, and L. Goerigk, “Effect of the Damping Function in Dispersion Corrected Density Functional Theory,” *J. Comp. Chem.*, vol. 32, p. 1456, 2011, doi: 10.1002/jcc.
[72] S. Steiner, S. Khmelevskyi, M. Marsmann, and G. Kresse, “Calculation of the magnetic anisotropy with projected-augmented-wave methodology and the case study of disordered Fe 1 − x Co x alloys,” *Phys. Rev. B*, vol. 93, p. 224425, 2016, doi: 10.1103/PhysRevB.93.224425.
[73] W. Tang, E. Sanville, and G. Henkelman, “A grid-based Bader analysis algorithm without lattice bias,” *J. Phys. Condens. Matter*, vol. 21, no. 8, p. 084204, 2009, doi: 10.1088/0953-8984/21/8/084204.
[74] Z. Ren *et al.*, “High temperature (300 °c) ALD grown Al2O3 on hydrogen terminated diamond: Band offset and electrical properties of the MOSFETs,” *Appl. Phys. Lett.*, vol. 116, no. 1, p. 013503, 2020, doi: 10.1063/1.5126359.
[75] C. Wild, R. Kohl, N. Herres, W. Muller-Sebert, and P. Koidl, “Oriented CVD diamond films: twin formation, structure and morphology,” *Diam. Relat. Mater.*, vol. 3, pp. 373–381, 1994.
[76] J. van der Weide, Z. Zhang, P. K. Baumann, M. G. Wensell, J. Bernholc, and R. J. Nemanich, “Negative electron affinity effects on the diamond (100) surface,” *Phys. Rev. B*, vol. 50, no. 8, pp. 5803–5806, 1994.
[77] S. Lu, Y. Wang, H. Liu, M. Miao, and Y. Ma, “Self-assembled ultrathin nanotubes on diamond (100) surface,” *Nat. Commun.*, vol. 5, no. 100, p. 3666, 2014, doi: 10.1038/ncomms4666.
[78] H. Gomez, M. N. Groves, and M. R. Neupane, “Study of the structural phase transition in diamond (100) & (111) surfaces,” *Carbon Trends*, vol. 3, p. 100033, 2021, doi: 10.1016/j.cartre.2021.100033.
[79] T. Frauenheim, U. Stephan, P. Blaudeck, and D. Porezag, “Stability, reconstruction, and electronic properties of diamond (100) and (111) surfaces,” *Phys. Rev. B*, vol. 48, no. 24, p. 18189, 1993.
[80] G. Bogdan, M. Nesladek, J. D’Haen, K. Haenen, and M. D’Olieslaeger, “Freestanding (100) homoepitaxial CVD diamond,” *Diam. Relat. Mater.*, vol. 15, pp. 508–512, 2006, doi: 10.1016/j.diamond.2005.10.059.
[81] W. Hu, Z. Li, and J. Yang, “Diamond as an inert substrate of graphene,” *J. Chem. Phys.*, vol. 138, no. 5, p. 054701, 2013, doi: 10.1063/1.4789420.
[82] S. Zhao and K. Larsson, “Diamond & Related Materials First principle study of the attachment of graphene onto non-doped and doped diamond (111),” *Diam. Relat. Mater.*, vol. 66, pp. 52–60, 2016.
[83] C. D. Mendoza, N. S. Figueroa, M. E. H. Maia da Costa, and F. L. Freire Jr, “OPEN CVD graphene / Ge interface : morphological and electronic characterization of ripples,” *Sci. Rep.*, vol. 9, p. 12547, 2019, doi: 10.1038/s41598-019-48998-1.
[84] F. Varchon, P. Mallet, J. Y. Veuillen, and L. Magaud, “Ripples in epitaxial graphene on the Si-terminated SiC(0001) surface,” *Phys. Rev. B*, vol. 77, no. 23, p. 235412, 2008, doi: 10.1103/PhysRevB.77.235412.
[85] D. Selli, I. Baburin, S. Leoni, Z. Zhu, D. Tománek, and G. Seifert, “Theoretical investigation of the electronic structure and quantum transport in the graphene-C(111) diamond surface system,” *J. Phys. Condens. Matter*, vol. 25, no. 43, p. 435302, 2013, doi: 10.1088/0953-8984/25/43/435302.

[86] G. Wan, S. Panditharatne, N. A. Fox, and M. Cattelan, “Graphene-diamond junction photoemission microscopy and electronic interactions Graphene-diamond junction photoemission microscopy and electronic interactions,” *Nano Express*, vol. 1, p. 020011, 2020.
[87] T. Yamada, T. Masuzawa, H. Mimura, and K. Okano, “Field emission spectroscopy measurements of graphene / n-type diamond heterojunction Field emission spectroscopy measurements of graphene / n-type diamond heterojunction,” *Appl. Phys. Lett.*, vol. 114, p. 231601, 2019, doi: 10.1063/1.5094365.
[88] J. C. Phys, W. Hu, Z. Li, and J. Yang, “Diamond as an inert substrate of graphene,” *J. Chem. Phys.*, vol. 138, p. 054701, 2013, doi: 10.1063/1.4789420.
[89] H. Tan *et al.*, “Doping Graphene Transistors Using Vertical Stacked Monolayer WS 2 Heterostructures Grown by Chemical Vapor Deposition,” *ACS Appl. Mater. Interfaces*, vol. 8, no. 3, pp. 1644–1652, 2016, doi: 10.1021/acsami.5b08295.
[90] F. Lin *et al.*, “Graphene/GaN diodes for ultraviolet and visible photodetectors,” *Appl. Phys. Lett.*, vol. 105, no. 7, p. 073103, 2014, doi: 10.1063/1.4893609.
[91] R. H. Miwa, T. M. Schmidt, W. L. Scopel, and A. Fazzio, “Doping of graphene adsorbed on the a-SiO2 surface,” *Appl. Phys. Lett.*, vol. 99, no. 16, p. 163108, 2011, doi: 10.1063/1.3653261.
[92] S. Kopylov, A. Tzalenchuk, S. Kubatkin, and V. I. Fal’Ko, “Charge transfer between epitaxial graphene and silicon carbide,” *Appl. Phys. Lett.*, vol. 97, no. 11, p. 112109, 2010, doi: 10.1063/1.3487782.
[93] U. Monteverde *et al.*, “Under pressure : Control of strain , phonons and bandgap opening in rippled graphene,” *Carbon N. Y.*, vol. 91, pp. 266–274, 2015.
[94] J. Zhang, K. P. Ong, and P. Wu, “The Influence of Out-of-Plane Deformation on the Band Gap of Graphene Nanoribbons,” *J. Phys. Chem. C*, vol. 114, pp. 12749–12753, 2010, doi: 10.1021/jp103195u.
[95] C. Park, L. Yang, Y. Son, M. L. Cohen, and S. G. Louie, “Anisotropic behaviours of massless Dirac fermions in graphene under periodic potentials,” *Nat. Phys.*, vol. 4, pp. 213–217, 2008, doi: 10.1038/nphys890.
[96] W. Bao *et al.*, “Controlled ripple texturing of suspended graphene and ultrathin graphite membranes,” *Nat. Nanotechnol.*, vol. 4, pp. 562–566, 2009, doi: 10.1038/nnano.2009.191.
[97] L. Huang, Q. Yue, J. Kang, Y. Li, and J. Li, “Tunable band gaps in graphene/GaN van der Waals heterostructures,” *J. Phys. Condens. Matter*, vol. 26, no. 29, p. 295304, 2014, doi: 10.1088/0953-8984/26/29/295304.
[98] M. A. L. Marques, J. Vidal, M. J. T. Oliveira, L. Reining, and S. Botti, “Density-based mixing parameter for hybrid functionals,” *Phys. Rev. B*, vol. 83, no. 3, p. 035119, 2011, doi: 10.1103/PhysRevB.83.035119.
[99] W. Chen and A. Pasquarello, “Band-edge levels in semiconductors and insulators: Hybrid density functional theory versus many-body perturbation theory,” *Phys. Rev. B*, vol. 86, no. 3, p. 035134, 2012, doi: 10.1103/PhysRevB.86.035134.
[100] J. Y. Tsao *et al.*, “Ultrawide-Bandgap Semiconductors: Research Opportunities and Challenges,” *Adv. Electron. Mater.*, vol. 4, no. 1, p. 1600501, 2018, doi: 10.1002/aelm.201600501.
[101] M. Sun, J. P. Chou, Q. Ren, Y. Zhao, J. Yu, and W. Tang, “Tunable Schottky barrier in van der Waals heterostructures of graphene and g-GaN,” *Appl. Phys. Lett.*, vol. 110, no. 17, p. 173105, 2017, doi: 10.1063/1.4982690.
[102] D. Tomer, S. Rajput, L. J. Hudy, C. H. Li, and L. Li, “Intrinsic inhomogeneity in barrier height at monolayer graphene/SiC Schottky junction,” *Appl. Phys. Lett.*, vol. 105, no. 2, p. 021607, 2014, doi: 10.1063/1.4890405.
[103] W. Schottky, “Zur Halbleitertheorie der Sperrschicht- und Spitzengleichrichter,” *Zeitschrift für Phys.*, vol. 113, pp. 367–414, 1939, doi: https://doi.org/10.1007/BF01340116.
[104] N. F. Mott, “The theory of crystal rectifiers,” *Proc. R. Soc. Lond. A.*, vol. 171, pp. 27–38, 1939, doi: https://doi.org/10.1098/rspa.1939.0051.
[105] M. R. Neupane, R. K. Lake, and R. Rahman, “Electronic states of Ge / Si nanocrystals with,” *J. Appl. Phys.*, vol. 112, p. 024326, 2012, doi: 10.1063/1.4739715.
[106] M. Sun, J. P. Chou, J. Yu, and W. Tang, “Electronic properties of blue phosphorene/graphene and

blue phosphorene/graphene-like gallium nitride heterostructures," *Phys. Chem. Chem. Phys.*, vol. 19, no. 26, pp. 17324–17330, 2017, doi: 10.1039/c7cp01852e.
[107] T. Olsen, S. Latini, F. Rasmussen, and K. S. Thygesen, "Simple Screened Hydrogen Model of Excitons in Two-Dimensional Materials," *Phys. Rev. Lett.*, vol. 116, p. 056401, 2016, doi: 10.1103/PhysRevLett.116.056401.
[108] E. V Calman, M. M. Fogler, L. V Butov, S. Hu, A. Mishchenko, and A. K. Geim, "Indirect excitons in van der Waals heterostructures at room temperature," *Nat. Commun.*, vol. 9, p. 1895, 2018, doi: 10.1038/s41467-018-04293-7.
[109] G. Wang *et al.*, "Colloquium : Excitons in atomically thin transition metal dichalcogenides," *Rev. Mod. Phys.*, vol. 90, no. 2, p. 21001, 2018, doi: 10.1103/RevModPhys.90.021001.
[110] M. Long, P. Wang, H. Fang, and W. Hu, "Progress , Challenges , and Opportunities for 2D Material Based Photodetectors," *Adv. Funct. Mater.*, vol. 29, p. 1803807, 2019, doi: 10.1002/adfm.201803807.
[111] A. Di Bartolomeo, "Emerging 2D Materials and Their Van Der Waals Heterostructures," *Nanomaterials*, vol. 10, p. 579, 2020.
[112] T. P. O'Regan *et al.*, "Structural and electrical analysis of epitaxial 2D/3D vertical heterojunctions of monolayer MoS2 on GaN," *Appl. Phys. Lett.*, vol. 111, p. 051602, 2017.
[113] D. Ruzmetov *et al.*, "Van der Waals interfaces in epitaxial vertical metal/2D/3D semiconductor heterojunctions of monolayer MoS2 and GaN," *2D Mater.*, vol. 5, no. 4, 2018, doi: 10.1088/2053-1583/aad1b7.
[114] A. Fasolino, J. H. Los, and M. I. Katsnelson, "Intrinsic ripples in graphene," *Nat. Mater.*, vol. 6, p. 858, 2007, doi: 10.1038/nmat2011.
[115] S. K. Singh, M. Neek-Amal, S. Costamagna, and F. M. Peeters, "Thermomechanical properties of a single hexagonal boron nitride sheet," *Phys. Rev. B*, vol. 87, p. 184106, 2013.
[116] S. Thomas, K. M. Ajith, and M. C. Valsakumar, "Effect of ripples on the finite temperature elastic properties of hexagonal boron nitride using strain-fluctuation method," *Superlattices Microstruct.*, vol. 111, pp. 360–372, 2017, doi: 10.1016/j.spmi.2017.06.051.
[117] A. Rossi, S. Piccinin, V. Pellegrini, S. de Gironcoli, and V. Tozzini, "Nano-Scale Corrugations in Graphene: A Density Functional Theory Study of Structure, Electronic Properties and Hydrogenation," *J. Phys. Chem. C*, vol. 119, pp. 7900–7910, 2015.
[118] V. Tozzini and V. Pellegrini, "Reversible Hydrogen Storage by Controlled Buckling of Graphene Layers," *J. Phys. Chem. C*, vol. 115, pp. 25523–25528, 2011.
[119] X. Gao *et al.*, "Regioselectivity control of graphene functionalization by ripples," *Phys. Chem. Chem. Phys.*, vol. 13, pp. 19449–19453, 2011.
[120] G. Gui, J. Zhong, and Z. Ma, "Electronic properties of rippled graphene," *J. Phys. Conf. Ser.*, vol. 402, p. 012004, 2012, doi: 10.1088/1742-6596/402/1/012004.
[121] M. Gmitra, S. Konschuh, C. Ertler, C. Ambrosch-Draxl, and J. Fabian, "Band-structure topologies of graphene : Spin-orbit coupling effects from first principles," *Phys. Rev. B*, vol. 80, p. 235412, 2009, doi: 10.1103/PhysRevB.80.235431.
[122] S. Konschuh, M. Gmitra, and J. Fabian, "Tight-binding theory of the spin-orbit coupling in graphene," *Phys. Rev. B*, no. 82, p. 245412, 2010, doi: 10.1103/PhysRevB.82.245412.
[123] C. Elias *et al.*, "Direct band-gap crossover in epitaxial monolayer boron nitride," *Nat. Commun.*, vol. 10, p. 2639, 2019, doi: 10.1038/s41467-019-10610-5.
[124] J. Wang, F. Ma, and M. Sun, "Graphene, hexagonal boron nitride, and their heterostructures: properties and applications," *RSC Adv.*, vol. 7, pp. 16801–16822, 2017, doi: 10.1039/c7ra00260b.
[125] P. S. Mirabedini *et al.*, "Structural and electronic properties of 2D," *Appl. Phys. Lett.*, vol. 117, p. 121901, 2020, doi: 10.1063/5.0020620.
[126] R. J. Nemanich *et al.*, "Electron emission properties of crystalline diamond and III-nitride surfaces," *Appl. Surf. Sci. 130–132*, no. 130, pp. 694–703, 1998.
[127] V. Wang, N. Xu, J.-C. Liu, G. Tang, and W.-T. Geng, "VASPKIT: A User-friendly Interface Facilitating High-throughput Computing and Analysis Using VASP Code," *arXiv Prepr. arXiv1908.08269*, 2019.
[128] C. J. Fall, N. Binggeli, and A. Baldereschi, "Deriving accurate work functions from thin-slab

calculations," *J. Phys. Condens. Matter*, vol. 11, no. 13, pp. 2689–2696, 1999, doi: 10.1088/0953-8984/11/13/006.
[129] J. Yang, M. Youssef, and B. Yildiz, "Predicting point defect equilibria across oxide hetero-interfaces: Model system of ZrO2/Cr2O3," *Phys. Chem. Chem. Phys.*, vol. 19, no. 5, pp. 3869–3883, 2017, doi: 10.1039/c6cp04997d.
[130] I. Borriello, G. Cantele, D. Ninno, G. Iadonisi, M. Cossi, and V. Barone, "Ab initio study of electron affinity variation induced by organic molecule adsorption on the silicon (001) surface," *Phys. Rev. B*, vol. 76, no. 3, p. 035430, 2007, doi: 10.1103/PhysRevB.76.035430.
[131] D. Qi, X. Gao, L. Wang, S. Chen, K. P. Loh, and A. T. S. Wee, "Tailoring the electron affinity and electron emission of diamond (100) 2 × 1 by surface functionalization using an organic semiconductor," *Chem. Mater.*, vol. 20, no. 21, pp. 6871–6879, 2008, doi: 10.1021/cm801752j.
[132] X. Yang *et al.*, "Epitaxial Combination of Two-Dimensional Hexagonal Boron Nitride with Single-Crystalline Diamond Substrate," *ACS Appl. Mater. Interfaces*, vol. 12, p. 46466−46475, 2020, doi: 10.1021/acsami.0c11883.
[133] M. Gong, Q. Wang, N. Gao, and H. Li, "Structural and electronic properties of nitrogen-terminated diamond (100) surfaces," *Diam. Relat. Mater.*, vol. 120, p. 108601, 2021.
[134] F. Maier, J. Ristein, and L. Ley, "Electron affinity of plasma-hydrogenated and chemically oxidized diamond „ 100 … surfaces," *Phys. Rev. B*, vol. 64, p. 165411, 2001, doi: 10.1103/PhysRevB.64.165411.
[135] M. M. Hassan and K. Larsson, "Effect of Surface Termination on Diamond (100) Surface Electrochemistry," *J. Phys. Chem. C*, vol. 118, no. 22995–23002, 2014.
[136] W. Shen, Y. Pan, S. Shen, H. Li, Y. Zhang, and G. Zhang, "Electron affinity of boron-terminated diamond (001) surfaces: a density functional theory study," *J. Mater. Chem. C*, vol. 7, pp. 9756–9765, 2019, doi: 10.1039/c9tc02517k.
[137] K. Larsson and Y. Tian, "Effect of surface termination on the reactivity of nano-sized diamond particle surfaces for bio applications," *Carbon N. Y.*, vol. 134, pp. 244–254, 2018, doi: 10.1016/j.carbon.2018.03.031.
[138] J. B. Cui, J. Ristein, and L. Ley, "Electron Affinity of the Bare and Hydrogen Covered Single Crystal Diamond (111) Surface," *Phys. Rev. Lett.*, vol. 81, pp. 429–432, 1998.
[139] S. Li, J. Chou, J. Wei, M. Sun, A. Hu, and A. Gali, "Oxygenated (113) diamond surface for nitrogen-vacancy quantum sensors with preferential alignment and long coherence time from first principles," *Carbon N. Y.*, vol. 145, pp. 273–280, 2019.
[140] Z. Sun *et al.*, "Boron-terminated diamond (100) surfaces with promising structural and electronic properties," *Phys. Chem. Chem. Phys.*, vol. 22, pp. 8060–8066, 2020, doi: 10.1039/d0cp00121j.
[141] E. A. Ekimov *et al.*, "Superconductivity in diamond," *Nature*, vol. 428, no. April, pp. 542–545, 2004.
[142] J. Hafner and G. Kresse, "Dimer reconstruction and electronic surface states on clean and hydrogenated diamond (100)surfaces," *Phys. Rev. B*, vol. 53, pp. 7334–7351, 1996.
[143] G. Kern and J. Hafner, "Ab initio calculations of the atomic and electronic structure of clean and hydrogenated diamond (110) surfaces," *Phys. Rev. B*, vol. 56, pp. 4203–4210, 1997.
[144] G. Kern, J. Hafner, J. Furthmuller, and G. Kresse, "(2 X 1) re cons truction and hydroge n-induce d de -re cons truction o f the diamond (100) and (111) s urface s," *Surf. Sci.*, vol. 352, pp. 745–749, 1996.
[145] Y. M. Wang *et al.*, "Recent studies on diamond surfaces," *Diam. Relat. Mater.*, vol. 9, no. 9, pp. 1582–1590, 2000, doi: 10.1016/S0925-9635(00)00292-2.
[146] J. McGhee and V. P. Georgiev, "Simulation Study of Surface Transfer Doping of Hydrogenated Diamond by MoO3 and V2O5 Metal Oxides," *micromechanics*, vol. 11, p. 433, 2020, doi: 10.3390/mi11040433.
[147] C. Verona, W. Ciccognani, S. Colangeli, E. Limiti, M. Marinelli, and G. Verona-Rinati, "Comparative investigation of surface transfer doping of hydrogen terminated diamond by high electron affinity insulators," *J. Appl. Phys.*, vol. 120, p. 025104, 2017, doi: 10.1063/1.4955469.
[148] C. Verona *et al.*, "Influence of surface crystal-orientation on transfer doping of V2O5/H-terminated diamond," *Appl. Phys. Lett.*, vol. 112, no. 18, p. 181602, 2018, doi: 10.1063/1.5027198.

[149] D. B. Buchholz *et al.*, “The Structure and Properties of Amorphous Indium Oxide,” *Chem. Mater.*, vol. 26, p. 5401, 2014.
[150] G. Gutierrez and B. Johansson, “Molecular dynamics study of structural properties of amorphous Al2O 3,” *Rhysical Rev. B*, vol. 65, p. 104202, 2002, doi: 10.1103/PhysRevB.65.104202.
[151] S. I. Allec, “Atomistic Modeling of Amorphous Materials,” University of California Riverside, 2020.
[152] E. A. Chagarov and A. C. Kummel, “Surface Science Molecular dynamics simulation comparison of atomic scale intermixing at the amorphous Al2O3/ semiconductor interface for a-Al 2O3/Ge, a-Al2O3/InGaAs, and a-Al2O3/InAlAs/InGaAs,” *Surf. Sci.*, vol. 603, pp. 3191–3200, 2009, doi: 10.1016/j.susc.2009.08.009.
[153] S. Plimpton, “Fast Parallel Algorithms for Short – Range Molecular Dynamics,” *J. Comput. Phys.*, vol. 117, pp. 1–19, 1995.
[154] F. G. Fumi and M. P. Tosi, “Ionic Sizes and Born Repulsive Parameters in the NaCl-type Alkali Halids-I,” *J. Phys. Chem. Solids*, vol. 25, pp. 31–43, 1964.
[155] F. G. Fumi and M. P. Tosi, “Ionic Sizes and Born Repulsive Parameters in the NaCl-type Alkali Halids-II,” *J. Phys. Chem. Solids*, vol. 25, pp. 45–52, 1964.
[156] B. Y. P. M. Morse, “DIATOMIC MOLECULES ACCORDING TO THE WAVE MECHANICS. II. VIBRATIONAL LEVELS,” *Phys. Rev.*, vol. 34, p. 57, 1929.
[157] S. L. Dudarev, G. A. Botton, S. Y. Savrasov, C. J. Humphreys, and A. P. Sutton, “Electron-energy-loss spectra and the structural stability of nickel oxide: An LSDA+U study,” *Phys. Rev. B*, vol. 57, pp. 1505–1509, 1998.
[158] R. Irani, S. M. Rozati, and S. Beke, “Structural and optical properties of nanostructural V2O5 thin films deposited by spray pyrolysis technique: Effect of the substrate temperature,” *Mater. Chem. Phys.*, vol. 139, pp. 489–493, 2013, doi: 10.1016/j.matchemphys.2013.01.046.
[159] J. Meyer, K. Zilberberg, T. Ried, and A. Kahn, “Electronic structure of Vanadium pentoxide : An efficient hole injector for organic electronic materials,” *J. Appl. Phys.*, vol. 110, p. 033710, 2011, doi: 10.1063/1.3611392.
[160] M. Ozboyaci, D. B. Kokh, S. Corni, and R. C. Wade, “Modeling and simulation of protein – surface interactions : achievements and challenges,” *Q. Rev. Biophys.*, vol. 49, pp. 1–45, 2016, doi: 10.1017/S0033583515000256.
[161] H. J. Berendsen, J. P. M. Postma, W. F. van Gunsteren, A. DiNola, and J. R. Haak, “Molecular dynamics with coupling to an external bath,” *J. Chem. Phys.*, vol. 81, p. 3684, 1984.
[162] F. A. Faber, A. S. Christensen, B. Huang, and O. A. Von Lilienfeld, “Alchemical and structural distribution based representation for universal quantum machine learning,” *J. Chem. Phys.*, vol. 148, p. 241717, 2018, doi: 10.1063/1.5020710.
[163] K. Ryczko, K. Mills, I. Luchak, C. Homenick, and I. Tamblyn, “Convolutional neural networks for atomistic systems,” *Comput. Mater. Sci.*, vol. 149, pp. 134–142, 2018.
[164] O. A. von Lilienfeld, K.-R. Müller, and A. Tkatchenko, “Exploring chemical compound space with quantum-based machine learning,” *Nat. Rev. Chem.*, vol. 4, pp. 347–358, 2020, doi: 10.1038/s41570-020-0189-9.
[165] H. E. Sauceda, S. Chmiela, I. Poltavsky, K. Müller, and A. Tkatchenko, “Molecular force fields with gradient- domain machine learning : Construction and application to dynamics of small molecules with coupled cluster forces Molecular force fields with gradient-domain machine learning : Construction and application to dynamics,” *J. Chem. Phys.*, vol. 150, p. 114102, 2019, doi: 10.1063/1.5078687.
[166] S. Chmiela, A. Tkatchenko, H. E. Sauceda, I. Poltavsky, K. T. Schütt, and K. Müller, “Machine learning of accurate energy-conserving molecular force fields,” *Sci. Adv.*, vol. 3, p. e1603015, 2017.
[167] L. Yang, P. Juhas, M. W. Terban, M. G. Tuckerd, and S. J. L. Billingea, “Structure-mining : screening structure models by automated fitting to the atomic pair distribution function over large numbers of models research papers,” *Acta Cryst.*, vol. A 76, pp. 395–409, 2020, doi: 10.1107/S2053273320002028.
[168] A. R. Oganova and C. W. Glass, “Crystal structure prediction using ab initio evolutionary

techniques: Principles and applications," *J. Chem. Phys.*, vol. 124, p. 244704, 2006, doi: 10.1063/1.2210932.
[169] S. Heiles and R. L. Johnston, "Global Optimization of Clusters Using Electronic Structure Methods," *Int. J. Quantum Chem.*, vol. 113, pp. 2091–2109, 2013, doi: 10.1002/qua.24462.
[170] D. Morgan, G. Ceder, and S. Curtarolo, "High-throughput and data mining with ab initio methods," *Meas. Sci. Technol.*, vol. 16, p. 296, 2004, doi: 10.1088/0957-0233/16/1/039.
[171] G. Taherzadeh, Y. Zhou, A. W. Liew, and Y. Yang, "Structural bioinformatics Structure-based prediction of protein – peptide binding regions using Random Forest," *Bioinformatics*, vol. 34, pp. 477–484, 2018, doi: 10.1093/bioinformatics/btx614.
[172] H. Shi, S. Liu, J. Chen, X. Li, Q. Ma, and B. Yu, "Predicting drug-target interactions using Lasso with random forest based on evolutionary information and chemical structure," *Genomics*, vol. 111, pp. 1839–1852, 2019.
[173] K. T. Schütt, P. Kindermans, H. E. Sauceda, S. Chmiela, A. Tkatchenko, and K.-R. Müller, "SchNet : A continuous-filter convolutional neural network for modeling quantum interactions," *arXiv Prepr. arXiv1706.08566*, 2017.
[174] K. T. Schutt, H. E. Sauceda, P. J. Kindermans, A. Tkatchenko, and K. R. Muller, "SchNet – A deep learning architecture for molecules and materials," *J. Chem. Phys.*, vol. 148, p. 241722, 2018, doi: 10.1063/1.5019779.
[175] Y. Huang, J. Kang, W. A. Goddard, and L. W. Wang, "Density functional theory based neural network force fields from energy decompositions," *Phys. Rev. B*, vol. 99, no. 6, pp. 1–11, 2019, doi: 10.1103/PhysRevB.99.064103.
[176] M. Todorović, M. U. Gutmann, J. Corander, and P. Rinke, "Bayesian inference of atomistic structure in functional materials," *npj Comput. Mater.*, vol. 5, no. 1, 2019, doi: 10.1038/s41524-019-0175-2.
[177] J. Vandermause *et al.*, "On-the- fl y active learning of interpretable Bayesian force fi elds for atomistic rare events," *npj Comput. Mater.*, vol. 6, pp. 1–11, 2020, doi: 10.1038/s41524-020-0283-z.
[178] S.J.D. Prince, *Computer Vision: Models Learning and Inference*. Cambridge university press, 2012.
[179] C. E. Rasmussen and C. K. I. Williams, *Gaussian Processes for Machine Learning*. MIT Press, 2006.
[180] D. Koller and N. Friedman, *Probabilistic Graphical Models: Principles and Techniques*. MIT Press, 2009.
[181] D. K. Duvenaud, "Automatic Model Construction with Gaussian Processes," 2014.
[182] M. G. Genton, "Classes of Kernels for Machine Learning : A Statistics Perspective," *J. Mach. Learn. Res.*, vol. 2, pp. 299–312, 2001.
[183] M. Abramowitz, I. A. Stegun, and D. Miller, *Handbook of mathematical functions with formulas, graphs and mathematical tables (National Bureau of Standards Applied Mathematics Series No. 55).* 1965.
[184] F. Pedregosa *et al.*, "Scikit-learn : Machine Learning in Python," vol. 12, pp. 2825–2830, 2011.
[185] M. U. Gutmann and J. Corander, "Bayesian Optimization for Likelihood-Free Inference of Simulator-Based Statistical Models," vol. 17, pp. 1–47, 2016.
[186] K. Nakata and A. Fujishima, "Journal of Photochemistry and Photobiology C : Photochemistry Reviews TiO 2 photocatalysis : Design and applications," *ournal Photochem. Photobiol. C Photochem. Rev.*, vol. 13, pp. 169–189, 2012, doi: 10.1016/j.jphotochemrev.2012.06.001.
[187] T. M. Breault and B. M. Bartlett, "Lowering the Band Gap of Anatase-Structured TiO 2 by Coalloying with Nb and N: Electronic Structure and Photocatalytic Degradation of Methylene Blue Dye," *J. Phys. Chem. C*, vol. 116, pp. 5986–5994, 2012.
[188] M. Zhou, J. Yu, B. Cheng, and H. Yu, "Preparation and photocatalytic activity of Fe-doped mesoporous titanium dioxide nanocrystalline photocatalysts," *Mater. Chem. Phys.*, vol. 93, pp. 159–163, 2005, doi: 10.1016/j.matchemphys.2005.03.007.
[189] T. Peng, D. Zhao, K. Dai, W. Shi, and K. Hirao, "Synthesis of Titanium Dioxide Nanoparticles with Mesoporous Anatase Wall and High Photocatalytic Activity," *J. Phys. Chem. B*, vol. 109, pp. 4947–4952, 2005.

[190] A. Zaleska, J. W. Sobczak, E. Grabowska, and J. Hupka, “Preparation and photocatalytic activity of boron-modified TiO2 under UV and visible light,” *Sci. Direct*, vol. 78, pp. 92–100, 2008, doi: 10.1016/j.apcatb.2007.09.005.
[191] M. Esmat *et al.*, “Nitrogen doping-mediated oxygen vacancies enhancing co-catalyst-free solar photocatalytic H2 production activity in anatase TiO2 nanosheet assembly,” *Appl. Catal. B.*, vol. 285, p. 119755, 2021.
[192] A. Testino *et al.*, “Optimizing the Photocatalytic Properties of Hydrothermal TiO 2 by the Control of Phase Composition and Particle Morphology . A Systematic Approach,” *J. Am. Chem. Soc.*, vol. 129, pp. 3564–3575, 2007.
[193] J. Yu, X. Zhao, and Q. Zhao, “Effect of surface structure on photocatalytic activity of TiO2 thin films prepared by sol-gel method,” *Thin Solid Films*, vol. 379, pp. 7–14, 2000.
[194] P. D. Cozzoli, A. Kornowski, and H. Weller, “Low-Temperature Synthesis of Soluble and Processable Organic-Capped Anatase TiO 2 Nanorods,” *J. Am. Chem. Soc.*, vol. 125, pp. 14539–14548, 2003.
[195] M. F. Aimi, M. P. Rao, N. C. Macdonald, A. S. Zuruzi, and D. P. Bothman, “High-aspect-ratio bulk micromachining of titanium,” *Nat. Mater.*, vol. 3, pp. 103–105, 2004, doi: 10.1038/nmat1058.
[196] E. R. Parker, B. J. Thibeault, M. F. Aimi, M. P. Rao, and N. C. Macdonald, “Inductively Coupled Plasma Etching of Bulk Titanium for MEMS Applications,” *J. Electrochem. Soc.*, vol. 152, pp. C675–C683, 2005, doi: 10.1149/1.2006647.
[197] B. W. K. Woo, S. C. Gott, R. A. Peck, D. Yan, M. W. Rommelfanger, and M. P. Rao, “Ultrahigh Resolution Titanium Deep Reactive Ion Etching,” *ACS Appl. Mater. Interfaces*, vol. 9, pp. 20161–20168, 2017, doi: 10.1021/acsami.6b16518.
[198] O. Khandan, D. Stark, A. Chang, and M. P. Rao, “Wafer-scale titanium anodic bonding for microfluidic applications,” *Sensors Actuators B*, vol. 205, pp. 244–248, 2014.
[199] P. S. Mirabedini, “LightCapture_Model.” https://github.com/pmirabedini/LightCapture_Model.
[200] A. Truszkowska, “MPI-style parallelized Shan and Chen LBM with multiscale modelling extension.” https://github.com/atruszkowska/LBM_MATLAB.
[201] A. Truszkowska, “Serial LBM implementation for small single phase scenarios.” https://github.com/LBMFluids.
[202] X. Shan and H. Chen, “Lattice Boltzmann model for simulating flows with multiple phases and components,” *Phys. Rev. E*, vol. 47, p. 1815, 1993.
[203] R. Benzia, S. Succib, and M. Vergassolac, “THE LATTICE BOLTZMANN EQUATION : THEORY AND APPLICATIONS,” *Phys. Rep.*, vol. 222, pp. 145–197, 1992.